UNIVERSITÁ DEGLI STUDI DI FIRENZE

SCUOLA DI INGEGNERIA

Dottorato di Ricerca in

Ingegneria Industriale

COORDINATORE: Prof. Maurizio De Lucia

CICLO XXXII

Design methods for

unmanned marine vehicles

Dottorando	**Tutor**
Dott. Ing. Alessia Meschini	Prof. Andrea Rindi

Coordinatore

Prof. Maurizio De Lucia

Anni 2016/2019

Abstract

Marine robotics is increasingly adopted in many fields of the underwater world, however, as of today, can still be considered a challenging task. In this framework, the research activity carried out during the PhD period concentrated on the study of hull ways of failure, with special focus given to cylindrical and dome shape, and on the development of an autonomous self-moving buoy for underwater target localization and communication. Starting from the current solutions identified within the state-of-the-art, the work was conducted heading to create a simplified calculation system for the design and sizing of submarine hull parts under pressure and, in particular, to codify a fast and light computational procedure to check the resistance of cylinders and domes. The investigated underwater vehicle, i.e. the here presented case study, named FeelHippo, was designed and assembled by the Department of Industrial Engineering of the University of Florence. Its main hull is composed of an extruded PolyMethyl Methacrylate cylinder and two thermoformed domes, which for the productive process have peculiar geometrical features. First, the theoretical critical buckling pressure of the cylinder was calculated using classical formulas; second, the critical buckling pressure was analytically derived and used to determine the optimized size in order to calculate the lowest thickness of the vehicle central cylinder to address the buckling effect. The available domes were experimentally tested until breakage, and then the dome design pressures were obtained, introducing additional correlations to consider the thickness variation and the flange constraints. The performance of the resulting method was evaluated by means of Finite Element Method simulations and tested during dedicated experimental validation campaigns; although it would be useful to extend the tests, the obtained results were satisfying, indicating that the derived solution may constitute a valid design tool for thermoformed flanged plastic domes, commonly adopted in the underwater field. As concerns instead the developed buoy, useful for the localization of underwater targets such as autonomous vehicles, it was designed by means of topology optimization techniques too, and then it has been mechanically tested and successfully employed during experimental tests at sea.

Summary

List of figures

List of tables

Acronyms

ABS	Acrylonitrile Butadiene Styrene
AM	Additive Manufacturing
ARCHEOSUb	Autonomous underwater Robotic and sensing systems for Cultural HEritage discovery cOnservation and in SitU valorization
ARROWS	ARchaeological RObot systems for the World's Seas
AUV	Autonomous Underwater Vehicle
BFS	Buckling Factor of Safety
CAD	Computer Aided Design
CPU	Central Processing Unit
CSSN	Centro di Supporto e Sperimentazione Navale
CURV	Cable-controlled Undersea Recovery Vehicle
DIEF	Department of Industrial Engineering of the University of Florence
DOF	Degree of Freedom
DS	Deformation Scale (percentage)
DVL	Doppler Velocity Log
ERL	European Robotics League
EUMR	EUMarineRobots
FEA	Finite Element Analysis
FEM	Finite Element Method
FLS	Forward Looking Sonar
FOG	Fiber Optic Gyroscope
GPS	Global Positioning System
IMU	Inertial Navigation System
LARS	Launch And Recovery System
LBL	Long BaseLine
LSM	Level Set Method
LIPO	Lithium Polymer
MARTA	MArine Robotic Tool for Archaeology
MDM Lab	Mechatronics and Dynamic Modelling Laboratory
MEMS	Micro Electro-Mechanical Systems
MPC	Multi Point Constraints
PDE	Partial Differential Equations

PMMA	PolyMethyl Methacrylate
PVC	PolyVinyl Chloride
ROS	Robot Operating System
ROV	Remotely Operated Vehicle
SAUC-E	Student Autonomous Underwater Vehicles Challenge - Europe
SIMP	Solid Isotropic Material with Penalization
SPC	Single Point Constraints
SPURV	Self-Propelled Underwater Research Vehicle
SSS	Side Scan Sonar
TDOA	Time Difference Of Arrival
THESAURUS	TecnicHe per l'Esplorazione Sottomarina Archeologica mediante l'Utilizzo di Robot aUtonomi in Sciami
TIG	Tungsten Inert Gas
TMS	Tether Management System
UCH	Underwater Cultural Heritage
UMS	Unmanned Maritime Systems
UniFI	University of Florence
USV	Unmanned Surface Vehicle
USB	Universal Serial Bus
USBL	Ultra-Short BaseLine
UUV	Unmanned Underwater Vehicle
ZENO	Zeno Environment Nautical Operator

Nomenclature

d	[mm]	External radius of the dome
f_y		Corrective factor for the theoretical yield pressure
h	[mm]	Height of the dome
k		Theoretical buckling pressure corrective factor dependent on the cylinder thickness
n		Number of circumferential waves lobes (integer that minimizes the expression)
t	[mm]	Wall thickness of the cylinder
t_H	[mm]	Minimum thickness of the dome
t_s	[mm]	Nominal thickness of the starting slab for dome geometry
AR		Aspect Ratio
E	[MPa]	Young's modulus
L	[mm]	Unsupported length of the cylinder between two reinforced rings
P	[MPa]	Theoretical critical buckling pressure for a non-hemispherical dome
P_c	[MPa]	Critical static compression pressure for a sphere
P_{crit}	[MPa]	Theoretical buckling pressure
P_{design}	[MPa]	Operative pressure at which the cylinder can dive safely
$P_{designDY}$	[MPa]	Operative pressure at which the dome can dive safely for yielding
$P_{designDB}$	[MPa]	Operative pressure at which the dome can dive safely for buckling
P_{exp}	[MPa]	Experimentally obtained buckling pressure at which the cylinder could start collapsing
P_H	[MPa]	Theoretical critical elastic buckling pressure of a hemispherical dome, considering t_H
P_y	[MPa]	Ideal yield pressure for hemispherical and homogeneous shells
P_{yc}	[MPa]	Theoretical corrected yield pressure for a hemispherical dome

PKD		Plastic Knock Down factor: ratio between the theoretical and experimental pressure
R	[mm]	Average radius
R_f	[mm]	External radius of the flange
SF	[mm]	Safety coefficient for the cylinder
SF_d		Safety coefficient for the dome
λ_c		Slenderness of the cylinder
λ_d		Slenderness of the dome
ν		Poisson's ratio
σ_y	[MPa]	Yield strength

Introduction

Nowadays, Unmanned Maritime Systems (UMS) are greatly used on the surface or underwater as they can partially or fully autonomously operate, avoiding direct unsafe human diving. The possibility of improving reliability and cooperation among vehicles is challenging and is the basis of this work. In the last decades, from the 50s, the marine engineering sector has substantially developed; just to give some examples of the many fields of application, the marine geoscience [1] and biology [2], the oceanography [3], the marine military defence [4], the underwater inspection [5], [6], for the Oil and Gas too [7], search and rescue at sea [8], [9], and the underwater archaeology [10] must be cited. Especially the last one allowed the birth and development of the underwater robotics research group in Florence within I have worked.

The investigation of the seabed and ocean floor, and everything that lies on it, is often demanding and hazardous too; this leads to the need of substituting or, at least, supporting the human activities with expendable vehicles. A first distinction among unmanned marine vehicles can be made based on their operative depth: the Unmanned Surface Vehicles (USVs) float on the surface; they consist of two main parts: the dead work, air side, which can communicate with control stations or satellites; the quick work, sea side, which can collect marine and acoustic data, depending on the payload, and fulfils the function of propulsion or mooring post. The Unmanned Underwater Vehicles (UUVs) can dive into the depth of the sea, and are usually classified according to their operational mode: a human control is required for the Remotely Operated Vehicles (ROVs) which are always wire-guided by a control station; on the other hand, the Autonomous Underwater Vehicles (AUVs), once deployed, are fully autonomous both in the motion and power supply.

Starting specifically from FeelHippo AUV, one of the AUVs already developed by the UniFI research group, the studies and activities performed by the candidate during the PhD period have been focused on the detection of a method to characterize its safety operative depth, especially studying the case of thermoformed flanged domes, and on the realization of a self-moving autonomous buoy for its underwater localization and for communication. This introductive chapter is organized as follows: Section I.1 presents the general framework in which this research activity took place; in Section I.2 some surface and underwater vehicles, which have been used as a comparison or starting point for this study, are collected; Section I.3 briefly illustrates the personal contribution of the research and summarizes the structure of the thesis.

I.1. Overall framework

The present research activity was conducted at the Mechatronics and Dynamic Modelling Laboratory (MDM Lab) of the Department of Industrial Engineering of the University of Florence (DIEF), operative in the field of underwater robotics since 2011. All the developed vehicles, although with different characteristics, are mainly born for archaeological applications; this does not mean that they cannot be used for different applications, by changing the payload.

The first project in which the MDM Lab has been involved was the Tuscan regional project "TecnicHe per l'Esplorazione Sottomarina Archeologica mediante l'Utilizzo di Robot aUtonomi in Sciami" (THESAURUS) [11], [12]. Among the project goals there was the development of technologies and methodologies for archaeological search with a swarm of AUVs performing cooperative autonomous surveys in exploration missions. One of the achievements was the development and realization of three Typhoon class AUVs [13], visible in Figure I.1, equipped with acoustical and optical payload, to detect and geolocalize potential object of interest lying on the seabed; the other obtained result was an underwater acoustic network both among the Typhoons and the potential fixed stations. These vehicles were a middle-size class AUVs and featured some innovations, which greatly contributed to reduce production and maintenance costs. The main features were [14]: an extended use of fiberglass, a cheap composite material with great corrosion resistance; a modular mechanical design including lots of standardized and interchangeable components; wide use of fast prototyping techniques, which made the vehicles easy customizable thanks to 3D printed accessories [15].

Figure I.1: Photo of Typhoon AUV.

During the evolution of the THESAURUS project, successfully concluded in 2013, the MDM Lab started coordinating the European FP7, call ENV-2012 challenge 6.2-6, project ARchaeological RObot systems for the World's Seas (ARROWS) [16]; this second project was committed to the development of advanced technologies for mapping, diagnosing and securing underwater coastal archaeological sites. It was focused on the possibility to adapt and develop low cost AUV technologies with the aim of reducing the costs of undersea archaeological operations [17]. Starting from the needs of underwater archaeologists involved in the project, some robotic tools capable of adapting in response to all phases of a typical archaeological campaign have been proposed. The result of the work carried on during the project by the MDM Lab was the modular small-size AUV MArine Robotic Tool for Archaeology (MARTA) [18], depicted in Figure I.2 just before an immersion. The most interesting features of

this vehicle were its modularity and ability to modify its overall structure, rearranging or substituting its parts; that allowed an easy adaptation to various operations. The hull of each module was made in Al Anticorodal type 6082 T6, a good trade-off among lightness and mechanical strength and the modules were connected together with suitable plastic wires to speed up and easy the assembling and disassembling phases.

Figure I.2: Picture of MARTA AUV.

Before the end of the project, since 2014 the University of Florence (UniFI) has joint the Interuniversity Centre of Integrated Systems for the Marine Environment (ISME) [19], a union of Italian research institutions involved in marine field. At the end of 2016, at the beginning of the PhD period, the MDM Lab together with the MDM Team S.r.l., an official spin-off company of the University of Florence, started working on the Autonomous underwater Robotic and sensing systems for Cultural HEritage discovery cOnservation and in SitU valorization (ARCHEOSUb) project [20]. The aim of the ARCHEOSUb project is to develop products and services to support the discovery of new Underwater Cultural Heritage (UCH) sites and the detection, conservation, protection and enhancement of new and existing ones, following the footsteps of previously concluded projects. Among the various technological results, there is the development of a compact, high performance AUV, able to support archaeologists during all the phases of a typical campaign.

Exploiting the acquired knowledge on the marine robots, the UniFI has actively participated in the design and development of the new low-cost AUV to assist in the investigation and monitoring of archaeological interest. The vehicle is named Zeno, which stands for Zeno Environment Nautical Operator, (Figure I.3), and it is configurable and customizable with different sensors and payloads. It can be easily deployed from a pier or a small boat and it is transportable by two people; its weight in air, thinking to the complete configuration, is about 45 kg. The vehicle is small and compact; the external dimensions are about 1 m long, 800 mm wide and 500 mm high and the chosen aspect is a packed "U.F.O. shape" [21] [22]. One of the innovation integrated into the Zeno AUV design is the battery module, quickly replaceable thanks to a lever system and watertight connections.
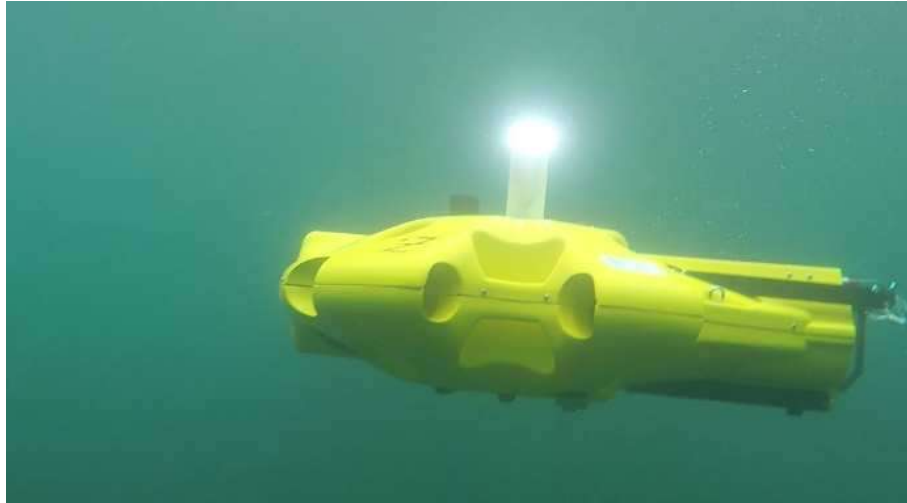
Figure I.3: Image of Zeno AUV.

FeelHippo AUV is the last vehicle it will be briefly described here: unlike the others vehicle developed by the research group, it is not a result of a founded project but it has been designed to be a development platform to test new payloads and new control algorithms for both MDM Lab researchers and students. Proof of this, throughout the years, FeelHippo took part in several monitoring tasks (in Figure I.4 the vehicle is depicted in Volcano Island during some experimental tests scheduled for EUMarineRobots (EUMR) [23]) and international student and non-student robotics competitions.
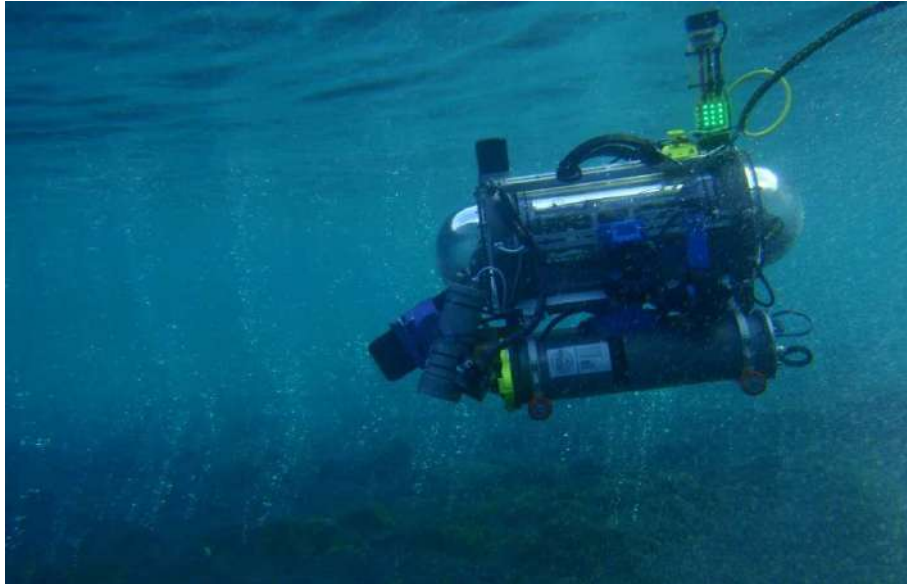
Figure I.4: FeelHippo AUV.

These events, besides being a precious and rare opportunity to test AUVs outside of research projects, promote the sharing of knowledge and the creativity of the participants, which usually have to face changing and challenging scenarios requiring the development of alternative solutions while dealing with strict time and resources [24]. Since 2012 a team from UniFI has taken part in one of this competition, particularly with FeelHippo in 2013, 2016 and 2018 has participated in Student

4

Autonomous Underwater Vehicles Challenge - Europe (SAUC-E) [25], while in 2015 competed in euRathlon [26], [27], and, finally, it took part in European Robotics League (ERL) Emergency Robots competition [28] both in 2017 [29] and 2019. The SAUC-E competition consists in some underwater trials stimulating autonomy and innovative approaches; euRathlon [30] and ERL more raise the challenge, recreating the consequences of a catastrophe to evaluate how robots coming from all the domains (air, land, and sea) could perform in different tasks (both with single and multi-domain cooperative missions) without human intervention. In 2013 and 2016, the team from UniFI placed third in the SAUC-E competition, while in 2017 it placed second in the ERL Emergency Robots air-and-sea sub-challenge, and fourth in the grand challenge (all the three domains included). Both in 2018 [31] and 2019 FeelHippo was first ranked for the sea domain. A detailed description of the vehicle will be given in Chapter 2, as FeelHippo represents the main test case for this PhD thesis.

I.2. Unmanned Marine Vehicles

The design certainly is tailored on the application field and over the past few decades, many unmanned marine vehicles have been developed for the most varied scenarios, creating an extremely wide world, starting with military applications (Figure I.5).

Figure I.5: Unmanned Maritime Systems classifications. (Credit U.S. Defense Dept).

Nevertheless, for instance, the role of the vehicle within an archaeological campaign is not too much different from a mission against mines [32] concerning the phases of search and inspection: in the first one, acoustic payloads, such as Side Scan Sonar (SSS) and Forward Looking Sonar (FLS), can be employed for quickly and ample surveying, to identify and mapping interesting places and targets, technically called "candidate points" [18]. In the second one the vehicle, once the point of interest is reached, acquires acoustic and optical pictures, e.g. for a 3D reconstruction, and usually navigating close to the target. In this phase, the hovering capability to acquire data from multiple directions is very important [33]. There are numerous companies

commercializing autonomous vehicles, while scientists [34] and researchers [35], [36] develop their own prototypes or employ commercial products. The UUVs are vehicles able to operate underwater without a human occupant and, as anticipated, two main classes are identifiable, more in detail: ROVs, on one side, which are directed by human operators by means of a control station, usually located on a support ship; the connection to the ship is an umbilical cable, which ensures the communication and, if needed, the power supply. On the other side, AUVs are completely autonomous, except for the deployment and recovery; they do not require any type of connection cable and operator to carry out their tasks. An AUV can perform a mission on long distance, with the only limit of power consumption. The use of UUVs entail the need of a proper localization system [37]. Radio waves, exploited by the Global Positioning System (GPS), are rapidly absorbed by water, therefore the need to rely on different acoustic tools for the positioning. The most common acoustic positioning systems are two [38]: the first one is the Long BaseLine (LBL), which guarantees an excellent accuracy, but needs various stations anchored to the seabed [39], and thus it is usually an expensive and time-consuming solution; the second one, cheaper and more flexible is the Ultra Short BaseLine (USBL). This can be equipped, for instance, on a USV; these unmanned vehicles can be used for multiple purposes and their use is growing, thanks above all to cost-effectiveness compared to a corresponding support vessel for experimental campaigns. To conclude, for a complete monitoring of a specific area of interest, the underwater vehicles (both ROVs and AUVs) have to be complemented by samples above the water [40] (e.g. buoy). Here below some ROVs, AUVs and USVs will be presented; for all of them the common thread is the evidence that the marine robotics can facilitate work from the sea surface to the seabed.

I.2.1. Remotely Operated Vehicles

The main applications in which a ROV is involved are underwater inspection and manipulation. Starting from the origins, the first ROV was born for archaeological research, and was named POODLE (Figure I.6).
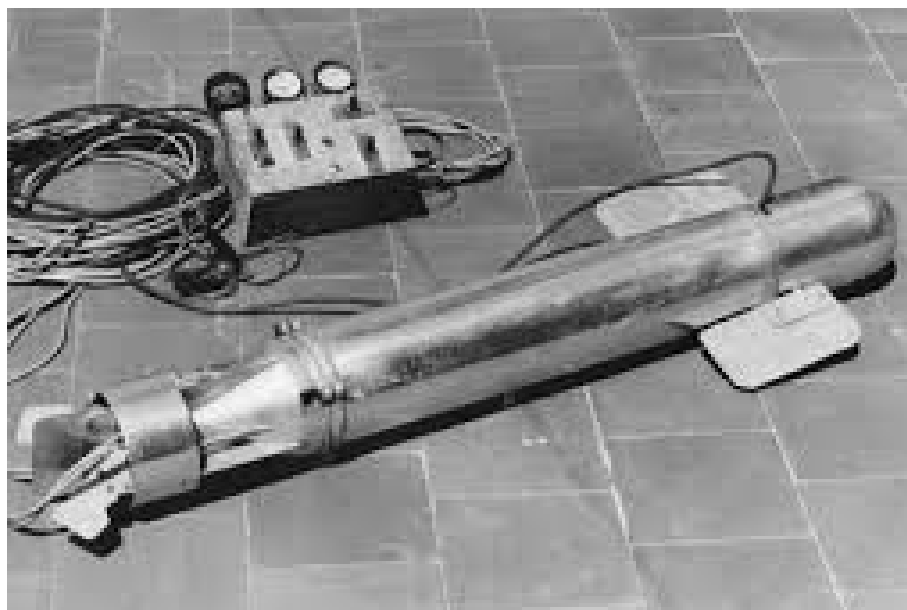
Figure I.6: Stock photo of POODLE ROV.

This simple vehicle was built by Dimitri Rebikoff, a French engineer with the desire to take a look at some Mediterranean wrecks, which were too deep for the divers. A camera was installed in a pressure-resistant housing, together with a water-corrected lens, and mounted on a tether-controlled vehicle, equipped with a stern thruster and two bow rudders. Despite its impact on the history of ROV was minimal, it was the start [41].

In the early of the 60s, the U.S. Navy presented to the world the first "modern" ROV named CURV (Cable-controlled Undersea Recovery Vehicle), of which different versions have followed one another, visible in Figure I.7. This UUV had simply defined the concept of ROV so much that from most it is considered the first one (from this, the typical ROV aspect is a cubic shape): a metal frame or a truss that supports and holds all the watertight housings and motors. Its field of application was the military one, actually it was the first armed ROV in the history. Indeed, this vehicle was thought to bring back torpedoes that failed to rise to the surface after test shots up to 3000 m [42].

Figure I.7: Stock photo of CURV-II.

Later this type of technology was used in the oil companies' field, and a specific class of ROVs able to operate on offshore oil field was born (starting from the RCV-225 and the RCV-150, of HydroProducts, Figure I.8). They are connected to the control vessel by an umbilical cable and, when working in difficult conditions or in deeper waters, a steel cable combined with a Tether Management System (TMS) is also used. The TMS is a device similar to a small garage that contains the ROV during lowering through the area of contact with the water surface or, on larger operational class ROVs, a separate assembly located above the ROV. The purpose of the TMS is to lengthen and shorten the cable so that the effect of the cable resistance in the presence of underwater currents is minimized. The umbilical cable is an armoured cable that contains a group of electrical conductors and optical fibres that carry electrical power, video and data signals between the operator and the TMS. The TMS then transmits the signals and power to the ROV along the cable.
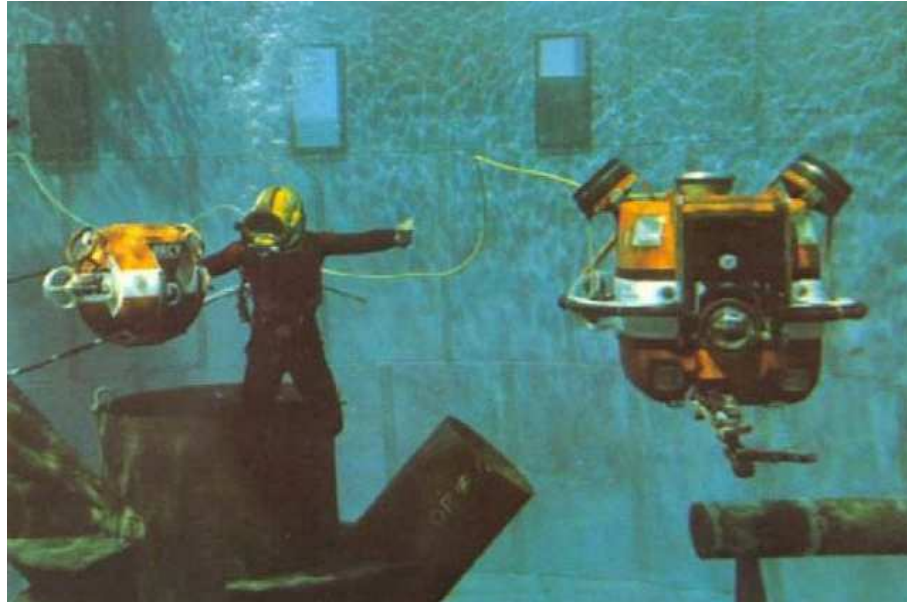
Figure I.8: Hydro Product RCV 225 and RCV 150.

Most ROVs are equipped with at least one camera and with illuminators. Equipment is commonly added to expand the capabilities of the vehicle. This can include sonar, magnetometers, camera, a manipulator or cutting arm, water samplers and instruments that measure the physical characteristics of water such as temperature, density, speed of sound and opacity, i.e. the presence of solid suspensions. To classify their function, the ROVs can be divided into Observation class, Working class and special use.

The Observation-class ROVs are normally a "flying eye" designed specifically for lighter use to place a camera and sensors where they can provide a meaningful image, or collect data. Furthermore with its tool package and many accessories, the observation class ROV is able to deliver payload packages of instrumentation, intervention and underwater navigation aids. One example of this type of vehicle is the Blue Robotics BlueROV2, (Figure I.9), a vectored six thruster ROV, heavy about 10 kg, big approximately 460x340x250 mm, capable to reach depths of 100 m [43].

Figure I.9: BlueROV2 by Blue Robotics.

The Working-class ROV systems generally have large chassis, with multifunction manipulators, hydraulic propulsion and actuation, and heavy tools for larger underwater construction projects, where heavy equipment needs to be moved.

Figure I.10: Photo of Tomahawk.

An example of Light Work-Class ROV is the Tomahawk by Sub-Atlantic, (operating depth 3000 m, general dimensions without LARS (Launch And Recovery System) (visible in Figure I.10) about 2x1x1m. In special-use ROV systems there are tethered underwater vehicles, designed for specific purposes. An example of a special use vehicle can be a cable burying ROV system designed to till the seabed to bury telecommunications cables.

I.2.2. Autonomous Underwater Vehicles

Historically, the research about AUV started only a few years after the first ROV. One of the first AUV built was the Self-Propelled Underwater Research Vehicle (SPURV), visible in Figure I.11, in 1957 by the University of Washington's Applied Physics Laboratory.

Figure I.11: Picture of SPURV AUV during a deployment.

The Office of Naval Research funded this vehicle for the U.S. Navy, it could dive up to 3000 m and operate for four hours. Sensors capable of temperature and conductivity measurements were used to support oceanographic research including diffusion studies, acoustic transmission and submarine wakes [44].

Nowadays, such vehicles can be considered a cost-affordable solution for many applications in the most diverse sectors [45]. An example of versatility, for instance, is given by the REMUS AUV [46]: it was originally developed for scientific sampling applications in water up to 100 m depth [47]. After the first vehicles were built and demonstrated for civilian applications, the U.S. Navy expressed interest in equipping them with SSS and using them to map the bottom and find mines in coastal environments [32]. Once more, another improved version of the same family vehicle, the REMUS-100 AUV (visible in Figure I.12), is used to obtain hydrographic observations under coastal sea ice [48].

Another field of interest is the deep water archaeology, in which both the survey and inspection are fundamental, together with the possibility of high-resolution characterization and data collection; two underwater archaeological campaigns are described in [49], [50].

Figure I.12: Photo of REMUS-100 AUV before a deployment.

A relevant sector of AUV employment to carry out high-depth tasks in environments which are unsuitable for divers is the Oil and Gas field; the Gavia [51] by Teledyne Marine is a family of AUVs (in Figure I.13, three models of GAVIA, from the background the GAVIA Offshore, the GAVIA Scientific and the GAVIA Defence,

Figure I.13: Family of GAVIA AUV.

together with an additional battery module and control notebook), specially designed to perform underwater measurements, research and monitoring of the seabed. The Gavia was the first product to offer a service for the Oil and Gas market, and this has made Teledyne one of the leading companies in this field.

Most of the AUVs, as the ones presented so far, have a torpedo shape to better navigate for long distance along the longitudinal direction, and cover for instance the search phase. Only in the last few years, thanks to the improving of control algorithms, which allow to improve their manoeuvrability, some AUVs have become more similar to standard ROVs for their shape and thrusters layouts. To conclude here is mentioned Sentry [52], visible in Figure I.14. This vehicle has been designed and built in 2010 by Woods Hole Oceanographic Institution (WHOI), USA, with the aim of providing hovering abilities and depth control independently of vehicle speed, and having a large distance between the centre of buoyancy and the centre of mass to minimize vehicle pitch and roll. The adopted solution is an elongated body along the vertical direction with two unique design features (its thruster configuration, the large separation between the centre of buoyancy and mass) that suited it to mapping rugged sub-sea environments, for instance oil spill assessment.

Figure I.14: Photo of Sentry AUV.

I.2.3 Unmanned Surface Vehicles

In recent years, the use of USV and/or buoys has become increasingly frequent as a replacement, for some activities, for boats or vehicles, the use of which is very expensive. The buoys are divided between those static, i.e. without a propulsion system, and those motorized, where the propulsion system allows the buoy to independently move in the desired position or to maintain a certain position [53]. In this paragraph some commercial buoys will be described together with a mechanical data table, available from the datasheet of the manufacturer's sites.

In the state-of-the-art literature, there are different applications where this type of vehicles is widely used, in addition to the military purposes already mentioned: first,

the optical visual survey is a technique that provides images or videos of the underwater environment through the use of the USV, to detect the seabed, a marine structure such as a pier or the hull of a ship or for a general underwater visual inspection. The results could be raw georeferenced or post-processed images or videos, such as photo-mosaic or 3D reconstruction of underwater objects. Second, acoustic investigations which serve for instance subsea positioning, oceanic meteorology data collection, surveillance and passive acoustic monitoring [54], [55]. Third, the bathymetry, which is the study of the underwater depths of lakes and ocean floors, the underwater equivalent of topography. The bathymetric maps show reliefs of the seabed such as depth contour lines (isobaths). Bathymetric mapping is carried out on industrial and tourist ports, on navigation channels before and after dredging, for submarine installation of cables and pipelines, on submerged coastal archaeological sites or for mapping marine habitats [56]. Fourth, for meteorology, buoys measure parameters such as air temperature above the surface, wind speed and direction, barometric pressure, water temperature, period and height of the dominant waves. The data are usually collected and processed on the buoy for transmission via radio or satellite to the meteorological communication centres. The buoys for meteorological analysis are divided into two categories: those moored, anchored to the seabed detect the physical-chemical parameters at a given point at specific times, while those drifting allow spread and continuous maps, for a more complete study of marine parameters [57]. Noteworthy, the multidisciplinary of the fields of application, e.g. to enhance the accuracy of oil drifting simulations, one needs to obtain the meteorological and oceanographic data around the oil slick [58]. Last but not least the water monitoring, through which the chemical, physical and biological characteristics of water are measured to monitor its state of health. Autonomous in-situ measurements over large areas significantly reduce the time and effort required for this task. In addition, in the event of water pollution generated, for example, by the accidental spillage of hazardous materials, the environmental investigation carried out by the USV-based system is of great help in providing a rapid understanding of the location and extent of the spillage, in order to quickly and effectively establish an appropriate response [59].

An example of oceanographic experiments with the use of, among various, moored instruments is well argued in [60]; the collectable dataset is, for instance, water masses and circulation, through current meter and operational forecasting thanks to meteorological buoy, together with lots of other sensors. One of the used buoy is the Waverider buoy, developed by Datawell, a private company, in a sensor-based (Figure I.15, Table I.1) version. Apart from wave height, wave direction and sea surface temperature, this buoy can also measure air temperature, surface current speed and direction. Obviously its correct functioning is closely linked to its correct mooring, deeply described in [61].

Table I.1: Waverider SG9 mechanical features [62].

Dimensions	Φ 900 mm
Weight	150 kg
Autonomy	33 months of operational life
Mooring post	Approx. 500 kg
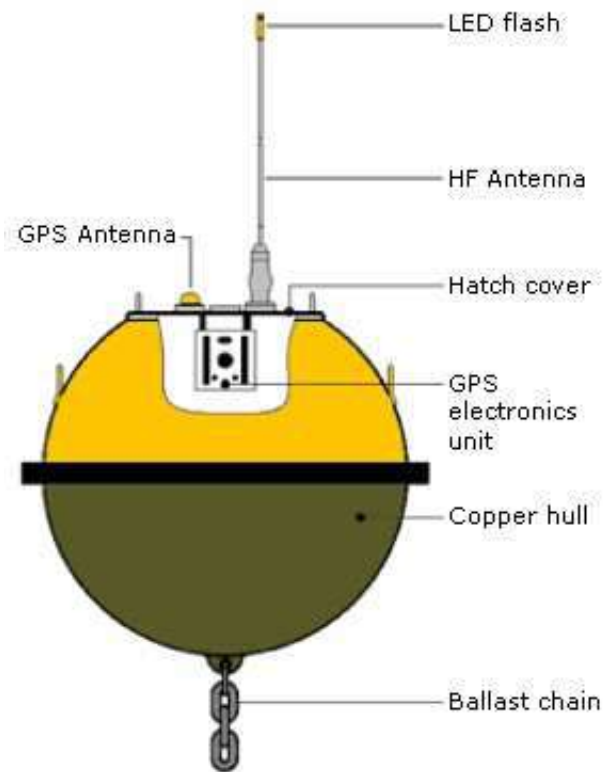
Figure I.15: Scheme of a Waverider SG Buoy.

Another example of a static buoy is the Gateway Buoy, (Figure I.16, Table I.2), produced by the Kongsberg Maritime company. This is used in combination with the REMUS AUV system to provide the operator with the ability to remotely track, monitor, command and interact with the vehicle while it is at sea. This allows operators to maintain communication with the vehicle and share information with all the interested parties, regardless of their location. Low-power Gateway buoys include an onboard power management system that automatically puts the buoy in an idle state during periods of inactivity. The buoy is very compact and can be deployed or hauled from a small boat without the need for any special handling equipment. The functions included are the monitoring and navigation functions of the AUV vehicle. The buoy can be anchored and act as a REMUS digital multi-channel transceiver within the detection area. When multiple buoys are deployed in known positions, triangulation techniques can be used to provide accurate information about the vehicle position during the mission. The information can then be transmitted via a radio modem installed on a ship or ground control station up to 5 miles away.

Table I.2: Gateway Buoy mechanical features [63].

Dimensions	Φ 381 mm, Emerged height 1220 mm
Weight	17.2 kg
Autonomy	200 hours "awake" time, or 60 days asleep time
Mooring post	48.6 kg

Figure I.16: Gateway Buoy [55].

To conclude two examples of dynamic buoys are mentioned. The Mooring-Free Buoy (Figure I.17, Table I.3) is a dynamic, moor-less buoy born from a collaboration between ASV Ltd and OSIL (Ocean Scientific International Ltd), as a low-cost alternative to moored buoy systems for a wide range of applications including oil and gas projects, dredger monitoring, environmental monitoring, current profiling, surface-to-submarine communication, port and ship safety, oceanographic data collection and positioning of submarine activities.

Table I.3: Moring Free Buoy mechanical features [64].

Dimensions	Length 2.4 m, Beam 1.2 m
Weight	450 kg
Autonomy	4 days
Payload weight	20 kg

Figure I.17 Mooring-Free Buoy.

The surface vehicle incorporates a wide variety of instruments including a turbidity sensor, an Acoustic Doppler Current Profiler or a multi-parameter probe. The mobile buoy can be programmed to maintain position, patrol a specific area or follow a ship (e.g. a dredger) using GPS technology. The data collected by the buoy can be forwarded to a ground base station or to a vessel via radio or satellite. Position maintenance algorithms allow the operator to set the allowable drift radius from the desired coordinate or to specify a route or route to follow. The benefits offered by this vehicle are the ease of transport and placement/recovery, no mooring authorizations required, low maintenance and operating costs.

The C-STAT 2 buoy (Figure I.18, Table I.4) is a vehicle produced by L3 HARRIS ASV, a world leader in the production of autonomous surface vehicles. The model offers the possibility of remaining in position for extended periods without the need for a ship in position or anchoring on the seabed.

Table I.4: C-STAT 2 Station Keeping Buoy mechanical features [65].

Dimensions	Length 2.7 m, Beam 1.44 m, Height 3.5 m
Weight	860 kg
Autonomy	10 days
Payload weight	30 kg

Figure I.18: C-STAT 2 Station Keeping Buoy.

The vehicle can be used as an aid in the submarine positioning of pipelines or similar, to allow communication between offshore and submerged systems, for the collection of oceanographic data, to monitor oil spills and for the safety of ports and ships. The system can be integrated with standard payloads or alternatively with one requested by users. The hull is optimized for oceanic performance and allows easy recovery and positioning at sea. The system is designed for position maintenance and self-adjustment.

I.3.   Contribution and thesis structure

Notwithstanding the significant and increasing engagement that has been developed towards the maritime engineering, in recent years, AUVs and autonomous underwater navigation can still be considered a challenging research field. The level of performance required is very high, and even more in case of multiple vehicles employed together; moreover, some severe limitations are imposed by the marine environmental conditions, for instance the GPS, widely used for the localization of land and air robots, cannot be exploited by AUVs since the radio waves are quickly absorbed by the water.

Starting from the aforementioned background, the research activities included and presented through this thesis coped with the hull design study, in particular dealt with types of collapse under uniform external pressure, and the realization of a hardware platform to guarantee communication and localization of underwater targets in general, the FeelHippo AUV from UniFI DIEF in particular.

The research activity carried out during the Ph.D. period focused on the study of a method to design specific underwater hull, focusing on cylindrical geometry and spherical domes. With the proposed approach, the methodologies reported in the literature were compared, and suitable modifications and improvements were investigated and implemented to extend the classical theories and data to this case study. The main hull of FeelHippo AUV is composed of an extruded PMMA (PolyMethyl MethAcrylate) cylinder and two thermoformed PMMA domes. One of the most important features of this material is its transparency which allows both the internal inspection of the vehicle and the positioning of optical devices [66], [67]. Starting from existing scientific literature, the collapse studies collected in the state-of-the-art literature were analysed, in order to identify their limitations which could provide a base for improvements or novel strategies. Some of the most relevant contributions used as a starting point are briefly commented below. For the first topic, for the cylindrical geometry collapse, two articles by Carl Ross are quoted: in [68] the study to generate design charts useful to predict the buckling collapse for near-perfect thick-walled is presented by theoretical and experimental points of view; in [69] the approach is also supported by a numerical study carried out through Finite Element Method (FEM). Both the articles, together with the other Ross's technical contributes, have been useful to get familiar with the problem, untimely collapse due to external pressure, and to offer the general guidelines of a new lean design procedures. In addition, the graphs were used as a comparison to check the test case. For the domes collapse, two other articles formed the first basis of the study: in [70] the scarcity of design rules in corresponding codes and recommendations of spherical shell has been highlighted, while additions are proposed that take into account relevant details such as boundary conditions, material properties and imperfections; following this approach, this research work focused on the boundary conditions, precisely the condition of constraint, and a theoretical integration has been proposed (in the case under study a tightening of the flange to 8 screws). The second main problem concerns the production process of thermoforming, closely related to the plastic material: in [71] a study on how the material flow properties affect the wall thickness has been presented; in fact, it is stressed that the thickness desired by the designer

must fall within tolerance limits, which can be respected thanks to additional techniques, but despite this, the thickness will never be uniform along the profile. For this reason a correlation has been searched and introduced to take into account the difference between nominal thickness at the base of the dome and minimum thickness at the top of the dome; moreover, as a precautionary measure, it was decided to introduce in the theoretical formulation the minimum value and not the average thickness.

The first geometry of interest is the cylinder (such as the central hull of FeelHippo AUV): the ideal main structure is usually a cylindrical shell crossed with equidistant rings and end caps. The analytical studies found in the literature have considered the behaviour of a cylindrical portion between two rings [69], and they have accounted for the simplification, uncertainties, and unmanageable details with appropriate safety coefficients. As a result of external pressure, a generic ductile resistant hull can be damaged in three ways: yielding, local or lobar instability, and general instability. When the external pressure generates compressive stresses that reach high levels, instability buckling phenomena predominate. For basic geometries, the linear buckling load can be determined by analytical and numerical studies. However, the linear buckling load is only an indication of the real buckling resistance of a shell; other important factors, such as geometric imperfections and the effects of the boundary conditions, must be considered [72] to obtain the actual buckling strength. For the cylindrical geometry, the theoretical formulations in the literature were used for verification. The widely applied cylindrical geometry was used to approach the problem of collapse and allowed the candidate to become familiar with the phenomenon; both a theoretical comparison and a simulated validation were performed.

The second studied geometric shape is the dome, which can collapse in different ways but presents a sudden loss of load capacity triggered by buckling. Studies on nonlinearity and marked imperfection sensitivity have been carried out since the study in [73]. Under a uniformly compressed state, both axisymmetric and asymmetrical behaviours can occur, as shown in [74]; in particular, the study focused on buckling and compression. These types of collapse are based on geometric and structural characteristics: for this reason, various breaking prediction theories have been studied to prevent these phenomena, as is the case in the present study. For this geometry, this study builds on the literature and represents a step forward in collapse prediction theories. Although the literature reports numerous complex theoretical treatments, during the PhD period a lack of implementation in real and diverse applications and few validations of the proposed theories have been highlighted [75]. The main difference is the material productive process, thermoforming, and the resultant geometry [71], [70]. The cases presented in the state-of-the-art literature do not fit the obtained results herein because of the non-negligible discrepancy in the constraints and the production process (e.g., [76], [77]). For the domes, the research focused both on buckling and compression phenomena and here there is a recap of the main followed steps: first, an experimental campaign was carried out. Then, the theories available in the literature were studied: because the correspondence with the proposed case was not satisfactory, some improvements and additions were applied. The obtained results with the new proposed approach are encouraging and

allow for the extension of the cases investigated in the literature. Furthermore, it is worth noting that the dome geometry is widely used in the field of submarine robotics.

To conclude the research activity, an autonomous self-moving buoy for the localization of underwater targets has been designed and developed, applying the theory for the cylinder collapse and exploiting optimization theories. The starting point were the following articles: in [78] some acoustic positioning systems are presented, together with their main advantages and disadvantages; looking at the USBL, the system used in UniFI Lab, the attention has focused on two features: the first is presented as an advantage over other systems and consists in having a system based on ship and not on fixed infrastructure, the second, already presented as a disadvantage, concerns the need to use additional sensors on the support boat in order not to affect the accuracy of the absolute position. In order to propose a solution to these two features, the idea of designing a sensorized support for the USBL, able to autonomously move and maintain the position, was born. A first version of the buoy was presented in [79], as a possible alternative to compensate for the lack of underwater GPS and to localize an underwater target; from the mechanical point of view some improvements are possible: it has only two thrusters, but above all it does not have a fixed connection between the USBL and the floating body and it is not very stable, transmitting further "disturbances" to the USBL. These three points have been implemented in the new buoy. One of the buoys that inspired the buoy configuration is the ASV presented in [80]: a positioning and communication movable station, useful for supporting diving operations, creating an underwater wireless network and supporting AUV operations by permitting a real-time remote access. To increase stability, it was decided to lower the centre of gravity by developing an elongated housing, able to accommodate bulky batteries, getting closer to the shape of the static buoys.

As acoustic waves are the only ones capable of propagating through water for long enough to be exploited for measuring the position of the vehicle, acoustic localization systems are widely used [37]. One of the most common acoustic positioning systems [81] is the relatively cheap and flexible USBL. Among the drawbacks of this solution, there is the dependence of the localization accuracy on the relative position between the target [82], e.g. an acoustic modem on the AUV, and the USBL device. In this work it has been decided to equip the autonomous self-moving buoy with an USBL, the here proposed buoy could follow the AUV during the mission, to maintain a certain distance thus optimize the AUV localization.

The thesis is organized as follows. Chapter 1 introduces the theoretical and mathematical background concerning the buckling design, the FEM and structural optimization; Chapter 2, starting from a brief description of FeelHippo AUV, collects the main cylinder state-of-the-art studies, with the obtained results. Chapter 3 describes the proposed theoretical improvements and the main obtained results, starting from the experimental results, elements of the dome theory and FEM achieved data. Chapter 4 focuses on the design of the self-moving buoy and its realization. The last chapter concludes the work.

Chapter 1

1. *Theoretical and mathematical background*

This chapter introduces the fundamental theoretical and mathematical concepts and computational tools used through the thesis. The first subject is the buckling design (Section 1.1); then the Finite Element Analyses (FEA) is mentioned (Section 1.2); lastly, the principles of structural optimization are reviewed with special focus on the topological optimization (Section 1.3).

1.1.Buckling design

High depths submarines used for carrying people, in general, consist of a hydrodynamic outer hull, and a structural inner hull to provide atmospheric pressure location for the passengers. The hull size is bound to the payload instruments to be on board, while the hull shape is constrained by the hydrodynamic features [83]. The structural hull can represent between a quarter and a half of the vehicle weight, but it is also the main watertight floating element. As during the dive, the internal pressure is generally immutable [84], the mechanical properties of the structural hull, (e.g. the yield strength, the behaviour to stability, the local crack resistance and the fatigue strength), directly influence the overall vehicle functioning. The design of the watertight hull involves the selection of the hull shape, the selection of materials and the evaluation of the stress distribution and buckling stability [85]. Some factors mainly influence the design, they are briefly listed: the flotation coefficient (the ratio between weight and volume), the necessary internal layout and shape, the production process (at the base of this work), the operative depth, the safety factor for different collapse modes and the hydrodynamic resistance. The objective of the usual design is to reduce weight by increasing internal usable volume, to better include more payload, and reducing hydrodynamic resistance, to navigate more with the same amount of stored energy.

The shape of the hull, a primary focus of the design, is most often cylindrical or spherical. The first one, usually is in the form of a ring-stiffed circular shape to better resist the external hydrostatic pressure effects and to have the largest volume available with the same diameter [86]. For instance some typical cylindrical hull solutions are depicted in Figure 1.1 [87]: the cylindrical shape of the hull is relatively easy to produce and the useful volume makes it easy to organize the layout of the onboard instrumentation. The smooth cylindrical shape (Figure 1.1A) generally guarantees excellent hydrodynamics, better internal arrangement of components and lower construction costs. The stability of the smooth cylindrical shape can be guaranteed by acting on the thickness when the diameter, length and external pressure have small values. The internal structure of a straight cylindrical shape, as already mentioned, is often divided by ring rib (Figure 1.1B) to increase its rigidity without compromising the flotation coefficient and the hydrodynamics. The corrugated cylindrical structure, shown in Figure 1.1CD, can be manufactured in the

form of segments, more or less tapered or hemispherical, maintaining low cost productivity.
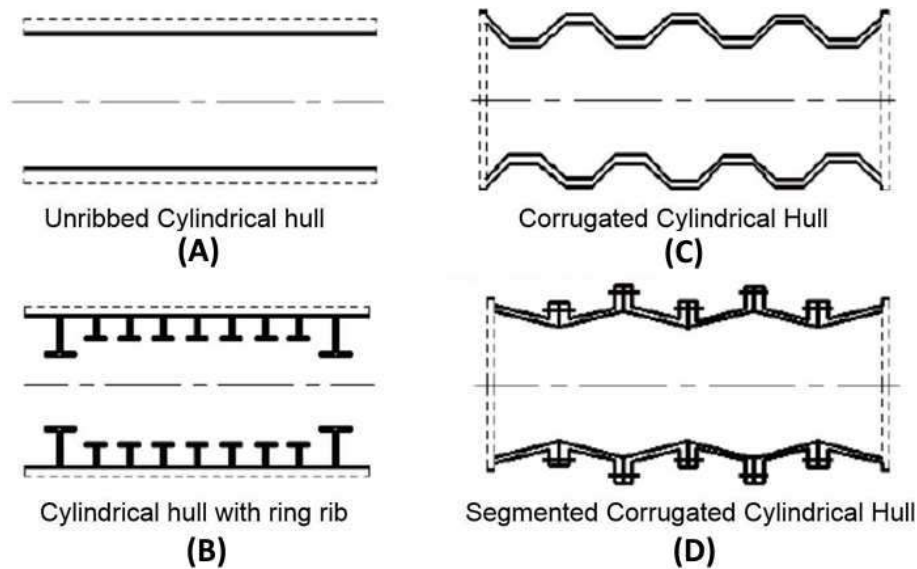
Figure 1.1: Typical cylindrical hulls [87].

In underwater robotics, the other more commonly used end geometry is spherical rather than a flat surface because the distribution of stress on the surface is homogeneous, and the hydrodynamic drag is reduced [88], moreover spherical geometries are ideal for responding to external pressure because if ratios between the thickness of the wall and the diameter are small, then they allow for an almost uniform distribution of stresses through the thickness [72]. However, its occupancy rate is lower than the cylindrical hull, because the shape does not favour the useful arrangement of the components. The spherical structure is not very easy to manufacture but can be made at a constant thickness without reinforcing ribs. A peculiar example is the structure made up of multi-spheres connected to each other, allowing to reduce the frontal area of the vehicle with the same useful volume. It is a way of approaching the cylindrical shape maintaining a structural resistance similar to the single sphere but obtaining a lower hydrodynamic resistance. [87]

The hull material is another fundamental aspect to consider since the production process can introduce non-negligible peculiarities [76], [89]. The most common materials for these types of mobile robots are metal alloys (high-strength steels, aluminium, or titanium) or composites (glass-fibre-reinforced plastic, carbon epoxy, or metal matrix composite) [86], [90].

Both yielding and buckling can result in failures; their causes, which include geometry and boundary conditions, are highlighted below. The analytical studies found in the literature have considered the behaviour of a cylindrical portion between two rings, and they have accounted for the simplification, uncertainties, and unmanageable details with appropriate safety coefficients. Because of many uncertainties and practical difficulties encounterable when dealing with the design of resistant hulls, so it is necessary to refer to models that can best represent reality. The calculation model, moreover, in consideration of the high design quotas, assumes that only a uniform external pressure acts on the resistant hull, neglecting the hydrostatic

gradient that is however recorded between the top and bottom of the boat. The stressing load on the resistant hull will therefore be that due to the pressure acting in the radial direction on the cylindrical mantle and in the axial direction due to the presence of the end bottoms [91]. As a result of an external pressure applied, a generic ductile resistant hull can be damaged in three ways, as better explained through Figure 1.2: cylindrical structure with non-deformed internal rings (on top), subjected to yielding (a), local instability (b), and general instability (c)
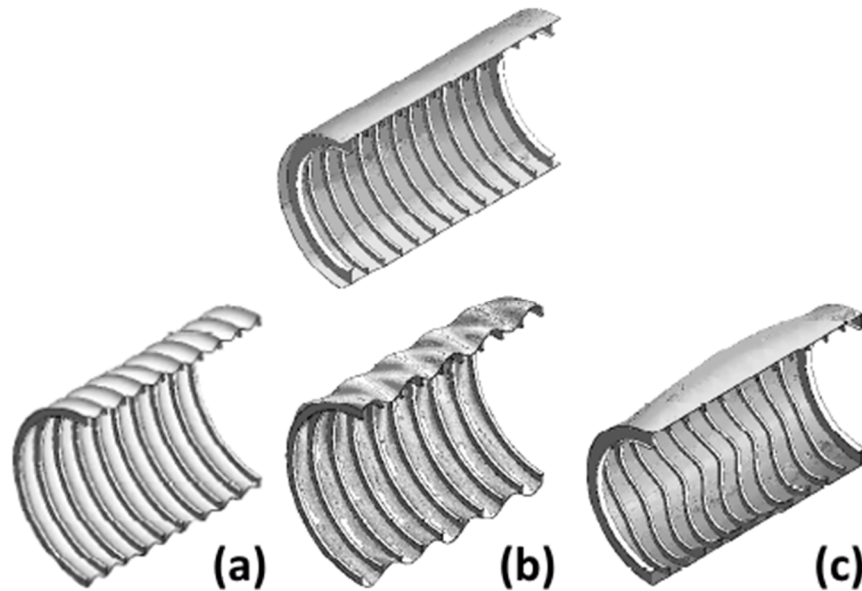
Figure 1.2: Ways of hull failure.

Yielding is axisymmetric inelastic collapse, which occurs at the plating, whose manifestation is an accordion fold between adjacent frames; local instability involves an asymmetrical inelastic collapse of the plating between adjacent frames and is characterized by a certain number of lobes, i.e. undulations that follow one another alternately in convex and concave form in both the circumferential and longitudinal directions. This phenomenon is influenced by numerous geometric parameters (cylinder diameter, plating thickness, distance between frames, geometric-inertial characteristics, mechanical properties of the material) and from the imperfections of circularity of the cylinder, (out of roundness), and straightness of the cylinder generators. It is noted that in the case of an infinitely long tube there is a simple instability due to ovalization (2 lobe mode), while as the decrease of the length of the cylindrical mantle the number of lobes increases rapidly. To visualize the first ways of instability of an annular beam, an example scheme is given in Figure 1.3.
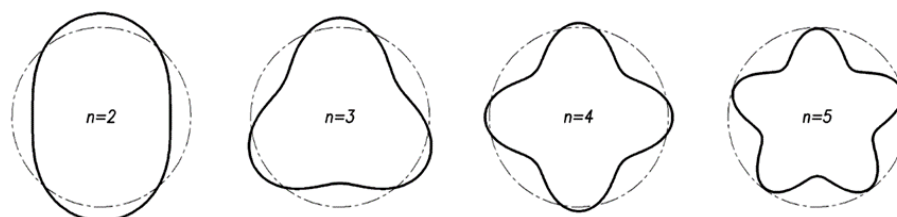
Figure 1.3: First ways of instability typically found in the annular beams [91].

General instability is an inelastic collapse involving both the planking and the ordinary frames between two reinforced transverse structures; this phenomenon is strongly influenced by the moment of inertia of the frames, by their imperfect circularity and the length/diameter ratio of the cylinder (the onset of this phenomenon is favoured on very slender hulls).

The current trend of designing hulls of underwater vehicles is to consider a specific sizing so that only yielding can occur at the design pressure. Because appropriate safety coefficients are used, the critical factors linked to both local and general instability should appear after the operating pressure exceeds the design pressure. In particular, the failure modes due to global instability are very sensitive to manufacturing imperfections [91]. When compressive stresses generated by the external pressure reach high levels, instability buckling phenomena become prevalent. For basic geometries, the linear buckling load can be determined by analytical and numerical studies, even if it is only an indication of the real buckling resistance of a shell; again, other important factors, such as geometric imperfections and the effects of the boundary conditions, must be considered [72]. For this reason, this research study focused on breakage due to the instability, first of cylinder then of dome.

Sizing is carried out to ensure that the structure will not be damaged, regardless of the phenomenon that occurs. With the application of a uniform pressure range, the collapse of a circular cylinder occurs with an external pressure that is a small fraction compared with the one to be internally applied. This mode of failure is known as shell instability or lobar buckling, and it causes a collapse around its circumference in the form of a number of circumferential waves or lobes [68]. General instability manifests as the physical collapse of the entire shell because of the low strength of the ring-stiffeners. Finally, axisymmetric deformation takes place if the circular cylinder implodes while maintaining its circular shape [68]. Resistance to external pressure is further diminished by initial out-of-circularity [69].

Regarding the spherical shape, both axisymmetric and asymmetrical behaviours can occur [74]. Studies on purely linear elastic buckling formulation has been started in 10s [92]. These types of collapse are strictly based on geometric characteristics: for this reason, various breaking prediction theories have been studied, starting from specific boundary conditions [93], but there is a lack of implementation in diverse applications; for instance the discrepancy in the constraints and the production process are non-negligible. A hemispherical shell is able to withstand higher internal pressure with respect to any other geometrical hull with the same wall thickness and radius. Thus, it is a major component of pressure vessel construction and has a smaller surface area per unit volume with respect to any other shape. For complicated structures, such as shells, the modern design technique tends to improve the model investigation since, in most cases, the true behaviour of the shell, with the load and the constraints, is not known or very difficult to know. The best approach is to make some assumptions and then verify them by using dedicated tests [94].

In this work, the study focused on domes, which greatly differ from the simple spherical geometry, if only for the presence of a connection flange. It is very important to study these elements, as usually, some forms of dome are included in pressure

vessel designs, e.g. as end caps to cylinders. The domes can be divided mainly into three groups, depending on the aspect ratio (AR): prolate (AR > 1.0, Figure 1.4A), hemi-spherical (AR = 1.0, Figure 1.4B) and oblate (AR < 1.0, Figure 1.4C). Experimental research has shown that, under uniform external water pressure, the hemi-ellipsoidal prolate domes and the hemi-spherical domes tend to collapse for lobar buckling, while the hemi-ellipsoidal oblate domes tend to collapse for asymmetric buckling [95].
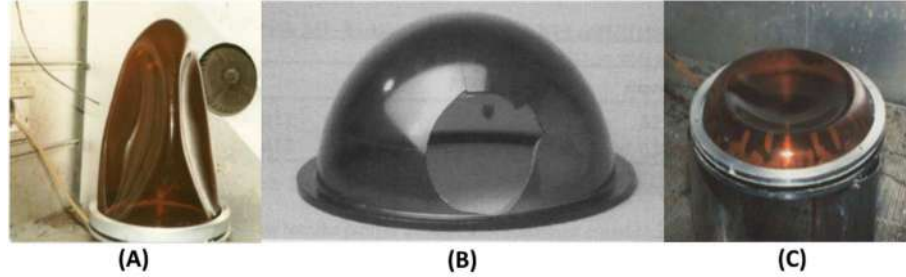
Figure 1.4: Buckling collapsed domes [95].

1.1.1. *Linear buckling analysis*

The purpose of numerical buckling analysis is to determine, as in the case of modal analysis, the system modes of vibrating; the first modes have a greater interest in triggering instability. Computational modelling, synonymous of numerical methods, is often used to predict the buckling stability behaviour of shell elements. The elastic buckling is a variant of the analysis at standard eigenvalues, it determines the system stability to verify the possibility of an unstable behaviour occurring beyond a certain critical load due to a small system disturbance.

The linear elastic instability problem is solved by applying a reference load L_{ref} to the structure and performing a static analysis to obtain the necessary stresses to generate the geometric stiffness matrix K_g [96] Eqn. (1.1). The loads at which buckling occurs are then calculated by solving a problem with the eigenvalues:

$$[K - \gamma K_g]x = 0$$

(1.1)

where K is the structure stiffness matrix and γ the multiplier for the reference load. The solution of the problem to eigenvalues generally provides n_{DOF} eigenvalues where n_{DOF} is the number of DOFs. Vector x is the eigenvector corresponding to its eigenvalue and the problem of eigenvalues, is solved using the Lanczos matrix method [97]. Not all eigenvalues are necessary for buckling analysis so normally only a small number are calculated, the lowest eigenvalue is associated with instability and the corresponding critical buckling load, $L_{cr,}$ Eqn. (1.2) is as follows:

$$L_{cr} = \gamma_{cr} L_{ref}$$

(1.2)

In buckling analysis, zero-dimensional elements are neglected because, even if present in the model, they do not contribute to the geometric stiffness matrix K_g, as

well as the contribution of rigid elements, which are mono-dimensional, is not included.

For an analysis of elastic deformation, the eigenvalue problem is defined with respect to the tangent stiffness matrix, [K_T], which is the same to the second derivative of the potential energy. The critical points are defined with eigenvalues equal to zero Eqn. (1.3):

$$[K_T]\{\Phi\} - \zeta\{\Phi\} = 0$$

(1.3)

The vector, $\{\Phi\}$, and the coefficient, ζ, are the eigenvector and the eigenvalue, and stand for buckling mode and buckling load factor. The next equation, Eqn. (1.4) shows that the tangent stiffness matrix is composed of the linear elastic stiffness matrix, [K_0], which is independent of load, initial displacements matrix [K_L] and initial stresses matrix, [K_σ], respectively, which are both related to the applied load [98]:

$$[K_T] = [K_0] + [K_L] + [K_\sigma]$$

(1.4)

A possible linearization of the eigenvalue problem involves assuming that the structure displacements in the preload phase are small, and therefore [K_L] can be neglected Eqn. (1.5). This leads to:

$$[K_T]\{\Phi\} + \zeta[K_T]\{\Phi\} = 0$$

(1.5)

For a single discrete eigenvalue problem, there are N eigenvalues, where N is the order of the linear stiffness matrix. The lowest of these eigenvalues are of primary interest, since this value represents the critical factor of elastic buckling for the structure. This value is approximately equivalent to the classical pressure elastic buckling solution.

1.2. Finite Element Method

FEM allows the modelling and the analytical resolution of problems that can be schematized with Partial Differential Equations (PDE): since the 1950s, this method has been widely developed and used leading to today applications in all research fields. The generic geometry constituting the object to be studied is divided into "elements": basic building blocks of FEA, parts that can be from one-dimensional to three-dimensional (lines (trusses or beams), areas (plates and membranes) or solids (bricks or tetrahedrons)) depending on the specific application, the object that is to be modelled and type of analysis that is going to be performed. An element is a mathematical relation that defines how the degrees of freedom (DOFs) of a node are related to the next. A "node" is a coordinate location in space where the DOFs (which are possible movement of the point due to the loading of the structure and/or which forces and moments are transferred from one element to the next) are defined. The information used in study is assigned to nodes.

The modelling of a physical system can be summarized as follows:

- division of the continuous physical domain into solution domains, i.e. in the finite elements, using lines or surfaces;
- assumption of the connection through a discrete number of nodes located at the extremities (in the case of more complex elements they can also inside be placed). Nodal displacements are the primary unknown quantities of the problem;
- each finite element displacements and its contours are uniquely defined by a set of functions in terms of nodal displacements;
- the functions that define the displacements allow the univocal calculation of the deformations in an element, in terms of nodal displacements. Using the initial stress values and material properties together with the deformations the stress states of the elements can be derived;
- calculation of the concentrated forces on each node that balance both the boundary conditions and the tensions present on the domain. [99]

To sum up, a discretization of the problem was carried out, obtaining a finite number of elements and nodes and therefore a finite number of unknowns (firstly nodal displacements); to know the quantities values in points between the nodes interpolating functions are used. Obviously, the numerous approximations are introduced with this method, both in the geometric and analytical field, but its ease of use has allowed its wide spread of uses. If a constraint affects one or more DOFs of a node it is Single Point Constrains (SPC). If, on the other hand, a constraint consists of a relationship between several DOFs different nodes it is a MPC (Multi Point Constraints).

1.2.1. *Buckling FEM model*

In general, the buckling behaviour of shell-type structures can be described by assuming the presence of small and moderate deformations, from moderate to large rotations, and large displacements; for thin shell elements, or elements with a small number of nodes, reduced integration patterns are required, in combination with a control method Figure 1.5.
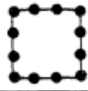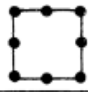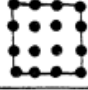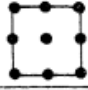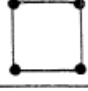
		fully integrated elements tendency to		reduced integration obligatory if
		shear locking	membr. locking when curved	
Serendipity	S12	large	low	thin
Serendipity	S8	large	large	curved thin
Lagrange	S16	low	low	not necessary
Lagrange	S9	low	large	curved
S/L	S4	extreme	extreme	always

Figure 1.5: Integration requirements for various shell elements [100]

25

Some higher-order elements, for example the Lagrange 16-node element, are not arranged to "locking" and therefore do not require reduced integration; however, such elements are computationally expensive and not considered practical for many applications. An alternative to using structural shell elements is the use of solid, or continuous, elements. The need to maintain reasonable aspect ratios of the elements, in combination with the thin shell geometry, results in a large number of elements for typical thin-walled structures. This is particularly pronounced if it is necessary to model multiple elements, for example, induced bending of a soft material. [100]

The structure of the finite element mesh (density and pattern) has a significant influence on the subsequent prediction of deformation or buckling collapse load and its mode. The mesh should be able to faithfully represent any geometrical imperfections and the shape. [101] Mesh convergence studies represent the discretization error in FEM by subsequently reducing the element size until the solution converges to a reasonable tolerance. The representation of the middle plane of the shell is the obvious choice for the cylindrical tubes, which make up most of the numerical buckling studies.

1.3. Structural optimization

Historically, the design is based on the experience and personal knowledge of the designer and the existing literature, but it takes a long process of "trial and error" until reaching a solution that meets all the requirements. This method is time consuming and expensive both for human and calculation resources used; it also does not provide information on the sensitivity of the solution to design parameters changes. A better approach to the design problem is achieved by creating an appropriate mathematical model through the definition of equations, objectives and constraints imposed on the structure; the solution can be considered the best as it achieves the objectives set while respecting the constraints imposed. The structural optimization problems are often addressed in many fields of engineering and different mathematical methods have been developed and exploited to solve this problem. In general, the mathematical formulation of optimization problems follows fixed steps:

- objective function definition;
- project variables choice;
- governing problem equations formulation;
- constraints and limitations definition.

The objective function, which will be maximized or minimized depending on the specific case, can cover any aspect such as cost (material, manufacturing or use), mechanical properties, etc. Actually, this concept does not only concern the structural field, but it affects a multitude of fields (fluid mechanics, electromagnetism, bioengineering, optics, economics, etc.). If several objectives, not in conflict with each other, are considered in the same problem, a multi-objective optimization problem is generated. The governing equations closely depend on the type of considered problem while the constraints limit the domain of acceptable solutions. It should be noted that constraints which are beyond outside the admissible domain zone are inactive. In Figure 1.6 a graphical representation of optimization search problems is given.
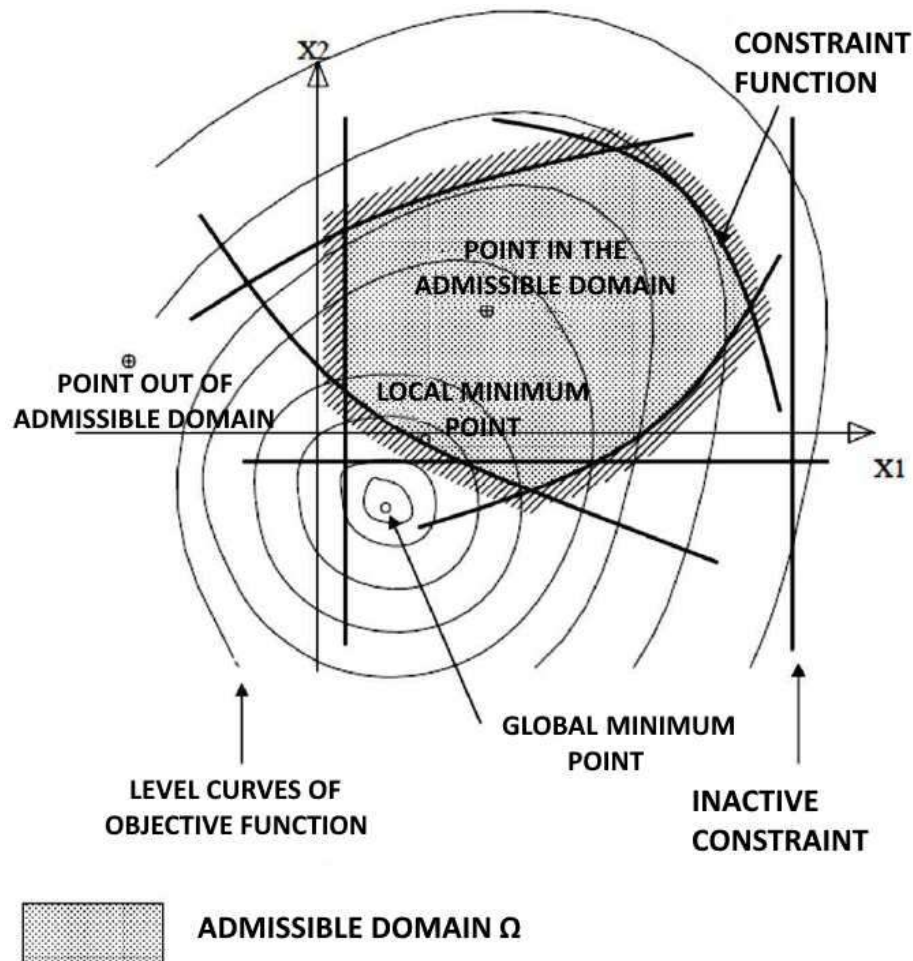
Figure 1.6: Objective function, constraints and admissible domain [102].

The main classification divides the optimization into three categories [103], shown schematically in Figure 1.7:

- sizing optimization [104]: the structural shape is known and the objective is the minimization of the structure by varying the components dimensions; the variables design are the structural elements dimensions, such as the diameter of a rod or the thickness of a beam, in this case the thickness of the cylinder;
- shape optimization [105]: the structure topology is known (e.g. the number of holes) and will not be changed; the design variable can be e.g. the distribution of thickness on the structural members, the diameter of the holes or the curvature radii. The other types of optimization can have more design variables applied to each element while in shape optimization each design variable can affect more elements;
- topology optimization [106]: this is the most general optimization whose purpose is to determine the optimal distribution of material and voids, respecting the constraints imposed and achieving the objective functions. Before optimization, neither the component geometry nor the topology (shape or number of holes) are known.

In all types of optimization, the component is divided into two areas: a design space and non-design space: the solver will act on design ones, changing the size and / or geometry, while the non-design will not undergo any alterations.
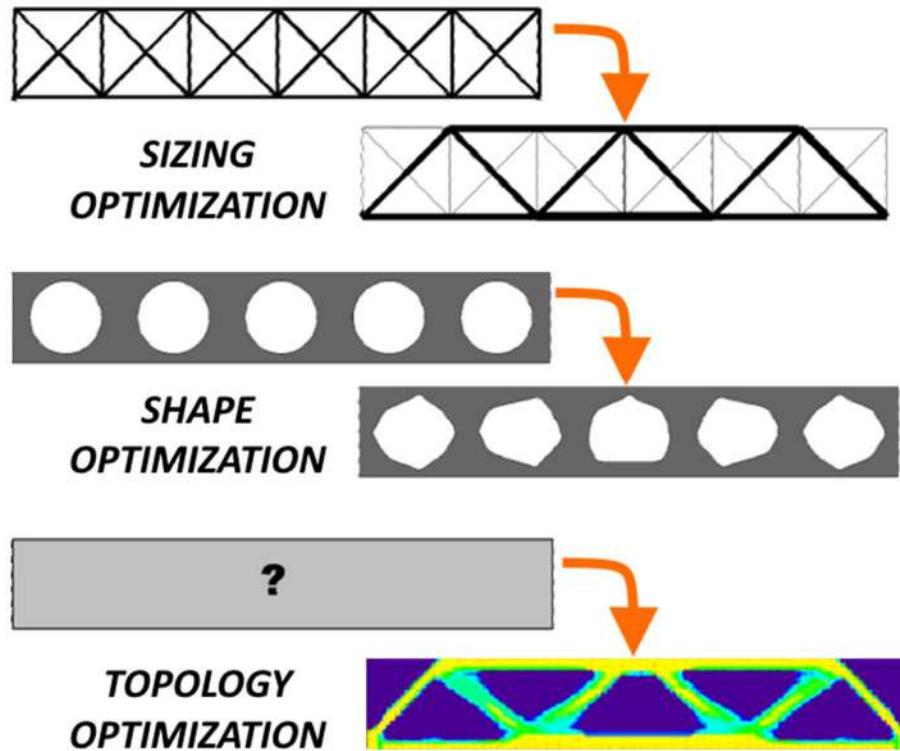
Figure 1.7: Optimization typology scheme.

1.3.1. *Topology optimization*

Topology optimization techniques have so far been dealt with in various engineering fields (especially in civil engineering [107], automotive [108]and lately also biomedical [109], [110]), but in the field of underwater [111] robotics is still not widespread [112]. They can therefore certainly be considered one of the most challenging and promising methods for structural optimization, especially in view of space and weight limits, in standard and new concept vehicles [113].

This process leads to determining the optimal distribution of a given amount of material, in the design domain, to achieve optimal connectivity; shape and number of holes are maximized or minimized while maintaining specific structural performance [114]. Topology optimization allows the modification of structures topology and has the ability to generate a large number of DOFs available for design variable settings, so that optimal design can be achieved without prior knowledge [115].

Topology optimization problems are solved using the density method, also known as the Solid Isotropic Material with Penalization (SIMP) method, where the design variable is a pseudo material density ρ_f [116]. The density of the material is defined within 0 and 1, where 0 stands for the empty state and 1 the solid one. Under topology optimization, the material density ρ_f of each element varies continuously between 0 and 1, defining the element as being respectively either void or solid. The stiffness of the material is assumed to be linearly dependent on the density. The SIMP method applies a power-law penalty Eqn. (1.6) for the ratio of stiffness to density, to set the density of the elements and can be expressed as follows [117]:

$$K_p(\rho_f) = \rho_f^p K$$

<div align="right">(1.6)</div>

where

K_p is the penalized stiffness matrix (referring to a generic FEM discretized element);

K is the real stiffness matrix;

P is the penalization factor (greater than unit);

ρ_f if the fictitious density.

The Level Set Method (LSM) is therefore used to solve the problem resulting from the introduction of the pseudo material density, as it is an excellent tool for modelling time-varying objects and following shapes that modify the topology. The use of Level Set techniques for the topology design has been recently proposed too. This method is a conceptual framework for using layer sets as a tool for numerical analysis of shapes and surfaces. The contours of a parameterized family of Level Set functions are used to generate the boundaries of a structure, and the topology can change with modifications in the Level Set function. The boundary of the design is represented as the isosurface (the zero level set) of a function defined on the finite element mesh. This function takes different values according to the different area (material region, boundary or region without material). Through the use of LSM, numerical calculations involving curves and surfaces can be performed on a fixed Cartesian grid without necessity of these objects parameterization [118].

Topology optimization, is definitely flexible and customizable, indeed it allows to take into consideration: several types of external loads, several boundary conditions and imposed mechanical constraints, several optimization objectives (e.g. volume or compliance, which is the structure deformation energy and it can be considered as the reciprocal measure for the stiffness of the structure) and several optimization constraints (e.g. natural frequencies, stress, volume fractions).

To sum up, the optimization process follows these steps:

- definition of test case, its physical and geometric features together with boundary conditions and external loads applied.
- static analysis on the standard original model as benchmark tests.
- definition of design space, which can change during the topology optimization too.
- definition of objective function and optimization constraints for the static characteristics.
- topology optimization that differs from the other structural optimization techniques, because it allows to change the topology of structures layout.

At the end it is possible to generate a surface rendering, to smooth surfaces derived and to compare the obtained weight and stresses to the standard configuration.

Referring to a domain Ω it is possible to define the optimal design problem as the problem of finding the optimal value Figure 1.8.
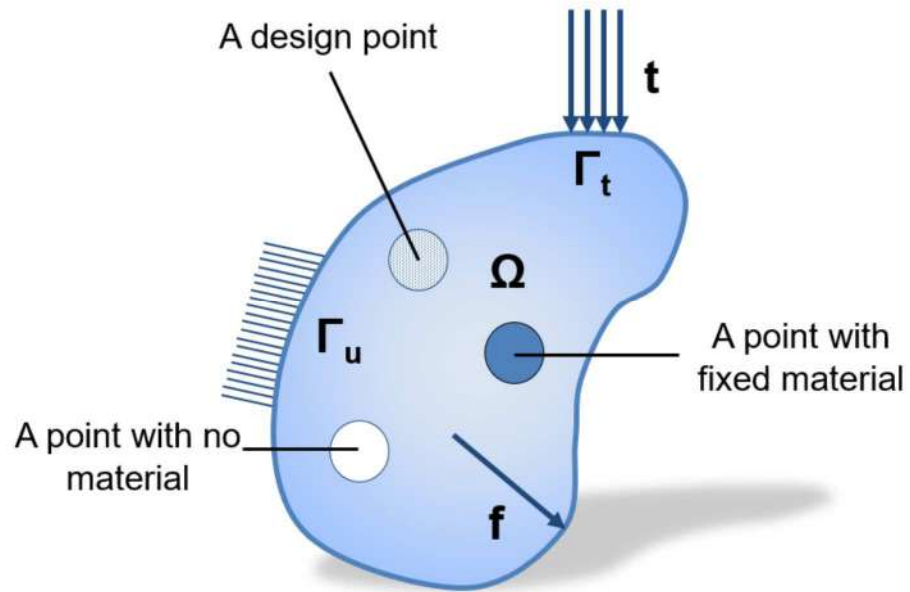
Figure 1.8: The generalized shape design problem for the optimal material [102].

Chapter 2

2. *Cylinder case study*

The cylinder is one of the most common geometries for the underwater vehicles. The candidate's contribution has been the study of applicability of classical and modern theories to the test case, using FEM simulations too. Starting from a brief description of the FeelHippo AUV, which is the reference case for this research activity (Section 2.1), in Section 2.2 there is an overview of the main cylinder studies on buckling failure, with both theoretical and experimental approaches found in the state-of-the-art literature. Section 2.3 concludes the chapter with the obtained theoretical FEM results.

2.1. FeelHippo AUV

FeelHippo AUV [119], shown in Figure 2.1, is an AUV specially designed to be a development platform to test new payload and new control algorithms for both the MDM Lab research group and its students. This is reflected by the vehicle involvement in several monitoring tasks (it has been employed e.g. during the ARCHEOSUb and EUMR projects) and, above all, student competitions, mentioned in Section I.1. For this reason, the design specifications for the vehicle are very simple: light, cheap, small, and with an operating depth of a few meters. In this research study the real depth of immersion and navigation in safety were calculated and found to correspond to about 30 m. FeelHippo AUV is configurable and customizable with different sensors and payloads. It can be easily deployed from a pier or a small boat and it is transportable by two people; its weight in air, thinking to the complete configuration, is about 35 kg.

Figure 2.1: FeelHippo AUV with acoustic devices [120].

The layout of the thrusters imparts FeelHippo AUV with an underactuated motion, with four marine propellers [121] controlling 4 DOFs of the vehicle: two of these are mounted laterally in a V-shape to control the depth and the lateral movement (which is necessary for precise hovering); the other two are mounted in the backside on the horizontal plane, one per side, to control the motion along the longitudinal advancing direction and the yaw angle [122].

The main structure of the vehicle is made of Anticorodal type 6082-T6 aluminium alloy and, PMMA commercially known as Plexiglas® (mechanical characteristics in Table 2.1(EN AW-6082) and Table 2.2 (ISO 527-2)).

Table 2.1: Main mechanical characteristics of Anticorodal type 6082-T6.

Property	Value
Density [kg/m^3]	2700
Yield strength [MPa]	260
Young's modulus [GPa]	68.9

Table 2.2: Main mechanical characteristics of PMMA.

Property	Value
Density [kg/m^3]	1180
Yield strength [MPa]	76
Young's modulus [GPa]	3.3

In Figure 2.2 a CAD of the compact vehicle is shown to highlight its overall dimensions.
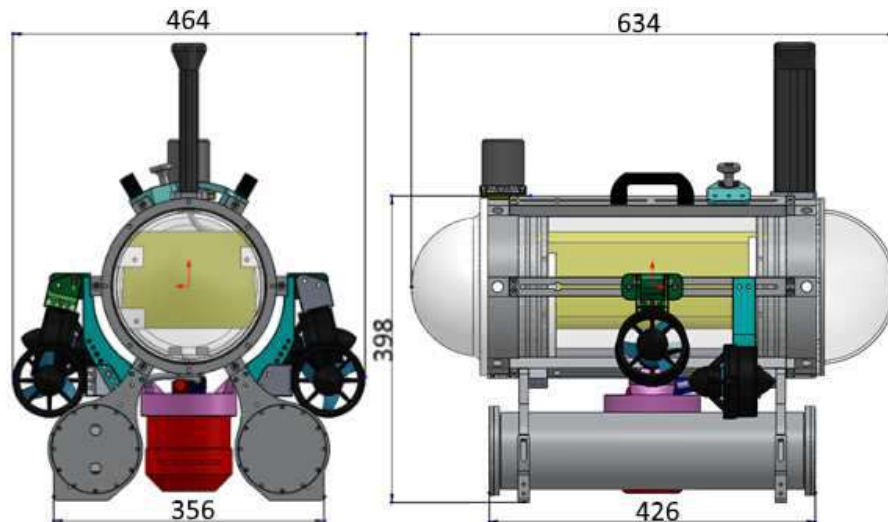
Figure 2.2: Overall dimensions of FeelHippo AUV.

More details are shown in the exploded view drawing of Figure 2.3. The vehicle central body is a PMMA pipe containing the instrumental hardware, and structural connections in Anticorodal type 6082-T6, as well as the two tubes under the main body house the batteries. The body consists of an extruded cylinder and two flanged thermoformed domes. The thermoforming process entails heating a slab of material

to 150–160 °C and then deforming it under vacuum by blowing without a counter-mold to maintain good optical quality.
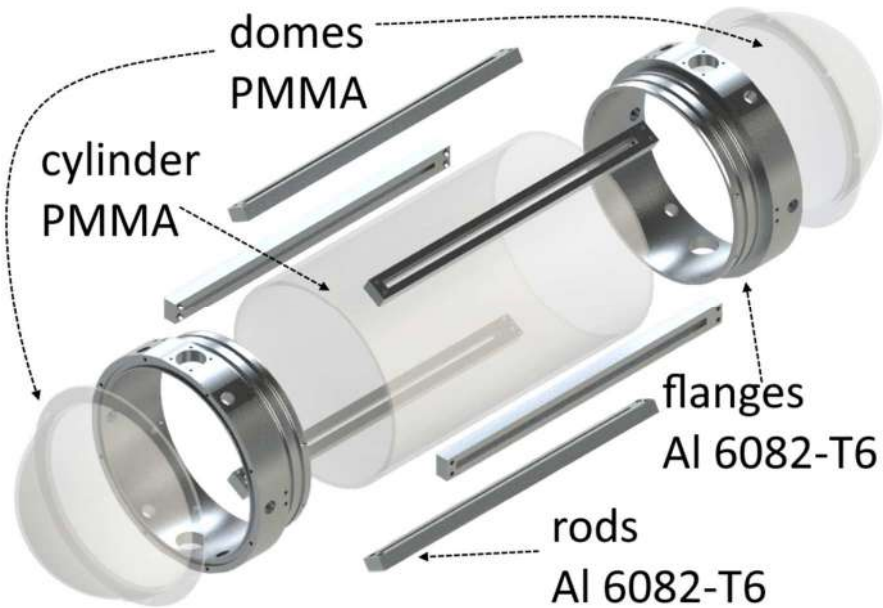
Figure 2.3: Main mechanical structure of FeelHippo AUV.

As discussed in next chapter, this implies that the thickness is variable and that the shape is not perfectly spherical. The choice of materials was dictated by compromising between lightness, strength, and the ability to visually check the electronic components. Other external elements were realized through Additive Manufacturing (AM) in ABS (Acrylonitrile Butadiene Styrene) with a 3D printer from the MDM Lab (Stratasys Dimension Elite) e.g. Figure 2.4

Figure 2.4: Rear thrusters ABS supports.

The differences between the selected materials had a profound influence on the design phase. In fact, the aluminium parts were sized to ensure structural resistance to impacts, which represent another type of possible failure. This choice also ensured that the aluminium parts could endure buckling instability: for this reason, given the

difference in the thicknesses of the various elements, this work performed buckling optimization only for the PMMA components (also because this material has a much lower yield strength and Young's modulus). The PMMA domes and the main tube are connected by 6 aluminium rods and 2 flanges, which are equivalent to ring-stiffeners.

The FeelHippo design is thought to have limited roll and pitch angles during vehicle navigation. This feature is commonly adopted in AUV designs and is obtained by placing its centre of gravity below its centre of buoyancy. In this case, the AUV has a large and light main body, which contains the mainboards and other hardware, and two smaller and heavy legs, which contain the batteries and balancing weights.

In the electronic architecture, the main computer communicates with other devices by means of serial communication (USB (Universal Serial Bus) and RS-232) and an internal Ethernet network; the only exception is for servo command, joining drivers.

Devices connected with serial communication are:

- radio modem to send short messages from high distances on the surface;
- GPS receiver on the surface to quickly localize the vehicle;
- FOG (Fiber Optic Gyroscope), a single-axis gyroscope with high precision to improve the pose estimation (particularly the yaw measurement);
- custom board to monitor internal temperature; it also includes a water leakage sensor, battery SOC, and a control custom beacon flash and status LEDs;
- USB camera to provide frontal images during navigation;
- IMU (Inertial Measurement Unit) MEMS (Micro Electro-Mechanical Systems) to provide data from the 3D internal accelerometer, gyroscope, and magnetometer;
- acoustic modem, which enables a high data transfer rate (13.9 kbit/s) and a high functioning range (3500 m);
- servo driver, an electronic board to control the four outrunner brushless motors.

The other devices, which are connected to each other in a cabled Ethernet network with two switches, are:

- DVL (Doppler Velocity Log), which provides a 3-axial linear speed and altitude measure referred to the seabed using the Doppler effect and the depth of the vehicle by means of an integrated pressure sensor;
- Wi-Fi Access Point, which allows for fast, high-band, short-range communication on the surface;
- 2D forward-looking sonar that allows the vehicle to see obstacles in situations of poor visibility;
- IP cameras to acquire images of the seabed and facilitate 3D reconstruction.

The energy supply that powers the vehicle comprises three LiPo (Lithium Polymer) batteries placed inside the aluminium pipes. In addition, other voltage levels are provided by dedicated DC/DC converters. The main voltage value lines are shown in Figure 2.5, along with the brands and models of the devices.

Once more, all these devices are largely placed in the main PMMA body, stacked on two plastic planes (Figure 2.6), in order to be visible without opening the vehicle too.

Figure 2.5: Power supply for the onboard devices.
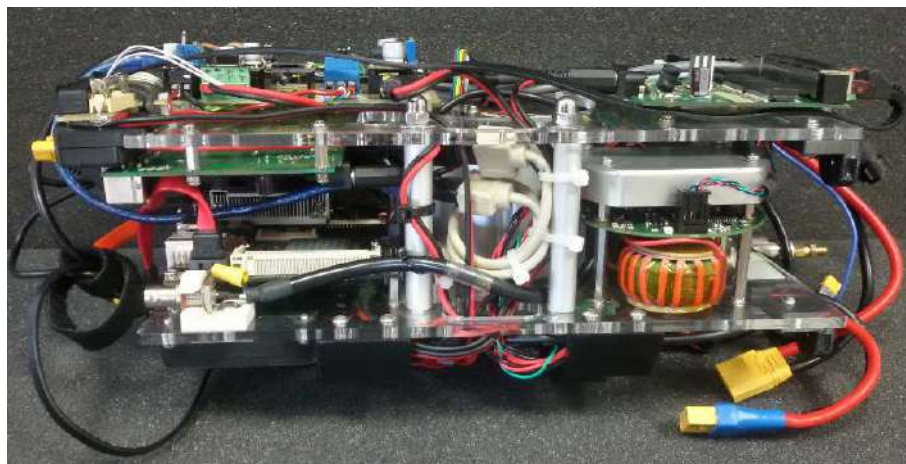
Figure 2.6. Inner electronics of FeelHippo AUV.

2.2. Cylinder theory

In this section, the equations for local instability are given [123]. The critical buckling pressure equations were derived from the buckling analysis proposed both by R. Von Mises and by D.F. Windenburg and C. Trilling. Particular emphasis was placed on the case of submarines that have a circular cylinder, are closed at the ends, and are submerged in water and thus exposed to pressure from all sides [124]. Since thin cylinders subjected to uniform external pressure collapse in an asymmetrical mode (lobar buckling), the local instability was studied at a fraction of the pressure needed to cause axisymmetric yielding. Specifically, an analytical reference formulation for the study of short thin tubes that are supported at the ends and subjected to uniform radial and axial pressure was proposed. The formulation was subsequently modified by Von Mises [68]:

$$P_{crit} = \frac{Et}{R}\left[\frac{1}{n^2+\frac{1}{2}\left(\frac{\pi R}{L}\right)^2}\right]\left\{\frac{\left(\frac{\pi R}{L}\right)^4}{\left[n^2+\left(\frac{\pi R}{L}\right)^2\right]^2}+\frac{\left(\frac{t}{R}\right)^2}{12(1-\nu^2)}\left[n^2+\left(\frac{\pi R}{L}\right)^2\right]^2\right\} \qquad (2.1)$$

$$P_{crit} = \frac{Et}{R}\left[\frac{1}{n^2-1+\frac{1}{2}\left(\frac{\pi R}{L}\right)^2}\right]\left\{\frac{\left(\frac{\pi R}{L}\right)^4}{\left[n^2+\left(\frac{\pi R}{L}\right)^2\right]^2}+\frac{\left(\frac{t}{R}\right)^2}{12(1-\nu^2)}\left[n^2-1+\left(\frac{\pi R}{L}\right)^2\right]^2\right\} \qquad (2.2)$$

where

P_{crit} [MPa] = theoretical buckling pressure Eqn. (2.1), (2.2);

R [mm] = average cylinder radius;

t [mm] = wall thickness;

L [mm] = unsupported length of the cylinder;

E [MPa] = Young's modulus;

ν = Poisson's ratio;

n = number of circumferential waves lobes (an integer that minimizes the expression)

In a precautionary manner, the difference between the real scenario and the theoretical hypotheses was considered by introducing the corrective factor k [91].

$$P_{design} = kP_{crit}$$

$$\qquad (2.3)$$

where k varies according to t:

k = 0.4 for t < 5 mm

k = 0.5 for 5 < t < 7 mm

k = 0.6 for t > 7 mm

P_{design} = operative pressure at which the vehicle can dive and navigate safely Eqn. (2.3).

A second theoretical expression, Eqn. (2.4), has been proposed by D.F. Windenburg and C. Trilling, and does not depend on the number of lobes [69]:

$$P_{crit} = \frac{2.42E}{(1-v^2)^{\frac{3}{4}}} \left[\frac{\left(\frac{t}{2R}\right)^{\frac{5}{2}}}{\frac{L}{2R} - 0.45\left(\frac{t}{2R}\right)^{\frac{1}{2}}} \right]$$

(2.4)

More recently, another approach has been formulated to propose more targeted correction factors starting from the interpolation of experimental data: Ross presented a comparison between the theoretical models, the experimental results, and simulated results [75]. For instance, Figure 2.7 (which has been graphically improved without modifications in contents) reports the results for an Anticorodal 6082-T6 tube with the outer diameter $2R + t$ = 50 mm and t = 1.7 mm.
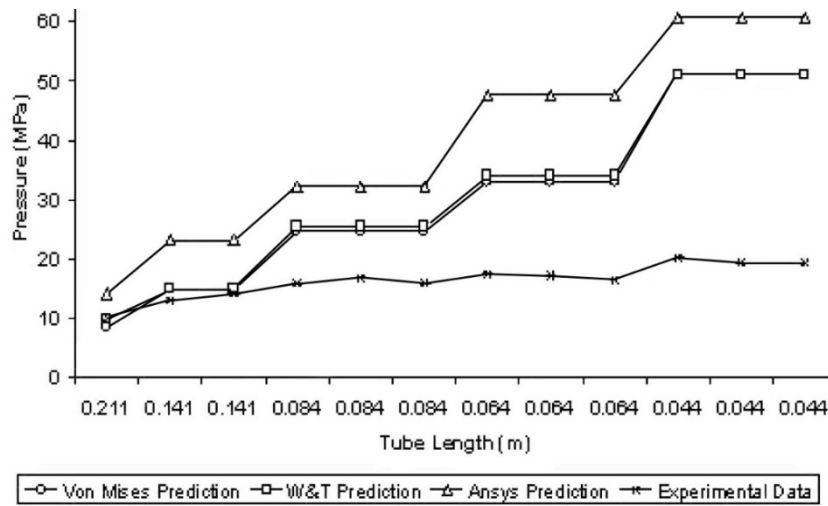
Figure 2.7: Predicted buckling pressure versus tube length [69].

The literature also includes graphs to calculate the pressure that is actually bearable by the cylinder according to its geometric characteristics and its material. The calculations are based on both a theoretical basis and experimental results; therefore, the results are even more reliable. E.g. Figure 2.8 presents a design chart for thick-walled machined circular cylinders that collapse under external hydrostatic pressure; the linearity of the graph in the "plastic" area, where the PKD (Plastic Knock Down factor) is much larger than the unit, seems to indicate that it will prove to be a very useful design tool [68].

$$\lambda_c = \left[\frac{\left(\frac{L}{2R}\right)^2}{\left(\frac{t}{2R}\right)^3} \right]^{\frac{1}{4}} \left(\frac{\sigma_y}{E}\right)^{\frac{1}{2}}$$

(2.5)

$$PKD = P_{crit} / P_{exp}$$

(2.6)

where

σ_y [MPa] = yield strength;

λ_c = slenderness of the cylinder Eqn. (2.5);

P_{exp} [MPa] = the experimentally obtained buckling pressure, which is ultimately an intermediate value between the theoretical and safety pressures and specifies the pressure at which the geometry could start collapsing Eqn. (2.6);

PKD = Plastic Knock Down factor, the ratio between the theoretical and experimental pressures.
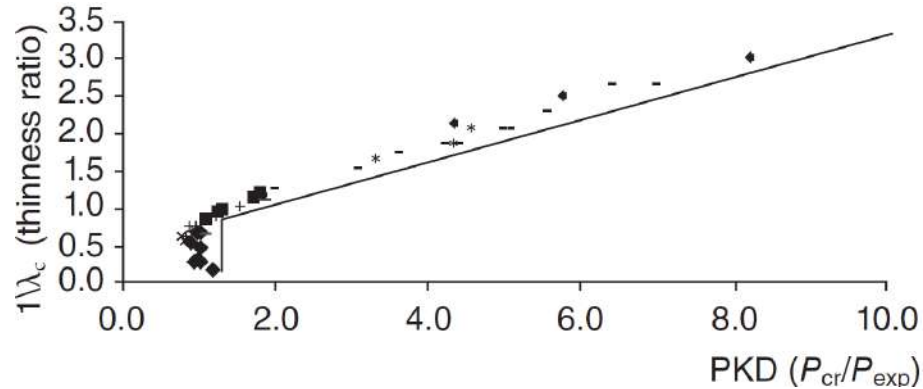
Figure 2.8: Design chart for the shell instability [75].

For the sake of clarity, the interpolated points derive from several experimental observations, e.g. of Sturm (diamond symbol in the chart [125]), Reynold (full squares [126]), Seleim and Roorda (grey hyphen [127]), Hom and Couch (plus sign [128]), and some different Ross's studies (asterisk [129], multiplication sign [130], minus sign [68], dot [131] and triangle [132]). Figure 2.9 presents another different design chart for machined ring-stiffened cylinders [133].
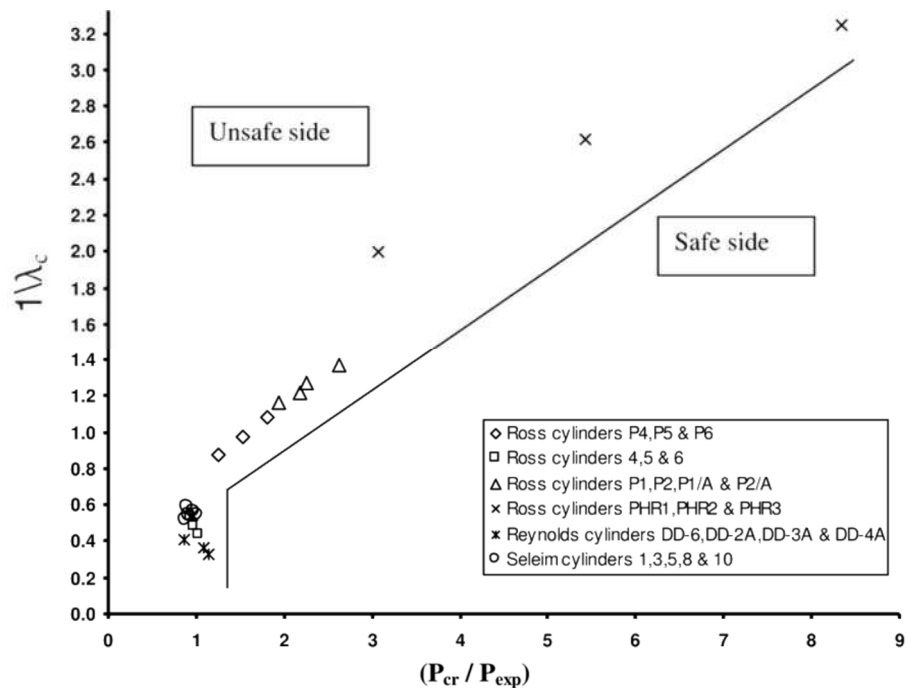
Figure 2.9: Design chart for the general instability (ANSYS) [133]

38

In addition, a safety coefficient (*SF*) < 3 e.g., arbitrarily 1.5 is included Eqn. (2.7) to obtain the real design operative pressure (a value of 3 is used for the case in which people are on board). It can be seen that if $1/\lambda_c < 0.9$, the structure will probably fail by elastic instability, followed by axisymmetric deformation. Additionally, there is a link between plastic axisymmetric deformation and inelastic shell instability.

$$P_{design} = \frac{P_{exp}}{SF}$$

(2.7)

The ability to withstand pressure is reduced if the cylinder is manufactured with an initial out-of-circularity. Comparing experimental and theoretical data reveals that as the length of the cylinder decreases, the theoretical data deviate from the experimental evidence (Figure 2.8) because of edge effects, too. Therefore, corrective factors are needed to ensure a certain safety margin.

2.3. Cylinder theoretical and FEM results

In this section, the study of the cylindrical component of the FeelHippo AUV has been collected. For the geometry of FeelHippo AUV, in accordance with the aforementioned nomenclature, the cylinder geometrical data together with the material properties are summarized in Table 2.3.

Table 2.3: Geometrical cylindrical data.

R [mm]	*t* [mm]	*L* [mm]	*E* [MPa]	*ν*
107.5	5	272	3300	0.39

First, the theoretical critical buckling pressure (the pressure at which the hull would collapse under ideal conditions) was calculated. Table 2.4 summarizes the theoretical pressure for the case under examination: the first two columns identify the cylindrical thickness and the number of lobes; the third column reports the values from Eqn. (2.1), the fourth column reports the values from Eqn. (2.2), the fifth column reports the values from Eqn. (2.4), and the last column reports the results of the FEA described below. The values are quite similar among the various formulations.

Table 2.4: Theoretical buckling pressure obtained values.

t [mm]	*n*	*Von Mises* Eqn. (2.1) [MPa]	*Von Mises* Eqn. (2.2) [MPa]	*Windenburg Trilling* Eqn. (2.4) [MPa]	*FEM* [MPa]
5	4	0.67	0.64	0.62	0.64

The necessary geometry was obtained by carrying out sizing optimization to perform a FEM comparison and an evaluation of the minimum volume of material, that is, the minimum thickness of the cylinder to withstand the calculated pressure, slightly less than 0.7 MPa. As a result, a uniform external pressure was applied to the structure while an equivalent axial load was imposed on the frontal section. The first thickness

was set to 10 mm to avoid influencing the test. After several iterations, the solver identified a minimum necessary thickness of 5.08 mm, which can be reasonably approximated to 5 mm.

Figure 2.10 and Figure 2.11 show a qualitative representation of the results of the FEA using SOLIDWORKS.
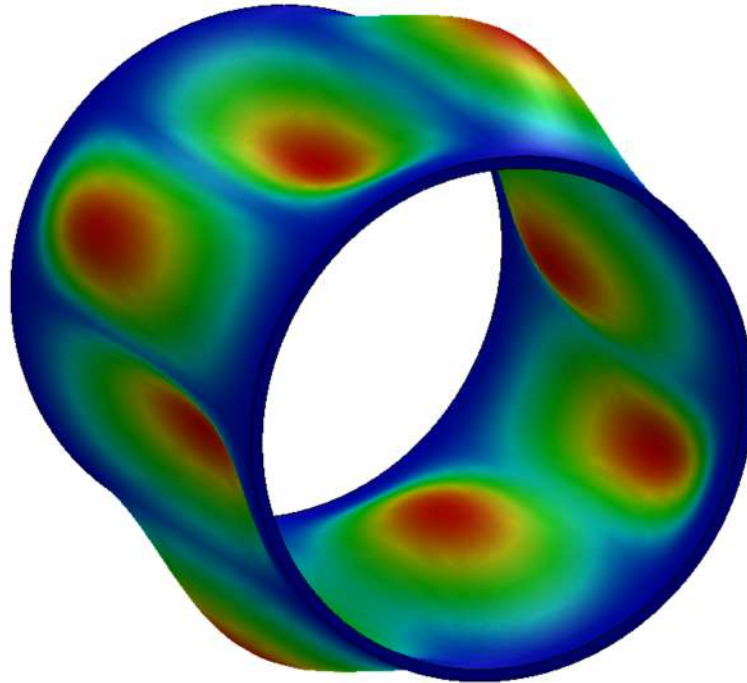
Figure 2.10: Optimized cylinder perspective view, first buckling mode.
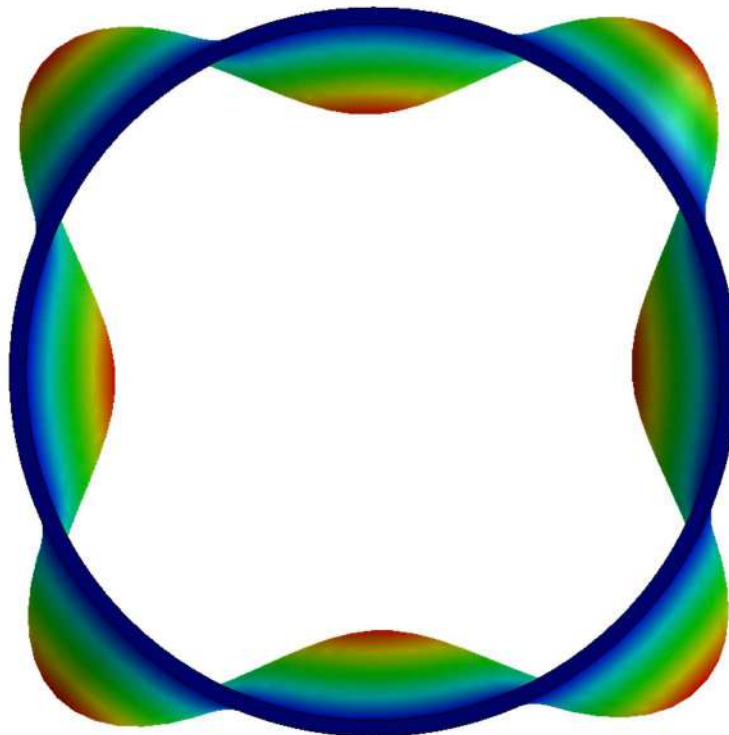
Figure 2.11: Optimized cylinder frontal view, first buckling mode.

Both ends are interlocked to simulate the behaviour of the rods. A tetrahedral solid curvature-based mesh was chosen, with 3308688 elements and 4899890 nodes. There is a complete match between the FEA results and the theoretical results derived from Von Mises's theory.

The number of circumferential lobes is 4, which is in agreement with both Eqn. (2.1) and Eqn. (2.2). The Buckling Factor of Safety (BFS), ratio of the buckling loads to the applied loads, is slightly less than 1, so the applied loads exceed the estimated critical loads and buckling is expected (BFS = 0.91). To make the deformed configuration and the resulting lobes visible, a deformation scale (DS) has been set. The deformation scale refers to the scale factor that the program uses to scale the deformed shape of the model, the value of the scale factor depends on the model's largest dimension and the calculated deformations; in this case DS = 54, means that the largest deformation calculated by SimulationXpress is shown as 54% larger than the largest dimension of the smallest boundary box that surrounds the model.

The first eight buckling modes of the cylinder are shown in the Figure 2.12.
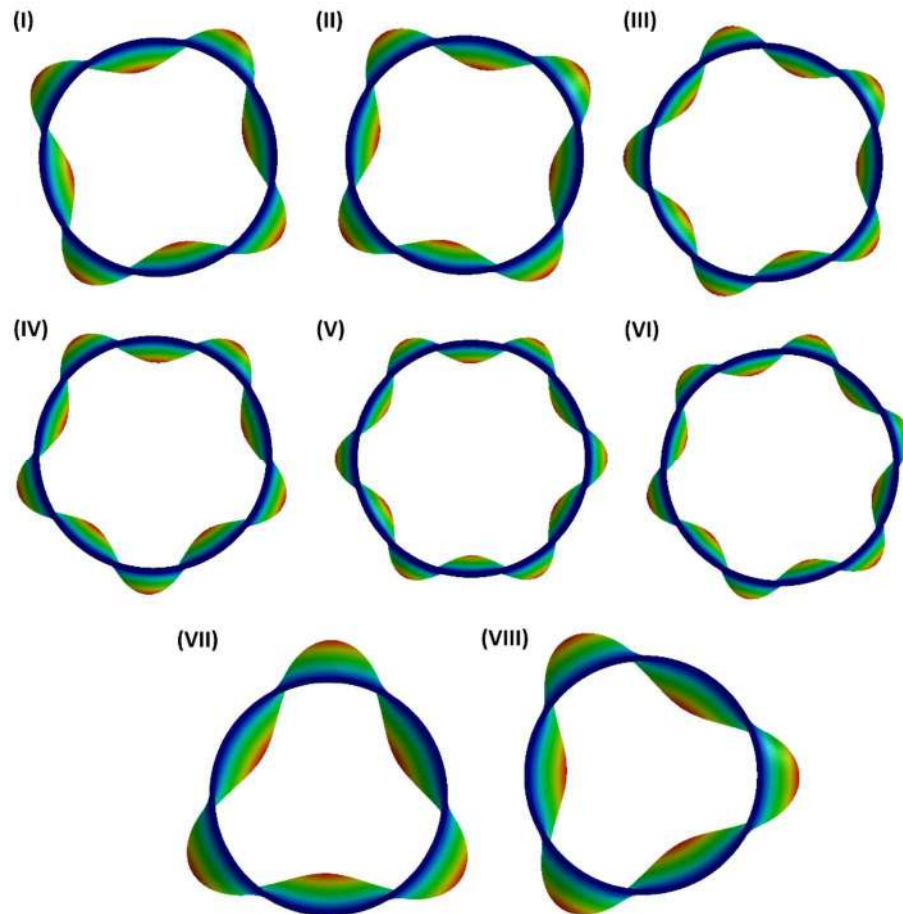
Figure 2.12: First buckling mode shape of the cylinder (DS = 50).

The last step includes the derivation of the real critical buckling pressure by using both the classical and experimental methods. In sum, the first method uses the theoretical value of the pressure derived by R. Von Mises' or D.F. Windenburg and C. Trilling's equations, with corrections applied by using the corrective factor k. The second (experimental) method corrects the theoretical value through experimental

charts (λ_c and *PKD*) and the safety coefficient *SF*. From the chart in Figure 2.8 and Figure 2.9, it is possible to calculate the coefficient λ_c, particularly λ_c = 2.87 (Eqn. (2.5)), to find the value of *PKD* ~ 1.3 and, consequently, P_{exp} = 0.49 MPa (Eqn. (2.6)), which is the experimental bearable pressure value. Using a safety factor (Eqn. (2.7)) *SF* = 1.5, the design pressure P_{design} = 0.32 MPa (about 30 m) is obtained. This is the same value that results from using the safety coefficient *k* = 0.5 and P_{crit} of Eqn. (2.1) in Eqn. (2.3). To further verify the yielding resistance, a static analysis was also carried out; the obtained results are shown in Figure 2.13 and Figure 2.14.
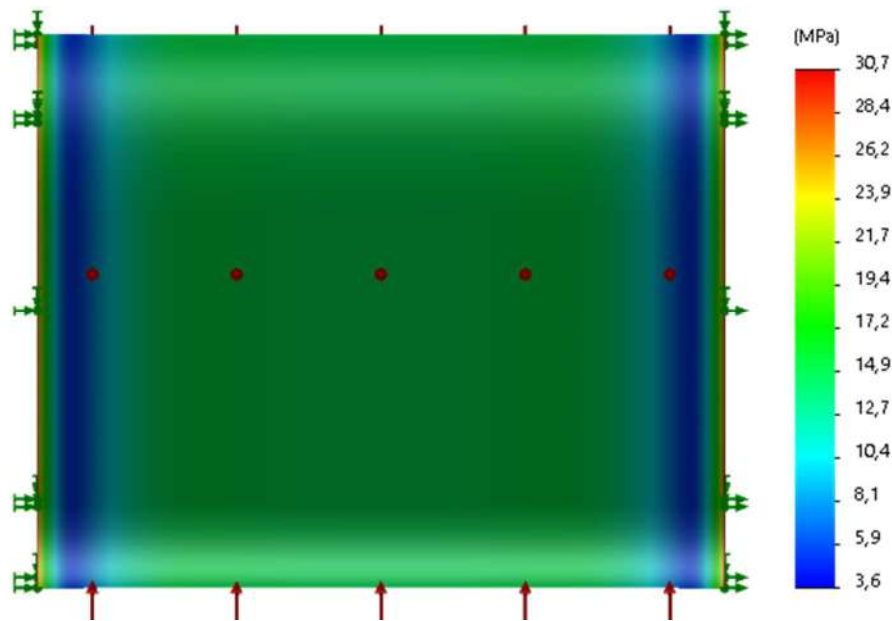
Figure 2.13: Static analysis results: stresses (cylinder lateral view).
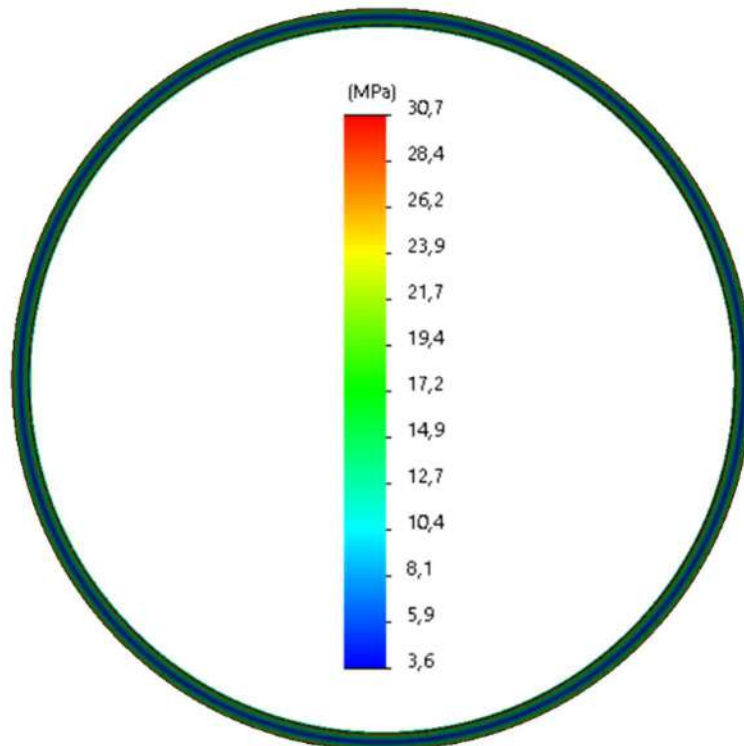
Figure 2.14: Static analysis results: stresses (cylinder frontal view).

The stresses are considerably lower than the yield stress, confirming that for this geometry buckling is the dominant phenomenon. In conclusion, the operative depth obtained for the case under examination is about 30 m; obviously this depth is linked to the PMMA use, if greater depths are desired, a change of material would be sufficient.

A theoretical investigation was also carried out for other cases that have been tested by other researchers [134]; this makes the validation more credible if the same results are obtained. Table 2.5 summarizes the buckling pressure data found: specifically, it presents the geometric data of the two aluminium tubes tested by BlueRobotics, their experimentally detected critical buckling pressures, and finally, the theoretical results derived from the FEA and Eqn. (2.1). The number of lobes is the same in each of the three cases. It is reasonable to assume that the tested cylinders are almost free from imperfections in addition to having an excellent geometric ratio.

Table 2.5: Comparison with BlueRobotics data [134].

| R [mm]	t [mm]	L [mm]	Experimental Collapse [MPa]	FEM [MPa]	Von Mises Eqn. (2.1) [MPa]	n
43.45	2	180	7.5	7.25	7.55	3
55.95	2.4	239	6.1	5.91	6.11	3

2.4. Conclusions

One of the most common geometries in the underwater field is the cylinder; the failure of this structure is widely studied. When the compressive stresses generated by the external pressure reach high levels, the phenomena of instability become predominant and the collapse of a circular cylinder occurs with an external pressure that is a small fraction compared with the one to be internally applied. This geometry has been used to approach the collapse theories and become familiar with the buckling phenomenon and the related design methods. The here specific study concerns an extruded plastic cylinder, which constitutes the main body of the underwater vehicle under study. It is possible to identify three meaningful pressures: the first one is theoretical, and, as it does not take into account imperfections in geometry or material, to determine the operating pressure it is divided by a high safety coefficient; the second one is experimental, and identifies the pressure at which the collapse phenomenon should really occur; the third one is the operating pressure at which diving and navigation is safe. In the technical literature there are mainly two approaches: the first, classic, one follows theoretical formulations and identifies the theoretical precautionary pressure of failure; the second one, more empirical, exploits experimental data to identify the pressure at which the failure should begin. The objective of this first phase of research was to verify the applicability of the methods to the case in exam and their usability in a first design phase even without the use of computationally costly simulations. With both approaches the same result was found, also confirmed by both a sizing optimization and a FEM analysis.

Chapter 3

3. *Dome case study*

The spherical shape is another of the most common geometries for the underwater vehicles, however, the studies in the technical literature are a few and not well suited if the case of flanged thermoformed domes is considered. This is because whatever additional production technique is employed, the dome thickness is never uniform [71]; the boundary conditions are another not inconsiderable factor [70]. An example of targeted study of specific geometric imperfections in buckling prediction theories is given here [135]. The candidate's original contribution has consisted in analysing the experimental data obtained, proposing modifications to extend the classical theory of domes, which has been enriched, and validate through a FEM study. In Section 3.1 there is a brief overview of the classical studies on dome collapses found in the state-of-the-art literature. Starting from a reduced experimental campaign, with the available samples (Section 3.2), the research study has been developed. Section 3.3 concludes the chapter with the proposed theoretical improvements and obtained results, with the aim of validating the here proposed approach [120].

3.1. Dome classical theory

It has been observed that the dome geometry can collapse in different manners depending on certain parameters. First, two equations from the literature are reported ([136], [137], [73]).

The first equation calculates P_{crit}, the theoretical critical buckling pressure for a thin sphere Eqn. (3.1):

$$P_{crit} = \frac{2}{\sqrt{\left[3\left(1-v^2\right)\right]}} \frac{Et_s^2}{R^2}$$

(3.1)

The second equation is related to the critical static compression pressure (based on large-deformation theory of shells) that causes membrane yield in the sphere P_c Eqn. (3.2):

$$P_c = 0.365E\left(\frac{t_s}{R}\right)^2$$

(3.2)

Since these equations represent two different failure modes, each one is valid for a specific field of application, and it is worth noting that their results could not be the same. Compared with the previous notation, it is important to highlight that

R [mm] = the radius of the hemisphere to mid-thickness;

t_s [mm] = the nominal dome thickness;

and, as before,

E [MPa] = Young's modulus;

ν = Poisson's ratio.

As one might expect, a hemispherical dome has a better buckling resistance than other kinds of domes. Indeed, hemi-ellipsoidal prolate and hemi-ellipsoidal oblate domes are ten times less robust than hemispherical domes. Experimental tests [75] have shown that the structural failure of domes occurs for values of critical pressure lower than those theoretically predictable by the formulas above.

The technical literature reports many specific correlations but only for very limited fields of application, the greatest limit of these results is the experimental peculiar conditions [93]; for instance, in Table 3.1, some of the coefficients proposed for the multiplicative constant value of the Eqn. (3.1) are given, elastic buckling of spherical shells under external pressure. The aim of this work is to extend the field of application of the available values. An alike problem, which was found to be inherent in the difficult task of linking a coefficient to a constraint type, was discussed in [138].

Table 3.1: Examples of multiplicative constant [93].

Constant	Due to
$\dfrac{1.16}{\sqrt{1-\nu^2}}$	Zoely
0.365	Von Karman, Tsien
0.283	Thompson
0.220	Mushtari
0.126	Dostanova, Raizer
f(R/t)	Others

The comparison between the theoretical data and the experimental data derived in the next section is not satisfactory, (Table 3.4, in the last columns there is the ratio of theoretical values to experimental measure).

Table 3.2: Comparison between experimental and theoretical formulations.

t_s [mm]	Experimental Collapse [MPa]	P_{crit} (Eqn. (3.1)) [MPa]	P_c (Eqn. (3.2)) [MPa]	$\dfrac{P_{crit}}{P_{exp}}$	$\dfrac{P_c}{P_{exp}}$
3	0.22	3.90	1.13	18	5
6	1.35	16.08	4.68	12	4
10	1.45	45.14	13.14	31	9

Hence, there is a need to introduce corrections to predict the behaviour of the case under study. This process starts from the theoretical critical buckling pressure of a hemispherical dome (P_H, Eqn. (3.3)) and the ideal yield pressure for hemispherical and homogeneous domes (P_y, Eqn. (3.4)). In this study, the variation in thickness, the AR, and the type of constraint were taken into account, given their non-negligible influence.

$$P_H = \frac{2Et_H^2}{R^2\sqrt{\left[3\left(1-v^2\right)\right]}}$$

(3.3)

$$P_y = 2\left(\frac{t_H}{R}\right)\sigma_{yield}$$

(3.4)

The collapse pressures obtained from experimentation are generally less than those calculated using theoretical formulas because of the geometric imperfections of the real domes. Furthermore, in the case studied, the geometry strongly depends on the manufacturing method. The use of PMMA as a material allows for an appropriate balance between inexpensiveness, optical properties, and mechanical strength. Nevertheless, in the state-of-the-art literature, only a few studies have been conducted on thermoformed flanged domes, which usually have a shape that considerably diverges from the ideal spherical shape as a direct result of the production process [71]. The structural characteristics of the objects realized in this type of production process vary according to their geometric characteristics, and they heavily differ from those produced by other production techniques. Unfortunately, therefore, the experimental theories derived from case studies in the literature [75], [139] although suitable for highly regular domes, cannot be directly applied to the thermoformed PMMA ones. The research objective is to study the problem of structural collapse for thermoformed flanged domes and to extend the classical theoretical formulations on structural collapse in the technical literature to this specific test case while considering the significant variation in the thickness [140] and AR, together with the constraints [70]. Thus, the theories and equations were modified, verified, and compared with the results of the FEM analysis.

3.2. Experimental campaign

Some experimental tests were carried out in the UniFI DIEF MDM Lab pressure chamber, approach Figure 3.1. Its technical characteristics are:

Figure 3.1: MDM Lab pressure chamber.

- material: high-strength steel;
- operating fluid: freshwater;
- dimensions: horizontal length of 2 m and diameter of 400 mm;
- maximum working pressure: 35 bar.

Nine specimens, three for each thickness, suitably constrained, have been broken thanks to a step increase in hydrostatic pressure (each step of 0.25 bar has been held for 5 seconds to identify the breaking value); the objective has been the detection of the ways of failure connected to the collapse pressures; the main geometrical features of the tested samples are summarized in Table 3.3, while the followed procedure is here below explained with the help of images taken during the experimental campaign. Regarding the nomenclature: t_s denotes the nominal thickness of the slab, available on supplier catalogues; R denotes the mean radius of the dome base; h denotes the height of the dome, from the upper face of the flange to the external upper part of the dome; lastly, R_f is the external radius of the flange.

Table 3.3: Geometrical features of specimens.

| t_s | h | R | R_f |
[mm]	[mm]	[mm]	[mm]
3	98	97.75	230
6	95	96.25	230
10	91	95.75	230

Each component, i.e., each dome with different features, was tested together with other more resistant components to avoid influencing the test with other collapses. Each test was performed three times, and the same result was obtained in each trial; while recognizing that a larger, more expensive, experimental campaign would be necessary, the obtained results are significant to characterize the specific case of interest, i.e. thermoformed and flanged PMMA domes:

- two domes were held together by the torque tightening of 8 screws , divided by a protective flat seal (Figure 3.2);
- the hydrostatic pressure was raised step by step and maintained;
- the collapse pressure was detected using the manometer (accuracy ±0,5%, just near the buckling collapse in Figure 3.3);
- after depressurization, each element was checked (Figure 3.4 and Figure 3.5 show examples of yielding collapse occurring close to the flange, Figure 3.6 and Figure 3.7 cases of buckling failure occurring on the top of the dome).

The obtained results, collapse pressure and type of collapse, are summarized in Table 3.4; for clarity the data have been referred to the nominal thickness of the slab, t_s.; experimental evidence has shown that the mode of dome breakage varies according to the nominal thickness [120].

Table 3.4: Dome experimental data.

t_s [mm]	Experimental Collapse [MPa]	Predominant phenomenon
3	0.22	buckling
6	1.35	yielding
10	1.45	yielding

Figure 3.2: Example of two joined domes before testing.

Figure 3.3: Pressure chamber manometer.

Figure 3.4: Check of breaking mode, first yielding example.
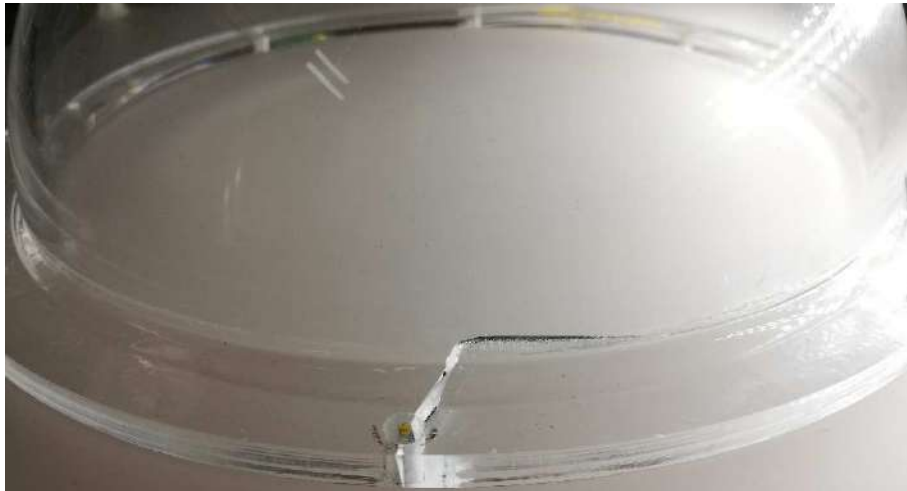
Figure 3.5: Check of breaking mode, second yielding example.

Figure 3.6: Check of breaking mode, first buckling example.

Figure 3.7: Check of breaking mode, second buckling example.

3.3. Dome theoretical and FEM results

First of all, the change in geometry was taken into account by comparing the values taken from technical manuals and the physical domes.

In the flange part, the thickness, t_s, is the nominal thickness of the PMMA plate, but the thickness decreases as it approaches the centre of the dome, as shown in the chart in Figure 3.8. Hence, for safety, the thickness used is t_H, which is the minimum of the dome (to clarify, in Table 3.5, the geometrical data are as follows: R is the mean radius, h is the height of the dome, and d is the external radius of the dome; all three variables do not consider the flange). The blue dotted line is the interpolation performed in this study (Eqn. (3.5)) [141].

Table 3.5: Geometrical data.

t_s	R	h	d	t_H
[mm]	[mm]	[mm]	[mm]	[mm]
2	98.25	99	199	0.64
3	97.75	98	199	0.99
4	97.25	97	199	1.34
5	96.75	96	199	1.71
6	96.25	95	199	2.10
7	96.25	94	199	2.50
8	95.75	93	199	2.91
9	95.75	92	199	3.34
10	95.75	91	199	3.79
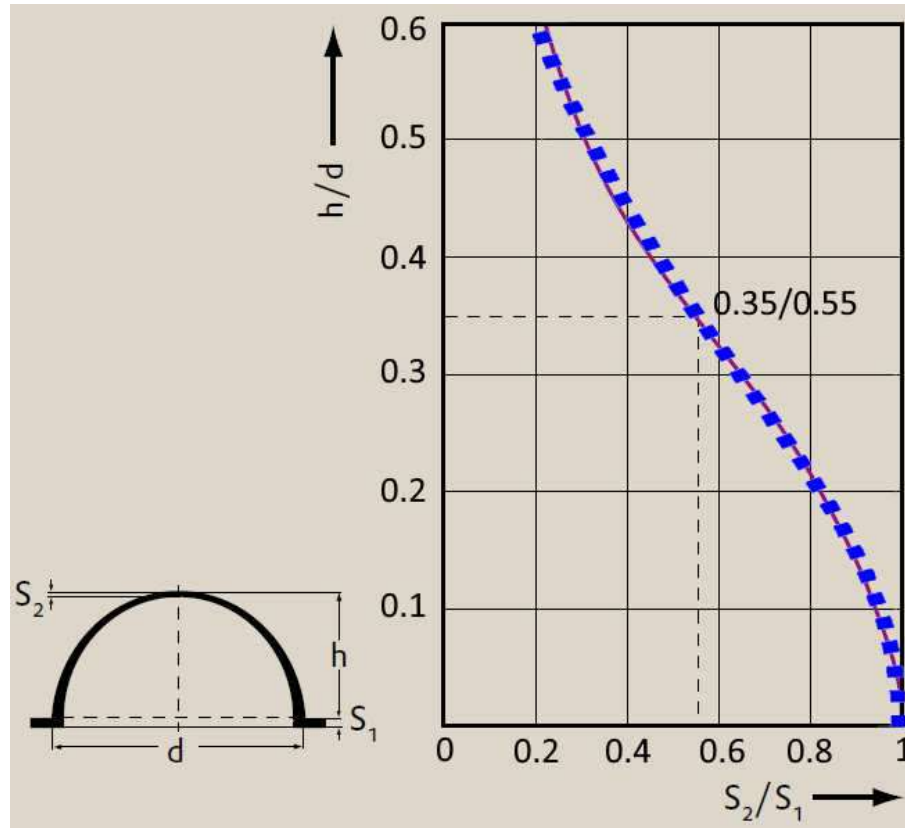
Figure 3.8: Thickness of a blowing produced dome [141].

$$\frac{S_2}{S_1} = s_4 + \frac{s_1 - s_4}{1 + \left(\dfrac{\dfrac{h}{d}}{s_3}\right)^{s_2}} \tag{3.5}$$

where S_1, S_2, h, and d are geometrical quantities and shown in Figure 3.8; $S_1 = t_s$ and $S_2 = t_H$; and s_1, s_2, s_3, and s_4 are interpolation coefficients (collected in Table 3.6)

Table 3.6: Interpolation coefficient for Eqn. (3.5).

s_1	s_2	s_3	s_4
0.993	2.224	0.454	-0.224

If the changes in the parameters are considered to be independent of each other in the first approximation, then the variation in the geometry, thickness, and constraints can be analysed. It has been observed that an imperfectly spherical shape influences the mode of dome breakage: as the thickness increases, the influence of the membrane buckling behaviour decreases and favours yielding, while the point of breakage moves from the top of the dome to the flanged base, close to the constraint. Furthermore, in the thickest domes, the radius of the inner curvature between the dome and the flange greatly influences its breaking behaviour under compression, but this geometric parameter depends on the thermoforming process and thickness: the

greater the thickness, the greater the radius and, consequently, the greater the mechanical stresses of the section. This is because the dome tends to overturn. On the other hand, as the radius of the external curvature between the flange and the dome decreases, local tensions increase. This justifies a sublinear trend. Another difference, which is discussed in the following part, is the *AR*, distance from the unit, together with the presence of holes in the flange, and an imperfect hemispherical shape.

The purpose of this study is to derive a simplified and efficient method for the case under study and integrate the problems related to the AR and constraints into the calculation to identify the limit between compression and buckling [120].

The formulation of the theoretical critical buckling pressure (Eqn. (3.3)) can be corrected using the *AR* (*R/h*), which is dependent on the parameters of the dome and non-negligible in this particular case. In Figure 3.9, a graph from the literature, showing the trends of elastoplastic buckling loads for different thickness ratios of the reference hemisphere is given; in this chart the coloured dotted lines represent the interpolation performed in this study. Below are the relationships used to interpolate the graph. First is the initial linear part (based on a linear function) (Eqn. (3.6)); second is the nonlinear part (based on the power curve) (Eqn. (3.7)), and third is the scaling based on R/t_H (based on symmetrical sigmoidal) (Eqn. (3.8)).

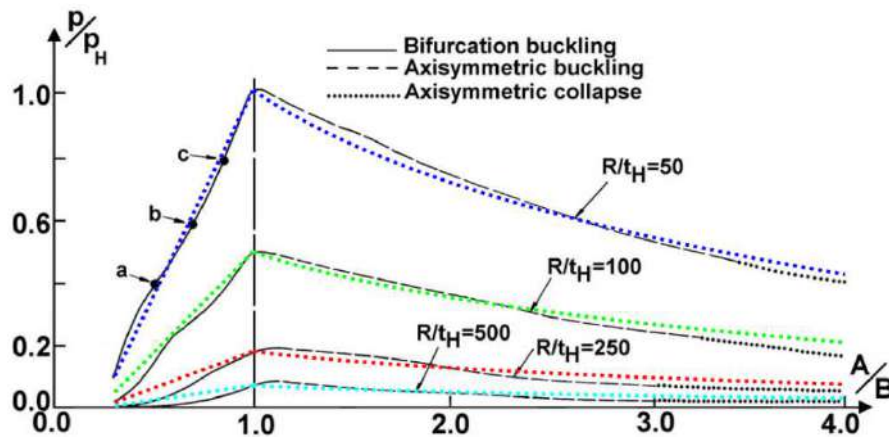**Figure 3.9: Elastoplastic buckling loads [142].**

$$\left(\frac{P}{P_H}\right)_k = f_k\left[l_1\left(\frac{A}{B}\right) + l_2\right]$$

(3.6)

$$\left(\frac{P}{P_H}\right)_k = f_k\left[n_1\left(\frac{A}{B}\right)^{-n_2} + n_3\right]$$

(3.7)

$$f_k = q_4 + \frac{q_1 - q_4}{1 + \left(\dfrac{\dfrac{R}{t_H}}{q_3}\right)^{q_2}}$$

(3.8)

52

In the above equations, l_1, l_2, n_1, n_2, n_3, q_1, q_2, q_3, and q_4 are interpolation coefficients (collected in Table 3.7); A/B is the reciprocal of AR in Figure 3.9, with $R = A$ and $B = h$; P_H is the theoretical critical elastic buckling pressure of a hemispherical dome (Eqn. (3.3), substituting the nominal t_s to Eqn. (3.1) with t_H); and P is the theoretical critical buckling pressure for a non-hemispherical dome.

Table 3.7: Interpolation coefficient for Eqn. (3.6) – (3.8).

l_1	l_2	n_1	n_2	n_3	q_1	q_2	q_3	q_4
1.286	-0.286	2133.4	-0.0002	-2132.4	214528.5	0.969	0.0002	-0.041

As regards the border between compression and buckling behaviour, the parameter λ_d is considered. Starting from the state-of-the-art literature [143], λ_d (Eqn. (3.9)) expresses a ratio between pressures and a relationship between geometric and material features.

$$\lambda_d = \sqrt{\frac{P_y}{P_H}} = \sqrt{\left(\frac{R}{t_H}\right)\left(\frac{\sigma_{yield}}{E}\right)\sqrt{3(1-\nu)}} \tag{3.9}$$

where P_y = ideal yield pressure of hemispherical and homogeneous shell, considering the t_H (Eqn. (3.4)).

From the experimental results, it was observed that if $\lambda_d < 1$, then the rupture occurs because of the static compression load. On the other hand, if $\lambda_d > 1$, then the buckling phenomenon occurs.

It is highlighted that the mechanics of the fracture depend on the type of constraint, the material, its stiffness, and the specific production method. For example, with consideration of only the constraint, in the particular case under examination, there are holes for connecting screws, and a peak of stress in their surroundings causes a crack and a brittle break that promote the initiation of the collapse.

A corrective factor is introduced (f_y) to take into account these effects. In this way, the theoretical corrected pressure (P_{yc}) (Eqn. (3.11)) matches the experimental one. The correction factor is based on a power curve Eqn. (3.10) derived from FEA, and it is dependent on the dome thickness, (y_1 and y_2 in Table 3.8).

$$f_y = y_1 t_s^{y_2} \tag{3.10}$$

$$P_{yc} = \frac{P_y}{f_y} \tag{3.11}$$

Table 3.8: Interpolation coefficient for Eqn. (3.10).

y_1	y_2
0.383	1.034

The influence of the correction of the coefficient λ_{dc} (Eqn. (3.12)), λ_d but with corrected pressures, follows a square root law, while the coefficient f_y follows a power one. Therefore, the transition point of collapse is also affected. As a result of applying this coefficient, the theoretical data coincide with the experimental evidence, as summarized in Table 3.9: for the three nominal thicknesses of which the experimental value is available, the conversion of the theoretical values P_H and P_y, in which the minimum thickness was considered, has been collected, taking into account the aspect ratio for the buckling phenomenon and the corrective constraint coefficient for yielding. The minimum theoretical value between buckling and yielding collapse pressures are in bold and stress the type of break.

$$\lambda_{dc} = \sqrt{\frac{P_{yc}}{P_H}} \tag{3.12}$$

Obviously, similar to the case with the cylinder, a safety factor for the dome (e.g. SF_d = 1.25) has to be considered to obtain the pressure design. This starts from the minimum pressure between $P_{designDY}$ for yielding and $P_{designDB}$ for buckling, the pressure at which the vehicle could dive safely.

$$P_{designDY} = \frac{P_{yc}}{SFd} \tag{3.13}$$

$$P_{designDB} = \frac{P}{SFd} \tag{3.14}$$

Table 3.9: Comparison between obtained theoretical and experimental data.

t_s [mm]	Exp [MPa]	Buckling			Yielding			λ_{dc}
		P_H [MPa]	AR	P [MPa]	P_y [MPa]	f_y	P_{yc} [MPa]	
3	**0.22**	0.42	1.00	**0.21**	1.53	1.19	1.29	1.75
6	**1.35**	1.97	0.99	2.16	3.31	2.45	**1.35**	0.86
10	**1.45**	6.48	0.95	12.66	6.02	4.15	**1.45**	0.49

As discussed, FEM analysis was performed, although with different thicknesses from those experimentally tested (Table 3.10), to both validate the proposed relationships of buckling pressure and delineate the correction curve for theoretical compression breakage (in the column of the FEA results, only the real collapse pressure is reported; it is a sublinear trend, as is the experimental one).

Table 3.10: Comparison between theoretical and FEM data.

t_s [mm]	Experimental collapse [MPa]	Buckling FEM [MPa]	Buckling P [MPa]	Yielding FEM [MPa]	Yielding P_{yc} [MPa]
2	-	**0.04**	**0.06**	-	1.27
3	**0.25**	**0.22**	**0.21**	-	1.29
4	-	**0.55**	**0.55**	-	1.31
5	-	**1.17**	**1.16**	-	1.33
6	**1.35**	-	2.16	**1.35**	**1.36**
7	-	-	3.62	**1.38**	**1.38**
8	-	-	5.82	**1.41**	**1.41**
9	-	-	8.75	**1.43**	**1.43**
10	**1.45**	-	12.66	**1.45**	**1.45**

Given the difficulty of identifying the yielding breaking state, a system of constraints suitable for the case under examination was to set up by using experimental data. In particular, the static analysis of the 10 mm thick dome is reported in Figure 3.10. The results of the intermediate domes were used to define the corrective relationship. The bolts in stainless steel AISI 316, A470 EN ISO 3506, were inserted as connectors and simulated with their pretension clamping force set to 3760 N, which is equivalent to nominal tightening. The lower face of the flange was fixed, while the contact between the dome and the flange was imposed without penetration and with a friction coefficient of 0.5. A tetrahedral solid curvature-based mesh was chosen, with 202760 elements and 317983 nodes.
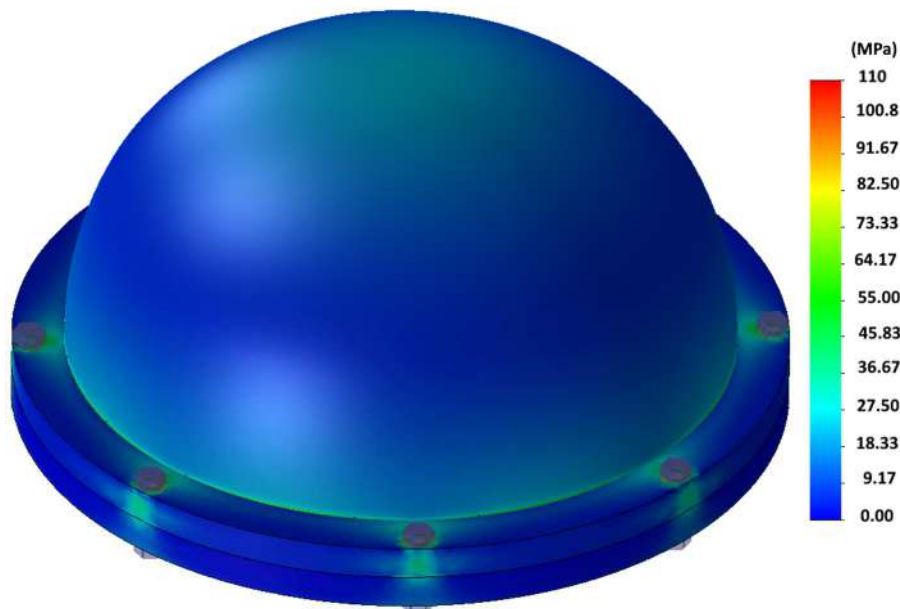

Figure 3.10:10-mm-thick Dome stresses [MPa] due to static pressure (1.45 MPa).

The minimum theoretical value between buckling and yielding collapse pressures are in bold and stress the type of break, and the result is the same as the experimental result. Specifically, the collapse occurs because of buckling up to a thickness of 5 mm;

beyond this thickness, the collapse is due to yielding. The most significant comparisons of breakage examples are qualitatively reported, and the experimental and FEM results match [120]. In Figure 3.11, the intermediate (6 mm thick) domes broke in the lowest part because of the yielding phenomenon.
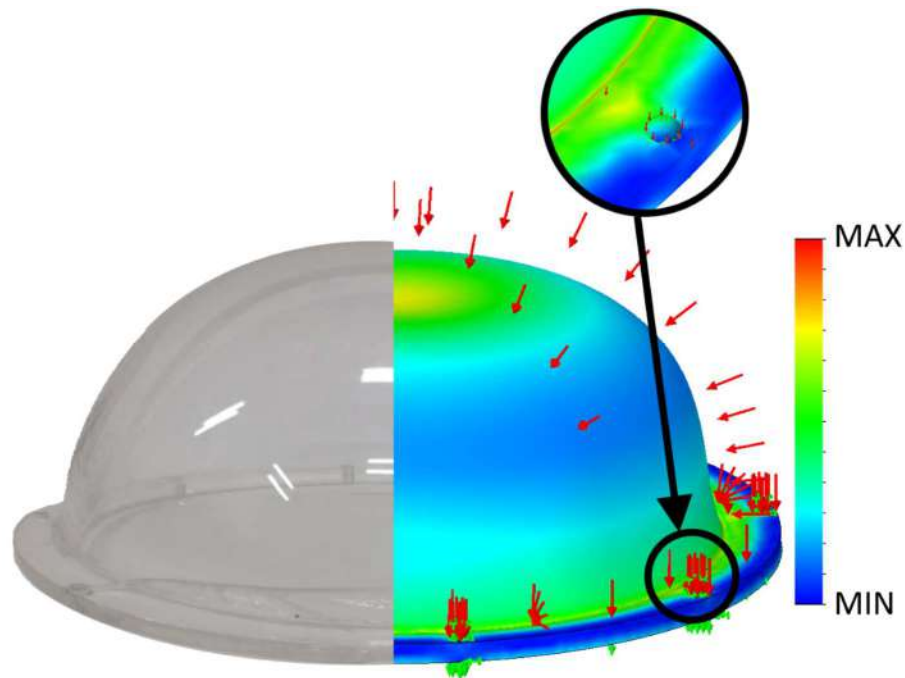

Figure 3.11: Comparison of compression ruptures.

In Figure 3.12, the thinnest (3 mm thick) domes broke because of membrane buckling in the highest region.
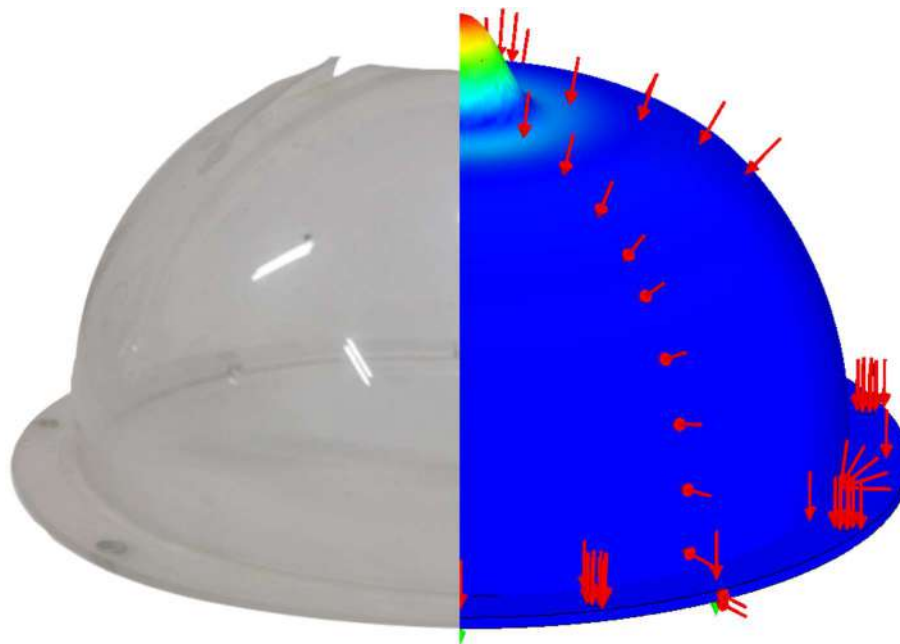

Figure 3.12: Comparison of buckling collapses.

The first eight buckling modes of the 5-mm-thick dome are shown in the Figure 3.13 and Figure 3.14, (DS = 25).

56
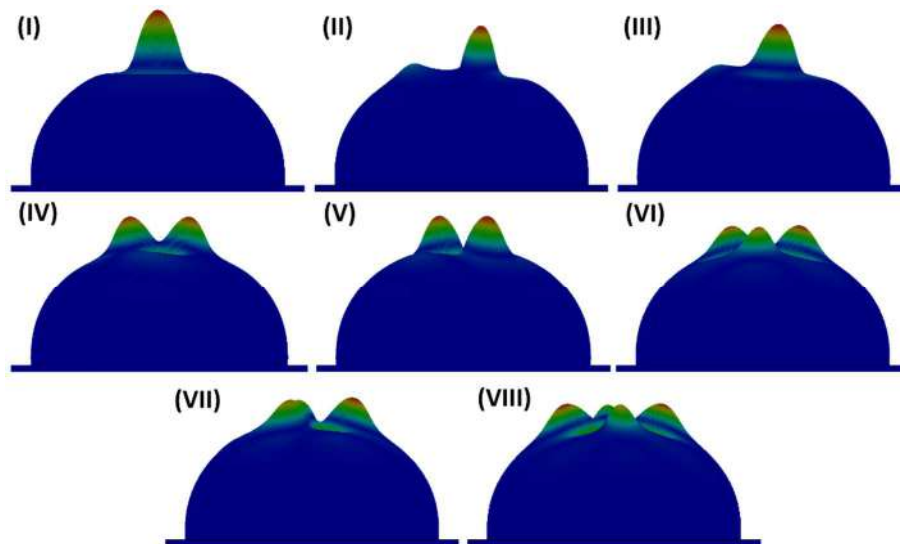
Figure 3.13: First buckling mode shape, (dome lateral view, DS = 25).
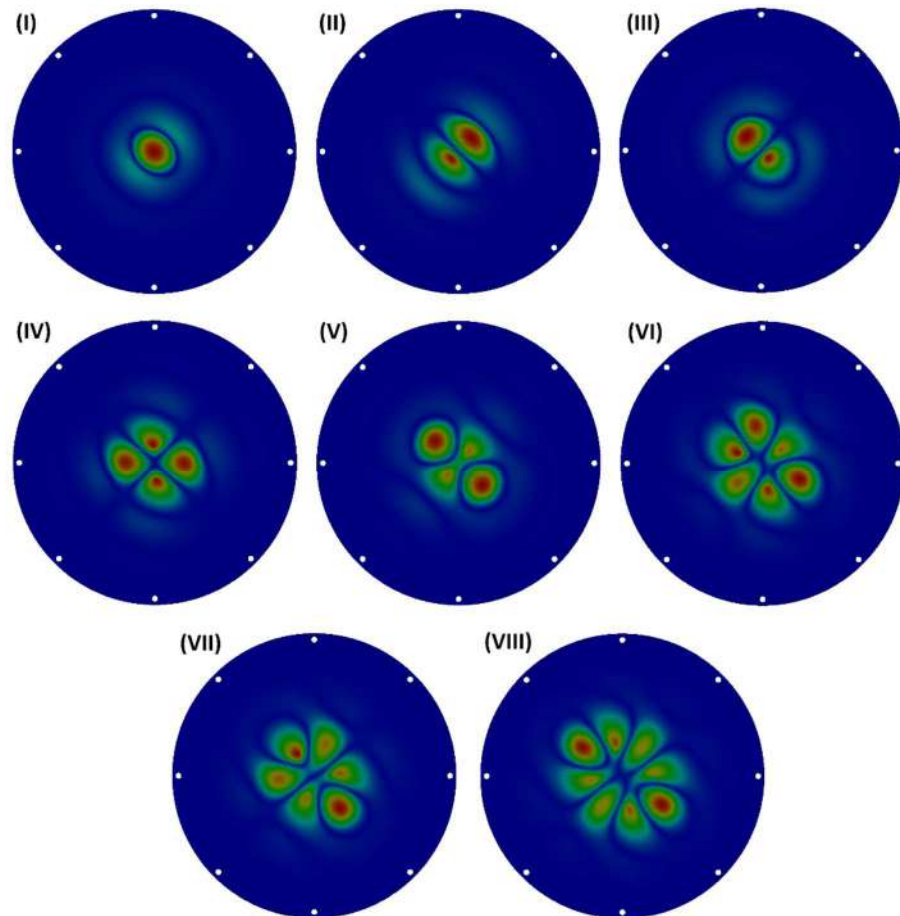
Figure 3.14: First buckling mode shape, (dome top view, DS = 25).

Notably, both the real and the simulated domes are not perfectly hemispherical. With this corrected shape, simulations can be used to predict the real breaking position, as well as the collapse pressure. This characteristic depends directly on the thermoforming process. Moreover, the *AR* factor and radius of the curvature are very

important for numerically reproducing its behaviour. In Figure 3.15, on the left, the real dome is shown, while on the right its design chart. CAD section in Figure 3.16.
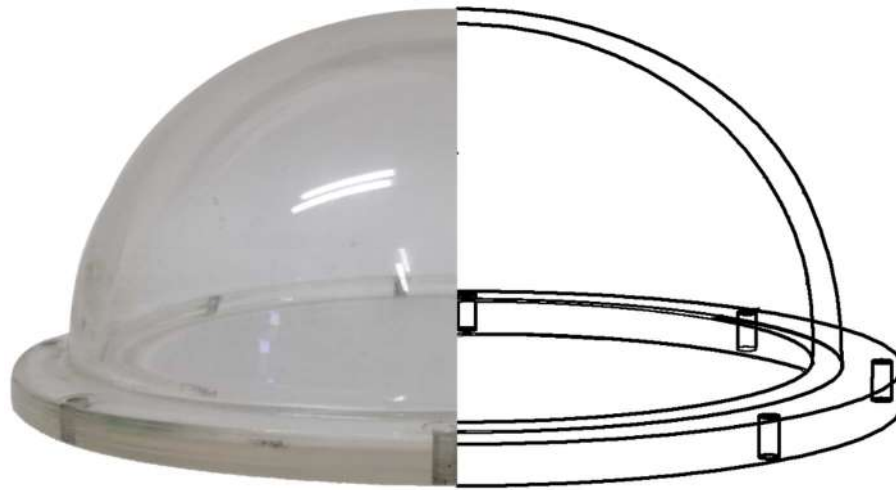
Figure 3.15: Comparison of geometries.
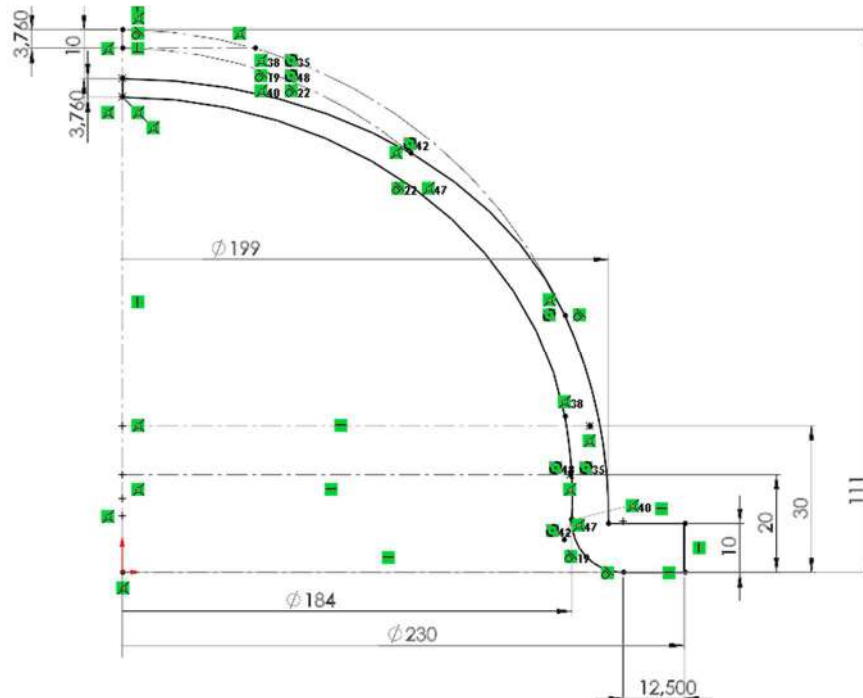
Figure 3.16: Designed geometry.

The FEM results reliably reproduce the experimental data; in Figure 3.17 green diamonds stand for the experimental values, while the purple dots represent the FEM yielding collapse and the orange dots reproduce the FEM buckling collapse; the theoretical values, after the here proposed corrections are applied, deviate by less than a 1 percent from the blue interpolating curve at most, except for an about 5 percent for the 3 mm thick dome. As mentioned, the trend of the pressure to the increase of the thickness (bluish line) is sublinear, this because of the onset of a second phenomenon, called overturning, too. To briefly mention this happening, FEM results are collected below: Figure 3.18 and Figure 3.19 show, at a pressure

immediately before the collapse, the displacements for the 10-mm-thick dome, (DS 25); in transparency the not deformed dome.

Figure 3.17: Chart for FEM and experimental collapse pressure.
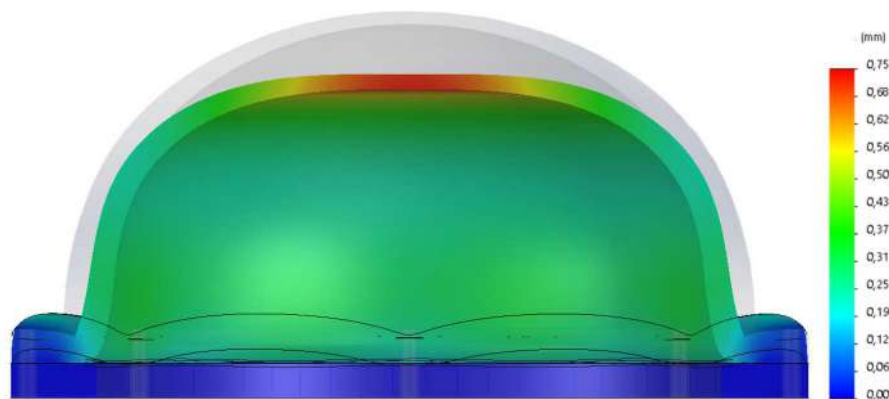
Figure 3.18: 10-mm-thick dome, displacements section view.
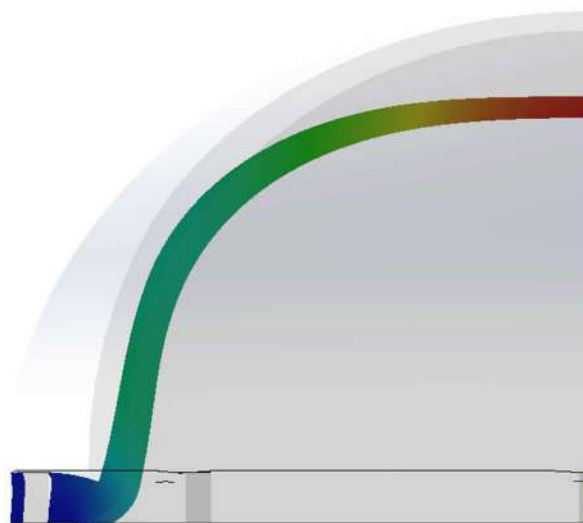
Figure 3.19: Overturning phenomenon.

59

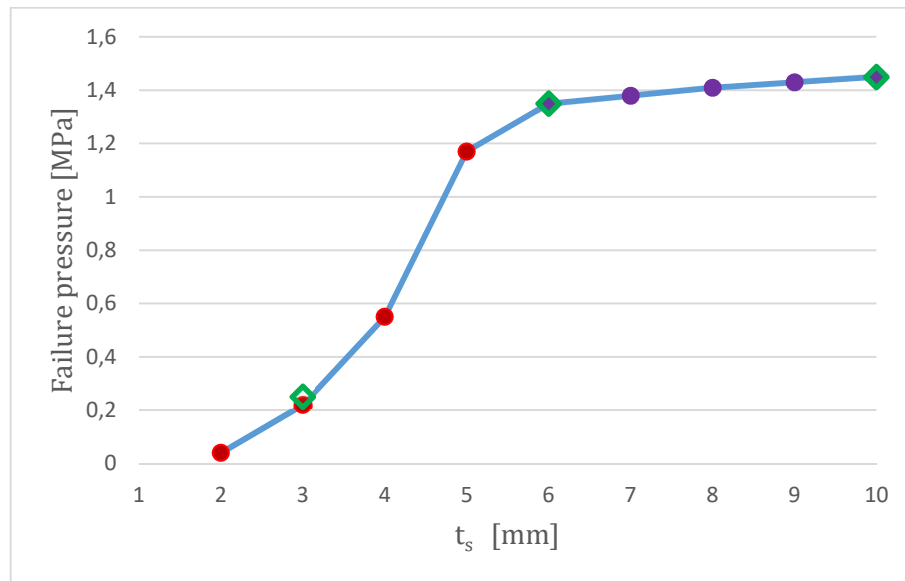In the end, given the reported correlations, the vehicle FeelHippo AUV has been equipped with a 10-mm-thick dome. The vehicle is thus able to reach a depth of 30 m safely (the less resistant structural component is the PMMA cylinder). To conclude, the model sensitivity to the variation of some dome geometric values has been checked, e.g. the AR and the nominal thickness (t_s), in a small range, starting from the near-transition geometry (thickness between 5 or 6 mm, the orange arises from the 5-mm-thick geometry, the grey from the 6 mm one). In Figure 3.20 the graph shows two interpolation curves representative of the failure pressure at the variation of the AR. The predominant phenomenon still remains the original one (buckling for $t_s = 5$, yielding for $t_s = 6$). In Figure 3.21 the graph shows the failure pressure only with respect to the thickness variation; the pressure trend follows the curve with the reference values, maintaining the same failure, as before.

Figure 3.20: Failure pressure with respect to AR variation.

Figure 3.21: Failure pressure with respect to t_s variation.

3.4. <u>Conclusions</u>

One of the most used geometries in underwater applications is the hemisphere; the here specific study concerns the thermoformed flanged dome. Since the studies in the technical literature do not well fit this case, the main issue was to adapt the classical formulations to calculate the critical pressure for the specific case under study. Two characteristics have 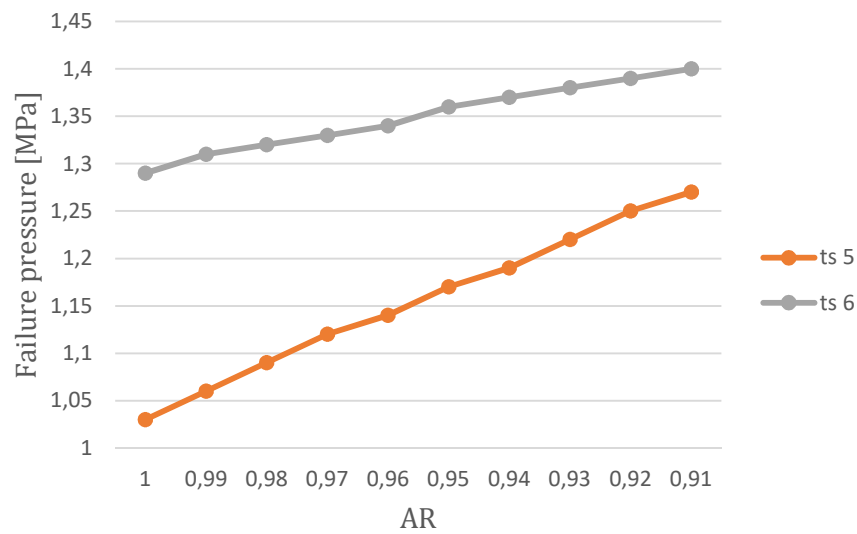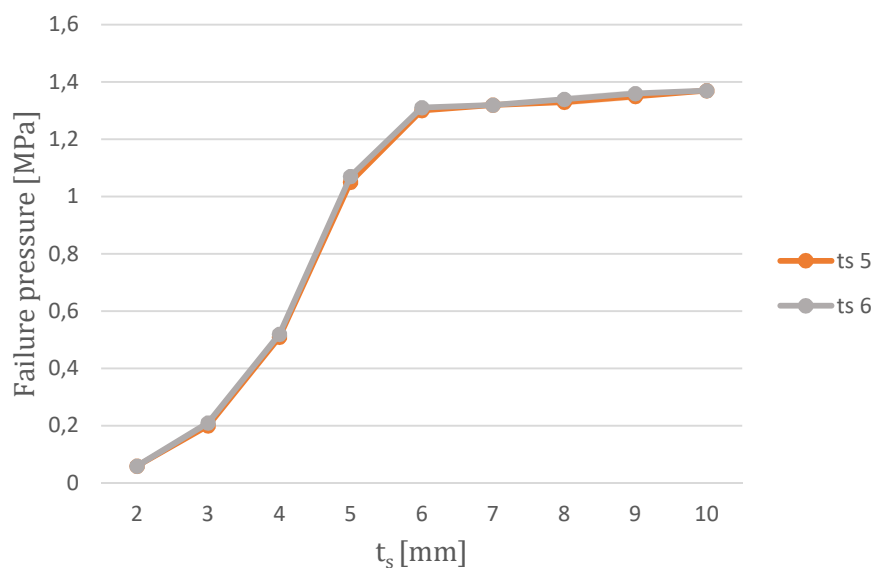been addressed: the first one is linked to the production process, as the free thermoforming leads to a variable thickness along the dome profile; the second one is related to the need of bind it to the rest of the structure, the cylindrical body of the vehicle, and the presence of a flange on which to tighten the screws. The final objective was to derive a mathematical tool that would allow, from geometric data, to derive the breaking pressure and identify the way of collapse.

To answer these research questions, first of all an experimental campaign has been carried out. What it has been obtained, leading to the breakage of the specimens in the pressure chamber, is a small, and actually specific, dataset of values and the awareness that the dome can break in two ways, or rather for two causes: buckling or yielding. The buckling phenomenon, predominant in the fine-thickness dome, occurs at the top of the shape, while the yielding, which happens for thicker domes, manifests at the base, near the flange. Starting from the two theoretical critical pressure studies, one for each way of failure, the main contribution was to introduce the variation in thickness, the aspect ratio and to evaluate a specific global correction coefficient for the constraint, to fit the experimental data. In addition, to validate the model, a FEM analysis has been performed on a corrected shape; the simulations, taking into account the thickness and the constraint, reproduce the experimental data and provide values for the intermediate thicknesses. Finally, the model sensitivity to the variation of aspect ratio and thickness has been checked. A lean and effective design method to identify the mechanical resistance of the dome has been thus proposed. The satisfactory obtained results highlight the goodness of the derived solutions. However, many improvements could be made: for example, some possible future developments are related to the identification and evaluation of application-specific coefficients for individual thickness variation, different constraint (perhaps even by changing the geometry and arranging axial screws or a flange of different shape), diverse manufacturing process (for example by simply adding a countermould or by completely changing technology, here an example of fabrication through coating [144]), and thus material. It would also be useful, keeping the production method and the type of constraint unchanged, to test specimens of different sizes and thicknesses. This would require a much more extensive experimental campaign to separately study each of the different coefficients and to generalise their field of application in a parametric way.

Chapter 4

4. *Buoy: design and development*

Problems with the use of autonomous submarine vehicles arise when it is necessary to perform a diving mission. The issues mainly concern the possibility of establishing a communication with them in order to instantly know their position, to receive data from the vehicle or to be able to give them a specific command. The main communication and location networks between operator and vehicle are GPS, radio or Wi-Fi. These communication channels are very efficient as long as the vehicle remains emerged from the free surface of the water [145]; however, once immersed, the radio waves are absorbed by the water and for this reason a few centimetres under the surface the communication with the vehicle, through these channels, is ineffective [82]. Therefore, the only way to establish effective communication between the vehicle and the control system is to use technologies that adopt sound waves. In addition, the dual functionality of integrated acoustic communication and navigation allows a reduction of costs, size, power and potential acoustic interference [146]. Thanks also to the development of GPS technology, new underwater acoustic positioning systems based on equipped buoys have emerged with GPS receivers and acoustic communication capabilities [147]. A detailed summary of the main acoustic positioning systems is collected in [78], in particular the details of LBL and USBL systems are given below. The LBL system is characterized by a Baseline length of 100 m up to 6000 m, and obtains the positions relative to an array of transponders distributed on the seabed. Looking at the advantages of this solution, it shows a high accuracy of the obtained position, regardless of the water depth, but it requires expensive and time consuming equipment. On the other hand, the USBL system has a Baseline length of less than 10 cm, exploiting a multi-element transducer. Among the benefits, the USLB is an easy tool to use and it does not need a greed deployment on the seafloor; however, a calibration system is required, the absolute position accuracy depends on the additional sensors available on the support structure and on the relative position. This is the system that has been chosen to be implemented for the localization and communication among the UniFI vehicles, both for economic reasons and for the versatility of use. To point out, the USBL is an acoustic localization and communication tool based on the principle of propagation of a sound wave in water. An acoustic pulse is emitted by the transceiver and detected by the submarine transponder, which in turn responds with an acoustic signal. The time elapsed between the transmission of the initial acoustic impulse and the response signal is measured by the USBL system and thanks to the TDOA (Time Difference Of Arrival), knowing the speed of the sound in water, the system it is able to calculate the distance and the relative azimuth angle using an array of 4 sensors.

To know the absolute position of the AUV, it is therefore necessary to have a known absolute reference system and it is preferable to reduce the relative distance between the target, e.g. an acoustic modem on the AUV, and the USBL device. It is precisely for this reason that the objective of achieving a system that could create a movable and

sensored bridge between operator and submerged vehicle was born, Figure 4.1. Equipping the buoy with an IMU and USBL system allows communication and localization of submarine vehicles, equipping it with GPS system, Wi-Fi and radio allows communication with the user [148].
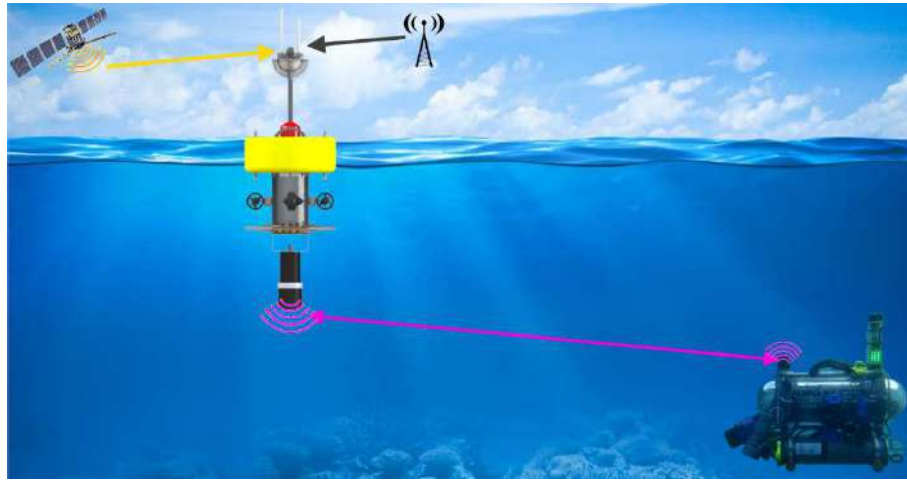

Figure 4.1: Communication scheme, buoy-FeelHippo AUV system.

In this way it is possible to know the real time vehicle position during the diving and to establish with it a communication channel. The operator can then monitor the progress of the mission, give new commands not included in the original mission profile or end the mission earlier than expected. Another great advantage is that, being able to monitor the position of the vehicle, if the vehicle suffers a fault and therefore be unable to re-emerge, the recovery operations will be facilitated by the knowledge of the last position detected by the USBL. A first version of the buoy was presented in [79]; one of the major cons concerned the lack of a fixed connection between USBL and structure; in addition to implementing a constructive solution to meet this need, the navigation capacity has been increased by the use of 4 motors. The full control over the 3 DOFs is useful both to maintain a fixed position, if required, and to follow the target, to reduce the relative distance, deviating from a preferential direction. The candidate's contribution has been the electromechanical design of the new buoy; this study has been also based on the acquired knowledge on buckling, but it has been focused on topological optimization techniques.

This chapter is organized as follows: Section 4.1 presents the buoy main features and the system architecture; in Section 4.2 the mechanical design of some parts is given: the antenna assembly, the float, the propulsion system and ballast; Section 4.3 briefly illustrates the cylinder collapse study; Section 4.4 focuses on the handle system and its optimization. In the last section, 4.5, there are some images of the buoy depicted during the first tests.

4.1. Buoy main features and architecture

In accordance with the specifications identified by the research group (maximum weight in air about 40 kg, less than 1.5 m long in the handling configuration and with one working day of autonomy), based also on previous experience [79], the here presented buoy has been designed as a portable, low cost floating device able to give

support during all the phases of a typical underwater mission; and that is why the buoy is customizable with different payloads, without changing its buoyancy (thanks to custom-made weights). Starting from a previous basic floating motor-powered device [149], this new model of buoy introduces, among all benefits, a fixed connection between the USBL and the floating structure, it increases the number of thrusters, it guarantees a watertight area for the electronics and an improved stability. The main scope of the USBL-aided buoy is to compensate for the lack of GPS underwater, creating an acoustic bridge with, for instance, FeelHippo AUV [150]. In Figure 4.2 a frontal view of the buoy is given together with some of the main parts of its structure: antenna area (b), main electronics housing (c), propulsion system (d), and acoustic payload (e).
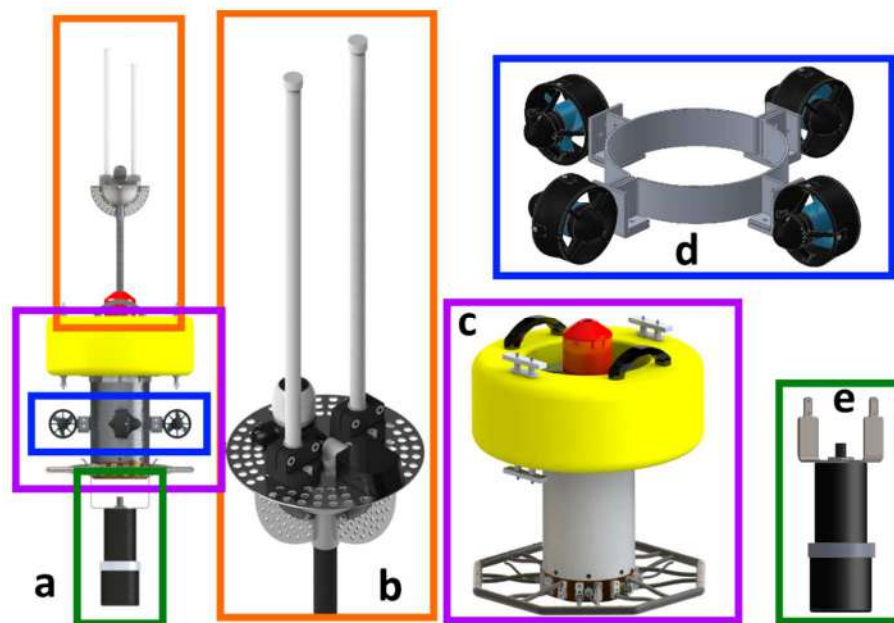
Figure 4.2: CAD of the autonomous buoy (a) divided into its main parts.

Its external overall dimensions are about 1.4 m high without the payload, 1 m holding the payload but removing antennas (two possible shipping or transport solutions), 0.5 m wide; it is quite small and easily transportable by two people thanks to dedicated handles. The buoy could be deployed from both a pier and a small boat with limited effort; it weights in air around 37 kg, in its complete configuration. To summarize, the main features are collected in Table 4.1.

Table 4.1: Buoy main features.

Type of vehicle	ASV
Material	Aluminium, carbon fibre, stainless steel, PVC
Dimensions	1810x535x535 mm
Weight	37 kg, full configuration
Number of motors	4
Cruise speed	0.6 kn
Autonomy	12 h
Power supply	22.2 V

Some more considerations: four marine propellers [121], in vectored configuration, are at the same height of its centre of gravity, thanks to the movable thrusters support, and fully control the buoy in each of its 3 DOFs: yaw, surge and sway [122]. Regarding the flexibility, the buoy was created to support acoustic devices dedicated to the underwater localization, particularly to move the USBL by EvoLogics (S2CR 13/34 kHz) in a controlled manner, but thanks to spare connectors, it is possible to equip the buoy with other devices, e.g. cameras or sensors to monitor or measure pollution, salinity, etc. The buoy is thought to face a sea state 1, but its stability has been numerically tested for a wind up to 30 kn [151]. The watertight electronics module is a cylinder in Aluminium (Anticorodal type 6082 T6), theoretically tested to yielding and buckling collapse [152] (in case of an accidental sinking), and holds, among all: 1 main computer (x86 ULTRA by UDOO), 1 radio modem (868+ by RFD), 1 Wi-Fi (PicoStation M2-HP by Ubiquiti), 1 Micro Maestro 6-channel USB servo controller by Pololu, 1 IMU MEMS (MTi-G by Xsens) and 1 GPS (NEO 7P Evolution Kit by Ublox). The chosen models depend on the availability in lab of the specific component, but with small modifications to the internal plates it is easy to replace and update them.

The antenna subassembly provides Wi-Fi and radio communication and allows the buoy control from a remote station, when remotely operated. Furthermore, the GPS allows a good localization of the buoy. Lastly, an anchor light guarantees visibility to the float. The radar plate, on which these devices are located, is connected to the buoy thanks to a carbon tube. The yellow floating body, crossed by handles and bollards, ensures the buoyancy even in case of complete flooding of the main housing; it is made of closed-cells PVC (PolyVinyl Chloride) foam. A custom lead weight guarantees the buoy stability (tuning the distance between the centre of buoyancy and gravity).

In addition to the electromagnetic waves on the airside and the acoustic waves on the waterside, another way of communication is the use of two umbilical cables, one dry, one wet; the buoy onboard software is based on ROS (Robot Operating System) [153] and it allows planning and executing autonomous missions.

Keeping in consideration the needed and selected devices, the first part of the design process has consisted in the identification of suitable electrical connections. These connections, among all the onboard devices, are highlighted here below. In particular, in Figure 4.3, each coloured line represents a different connection: blue reproduces the Ethernet wiring, black the USB, red for servo command and brown is for the UART conversion.

For what concerns the needed energy supply, a consumption evaluation has been done. Considering a cruise nominal speed of 0.6 kn, the estimated drag leads to an average power consumption of about 40 W; furthermore the other vital functions have been considered (e.g. anchor light 2 W, Wi-Fi 7 W, Ethernet switch 3W, radio 4 W, main vital PC 6 W, USBL 18 W, etc.). The battery pack, which guarantees an autonomy of about 12 hours, consists of 2 LiPo Tattu Plus 22000 mAh 22.2 V. Since this nominal supply voltage, a TRACO POWER DC/DC has been introduced; in Figure 4.4, all the voltage values are given.
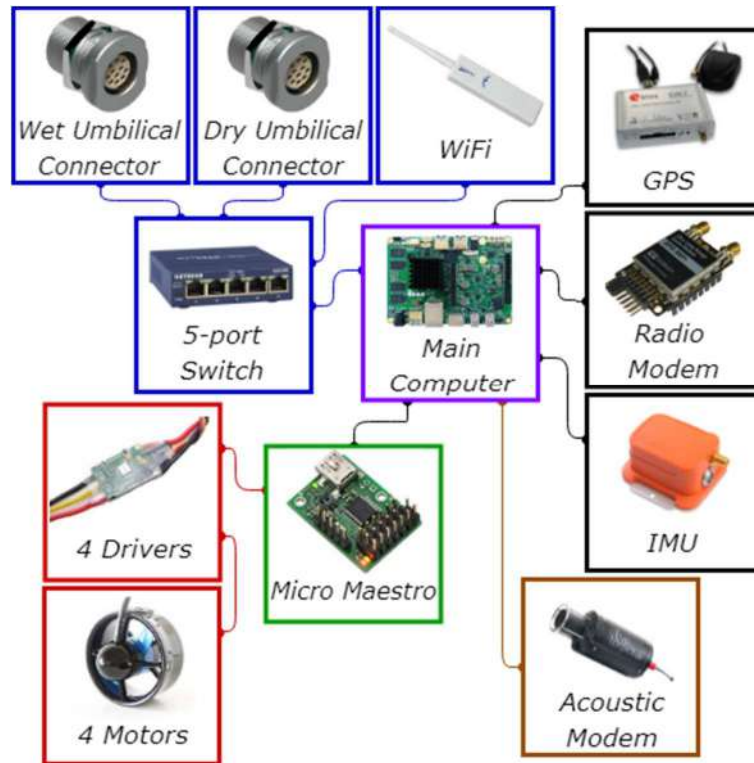
Figure 4.3: Onboard device wiring.

Figure 4.4: Power supply scheme.

Focusing on the inner distribution of these components, to better guarantee the buoy stability and to optimize the weight distribution, the battery pack has been centrally located. All the supports for the other devices were developed starting from an internal PMMA skeleton. A connectors zone has been created near the upper flange to tidy the connections. Only the drivers rack and the IMU are located directly on the lower flange; the first one for a heat exchange reason, the second one to be solid with the structure in general, with the USBL support in particular. In Figure 4.5 two views of the internal layout are shown, with evidence of the Ethernet switch and the Wi-Fi electronics on the left, the DC-DC board and main PC on the right. In addition to the PMMA plates, (white in figure) there are some metal L-shape connections and some custom ABS 3D printed components (the devices supports are here in red while the main support is in yellow). Almost all the seemingly empty space will be occupied by the wiring.
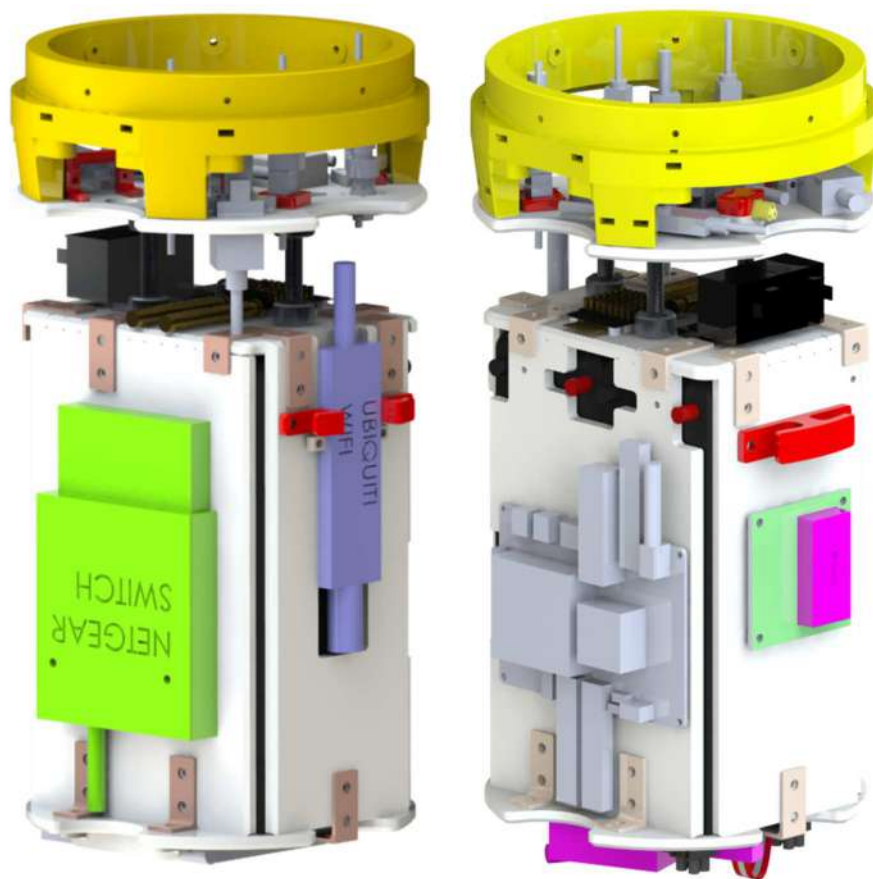
Figure 4.5: Electronics layout.

4.2. Buoy design

4.2.1. *Antenna assembly*

The antenna area, fundamental to communicate with the external world, is composed of radarable and reflective carbon plain plates, visible in Figure 4.6, drilled to minimize the wind lift but not too much to be still visible from the radar wavelength. In the presence of holes, in order to keep the plates visible to the radar, it is necessary to respect two constraints:
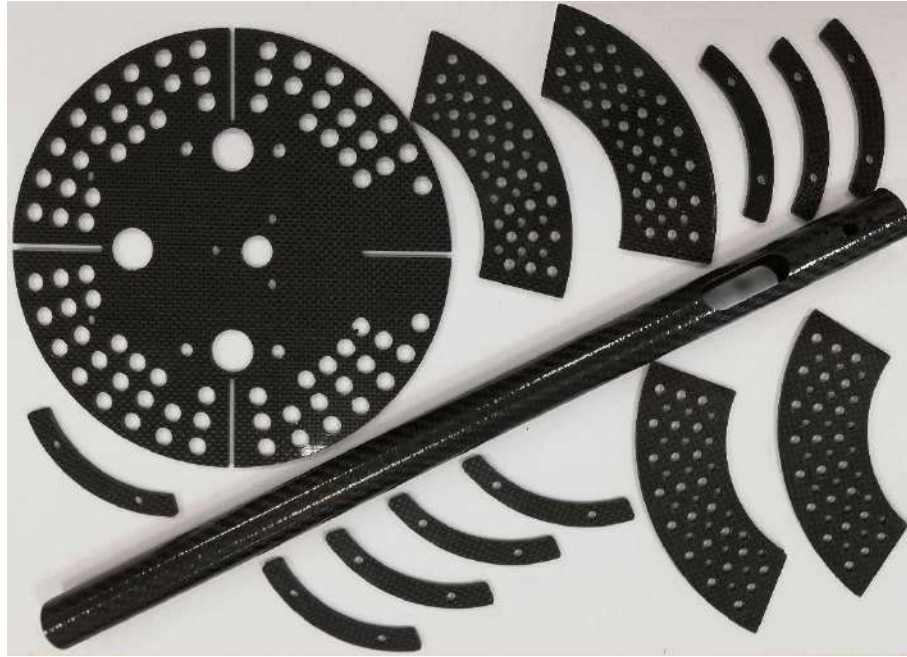
Figure 4.6: Carbon plates and tube.

the first is that the holes must have a minimum diameter smaller than the wavelength of the radar waves while the second is that the space between adjacent holes must be greater than the diameter of the holes chosen (the radar frequencies generally used fall between 8-12 GHz; considering the most binding condition at 12 GHz, a wavelength of 25 mm is obtained, which therefore represents the maximum acceptable size of the holes to maintain the radar system). On the main plate, the various antennas are located, close to the anchor light. All these parts are supported by a carbon twill tube (Figure 4.7).

Figure 4.7: Detail of the antenna body.

The inner diameter is necessary and sufficient to pass all the cables. The antenna area can be removed, thanks to a custom POM (PolyOxyMethylene) quick release system. To join the antenna parts together, a structural adhesive for carbon composite has been used (AS89.1/AW89.2). The small arches have been used to block plastic covers to protect the free wiring, by preventing the accidental direct access.

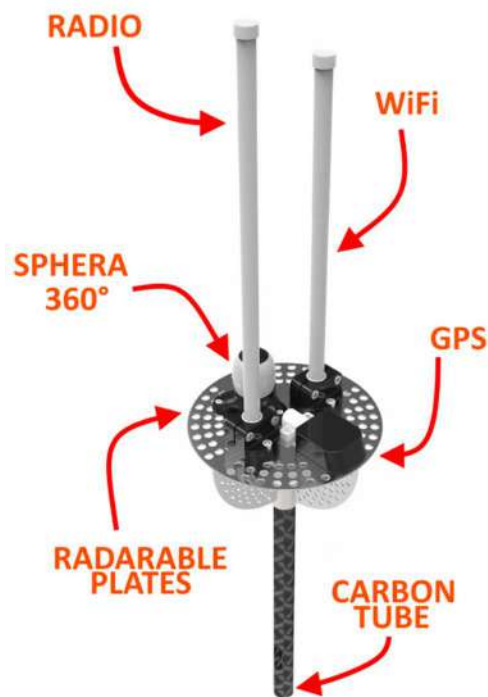To test the strength of the tube, two test cases have been considered, both representing the scenario in which the buoy is grasped from the upper part of the antenna area (equivalent to a fixed constraint) and not from the handles: the less heavy consists in subjecting the structure to an axial tensile load of 500 N to simulate the buoy weight, with a 30% of margin; the maximum resultant stresses (10.7 MPa) and displacements (0.01 mm) induced are acceptable (FEM results in Figure 4.8).
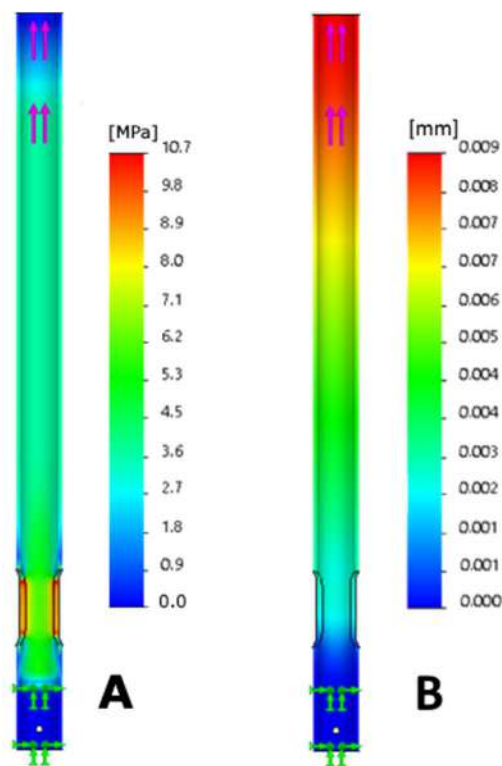
Figure 4.8: Stress (A) and displacements (B), antenna rod tensile test.

The second one imposes a bending load system, equivalent to 500 N, as before; the maximum resultant stresses and displacements, Figure 4.9, induced are still acceptable, remaining less than 500 MPa (respectively 322 MPa and 4.4 mm,). The displacements are reproduced together with the undeformed axis, the green arrows represent the constraint while the purple ones reproduce the applied force.
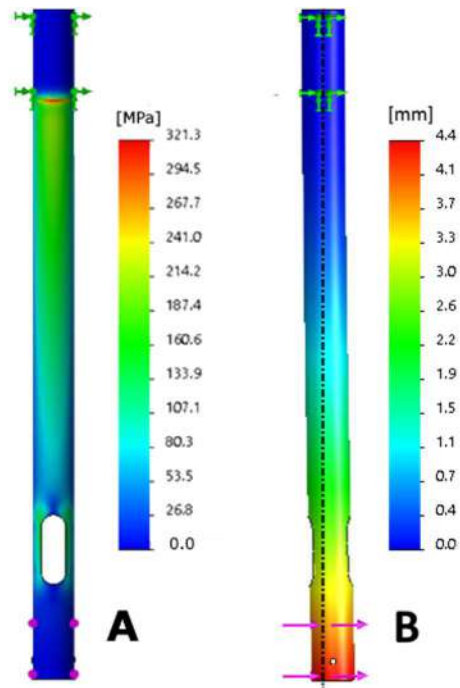
Figure 4.9: Stress (A) and displacements (B), antenna rod bending test.

4.2.2. *Floater*

This component guarantees the buoyancy even in case of complete flooding of the electronics housing, thanks to more than 6 L of residual thrust; it can be used as foothold in horizontal lay too. The chosen colour is yellow, quite common in underwater robotics, while the material is closed cells PVC M200 foam, with a density of 200 kg/m3 and good structural properties. Thanks to stainless steel threaded inserts pre-through hole, some bollards and two Boutet Handles EV (visible Figure 4.10) will be on board.

Figure 4.10: Floater rendering.

Overall, it is 195 mm high, its inner diameter is of 200 mm, and the external is 500 mm. In Figure 4.11, the violet line represents the waterline and both the centre of gravity and centre of buoyancy are depicted, in case of normal operation. H stands for the deadwork and it is 85 mm (about 10 L of floating thrust) while D is the distance between the centre of gravity and buoyancy, it is about 60 mm.
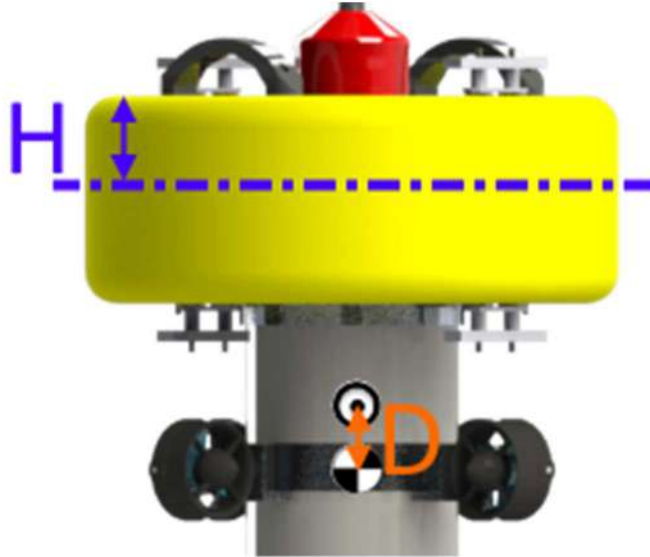
Figure 4.11: Waterline, centre of gravity and of buoyancy.

4.2.3. *Propulsion system*

The propulsion system is useful to navigate on surface, simplifying the deployment, and keep the buoy in a desired position, avoiding the presence of a mooring post. The propulsion, the slow moving, reaching and maintaining positions are guaranteed by 4 three-phase brushless motors, which allow the compensation for the change in position and can assure a dynamic position keeping on surface. The chosen thrusters are T200 by BlueRobotics and are located in horizontal vectored configuration to actively control the two translations and the yaw angle. To optimize the thrusts all the motors can be positioned at the centre of gravity height; in case of buoy configuration change, all the thrusters can be moved together thanks to an Al (Anticorodal type 6082 T6) clamp (Figure 4.12), circumferentially keyed to the cylinder.

Figure 4.12: Thrusters clamp.

4.2.4. _Ballast_

The dynamics and stability of a buoy depend mainly on the shapes, masses and positions of the components of which it is made. The objective is to have the buoy in a stable state of equilibrium so that even if an external force causes a change in its position, the buoy quickly returns to its unperturbed position. The stable equilibrium condition is guaranteed if the centre of gravity, where the weight force is applied, is below the centre of buoyancy, where the buoyant forces acts. When only these two forces are applied, a floating body tends to rotate with respect to its centre of mass under the action of a couple. On the lower face of the lower flange some threaded holes allow the placement of custom lead plates (Figure 4.13), with the function of increasing or keeping the stability in case of configuration changes and the distance between the centre of gravity and centre of buoyancy; an angle of about 6° till 30 kn of wind is guaranteed (Figure 4.14) (in order to calculate the external torque acting on the buoy, the SOLIDWORKS Flow Simulation solver was used to model the action of the wind acting on the emerged part of the buoy).
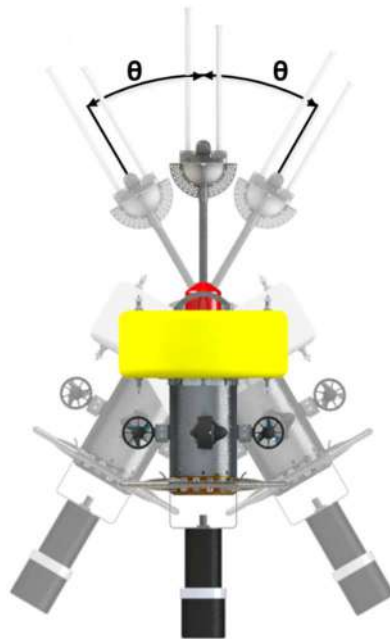

Figure 4.13: Lower lead ballast.

Figure 4.14: Oscillation angle representation.

4.3.<u>Main housing</u>

The electronics housing, protects in a watertight cylindrical case all the devices; As many other parts of the buoy, it is in Anticorodal type 6082 T6 aluminium alloy, with hard anodization against corrosion, which is a good compromise between weight and strength. The tightness of the watertight compartment is ensured through two Orings in NBR 70 Shore A, located between each flange and the cylindrical tube, visible in Figure 4.15. On the upper face, there is the predisposition for a vacuum nozzle, useful for the disassembly and to check the absence of leakage; furthermore, there are some Fischer connectors, Core Series Brass, useful for the recharging, the umbilical connection and antennas, dry air side. On the lower flange, wet sea side, on the lateral flats there are some cable glands (by Pflitsch Blueglobe) and connectors (by Seacon) for other connections together with another umbilical port.

Figure 4.15: Upper flange.

In case of watertight sinking and without considering other less efficient components two different collapses have been investigated, to evaluate the possibility of recovery.

An external pressure has been circumferentially applied to the cylinder together with the equivalent axial load. A tetrahedral solid curvature-based mesh was chosen, with 3248723 elements and 4874029 nodes. For the instability study, both ends are interlocked in a precautionary manner, not considering the axial DOF. $P_{crit} \cong 11$ MPa: the BFS is about 1 (0.985). The number of lobes, associated to the first buckling mode are 3; the deformation is depicted, with a DS of 100, in Figure 4.16 and Figure 4.17. $P_{design} \cong 5$ MPa.
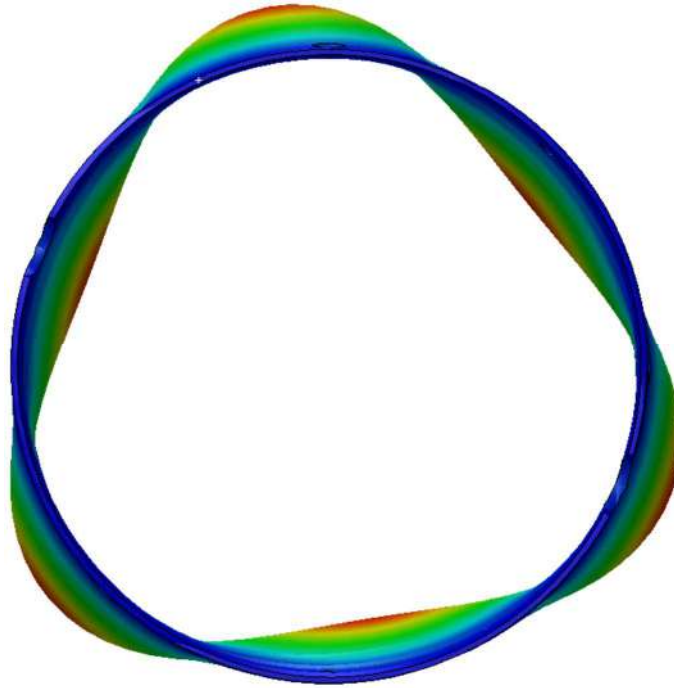
Figure 4.16: Buckling results, (cylinder frontal view).
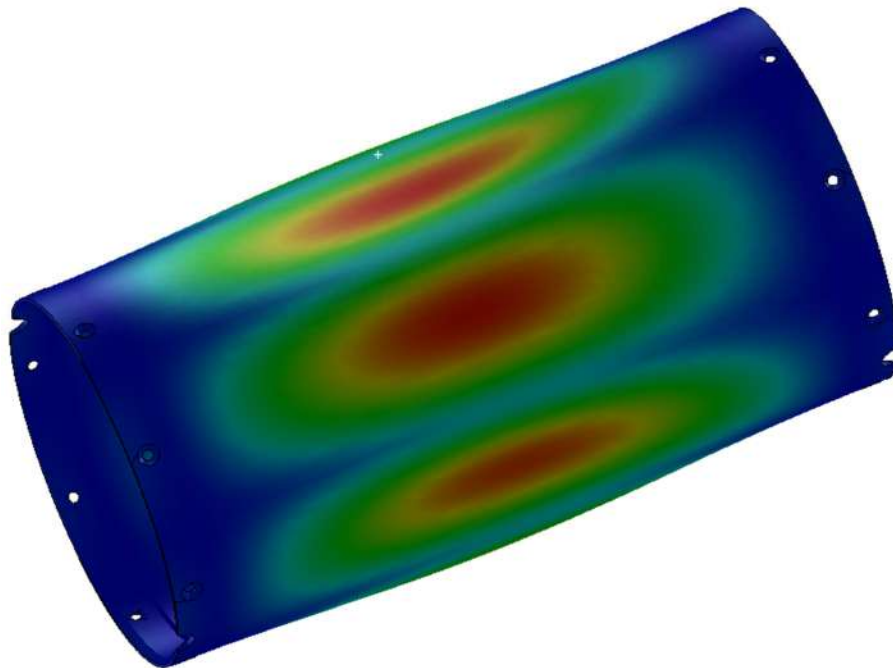
Figure 4.17: Buckling results, (cylinder perspective view).

For the static analysis one end is interlocked, while on the other end an equivalent inner pressure has been applied to simulate the joint with the flange, leaving the axial DOF. The plastic deformations occur at a lower pressure, of about 5 MPa, only in the constraints area, leading to the possible consequent flooding of the compartment. FEM results follow: stresses are shown in Figure 4.18, the 0.1% of the material is over the yield strength.

Figure 4.18: Static analysis results, stresses; (cylinder lateral view).

4.4. Handle system optimization

The last component is the big main handle, which has more functions: to contribute as ballast, to protect the propulsion system and the main housing, to guarantee a handhold during transport and a foothold in horizontal configuration. For the last reason an external octagonal shape has been chosen. In order to identify how to draw the structural part of the handle, a topological optimization was carried out using two different softwares: SOLIDWORKS and Altair Inspire™.

Beginning from the first one, a starting geometry has been created (Figure 4.19): to let the handle subject the aforementioned functions, the outer octagon is circumscribed to a circumference of 500 mm diameter, the inner one to 191 mm (imposed by the smoothed flange).
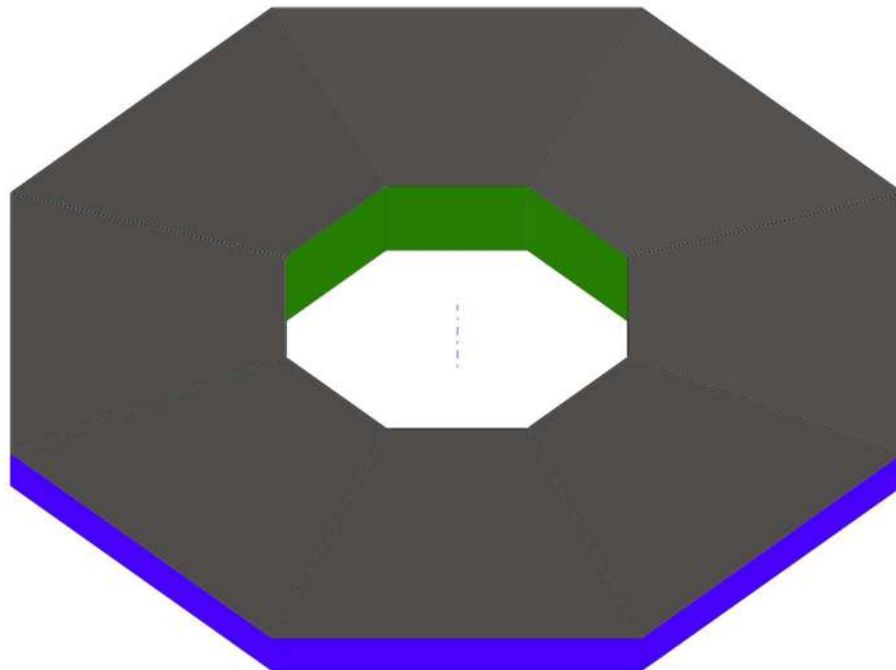
Figure 4.19: Maximum size model, starting geometry.

The green and blue areas are preserved regions, parts of the model excluded from the

optimization process and preserved in the final shape; on the first one the constraint has been applied while on the second one an axial distributed load has been imposed. The grey volume is the design space.

The optimization objective is the best stiffness to weight ratio. After several simulations a topology study has been obtained, and the related results are collected below. In Figure 4.20 there is the coloured scale explicative for all the SOLIDWORKS results, yellow stands for the mass which must be kept and constitute the optimized structure, blue for the removable mass.
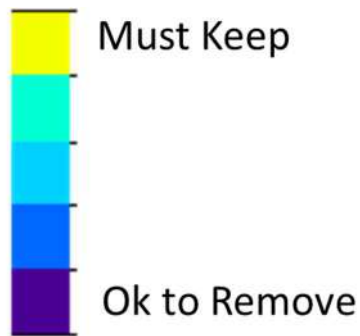
Figure 4.20: Coloured scale result.

In Figure 4.21, a top view of the result is shown, and it seems a sunburst; in Figure 4.22 an enlarged detail of one of the rays, a vacuum inner volume has been highlighted; lastly, a middle section is depicted in Figure 4.23.
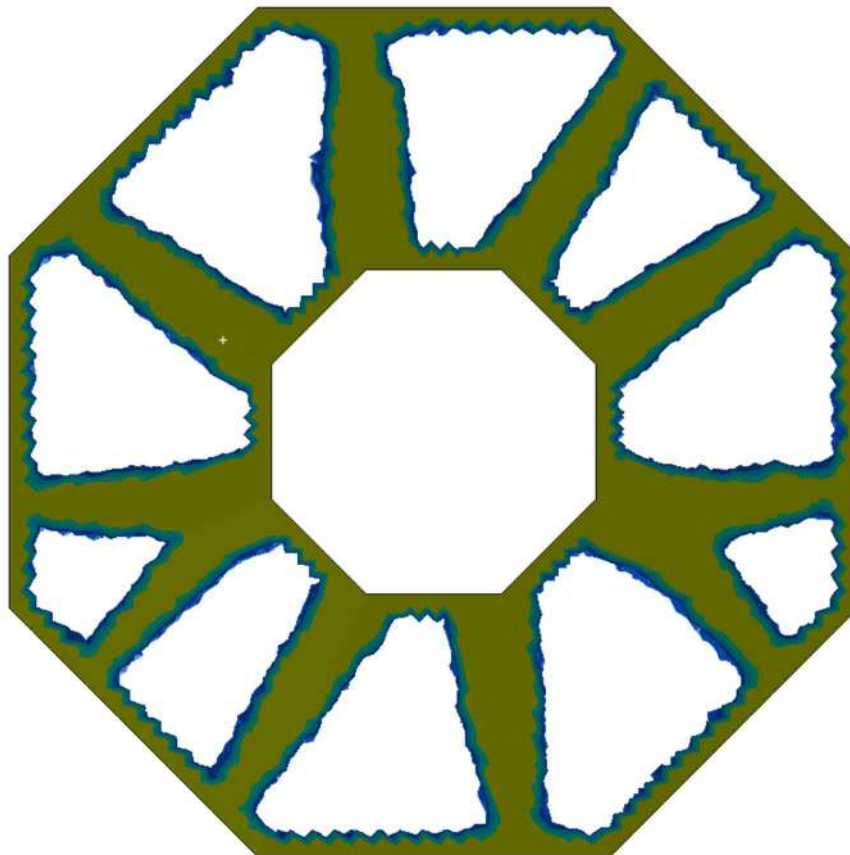
Figure 4.21: First optimized result, top view.
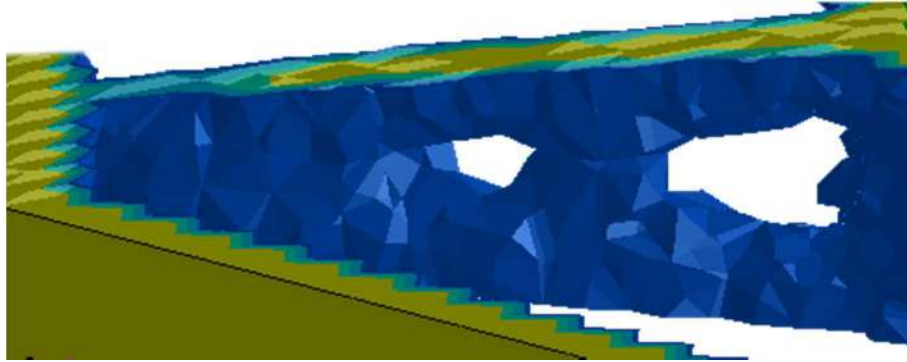
Figure 4.22: First optimized result, lateral view.
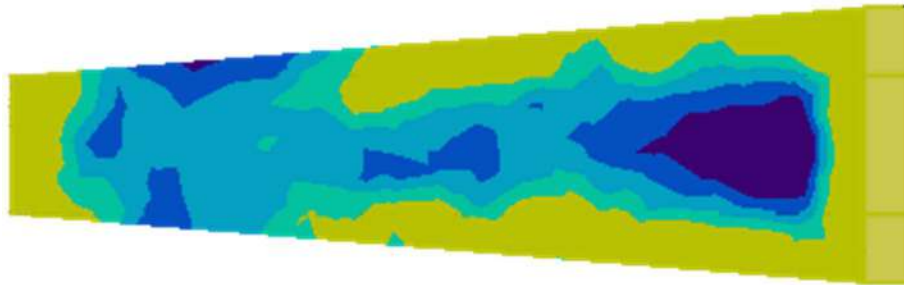
Figure 4.23: First optimized result, middle section.

Although it gives an idea of the final geometry, one of the limitations of this tool is the lack of mesh management, which is not symmetrically generated; therefore, while giving information on how the single branch should be, the second software, more limiting for the management of constraints but better for the discretization, has been used. First of all, a new starting geometry has been created, the grey parts of volume constitute the non-design space, while the brownish one represents the design space (Figure 4.24 and Figure 4.25).
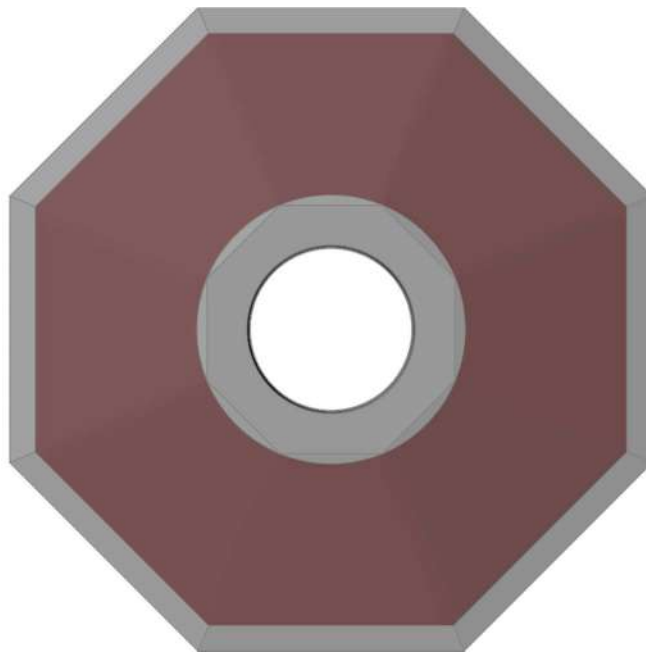
Figure 4.24: Design and non-design space, top view.

Figure 4.25: Design and non-design space, lateral view.

To use the available constraints and connect the inner part to the fixed flange, a circular part has been included. On the external vertical faces two different boundary conditions have been applied: first a single axial load (1000 N), secondly a double axial load, one positive, one negative, to simulate the lift of the buoy at about 3g per side. The symmetrical mesh dimension range chosen is 0.76 – 3.8 mm. A minimum safety coefficient of 1.2 together with a minimum thickness of 25 mm has been imposed, in order to then be able to weld the component. The optimization results follow.

In Figure 4.26 and Figure 4.27 two views of the first test case are shown, with axial load in a single direction. A symmetrical central sunburst has been obtained.

Figure 4.26: Optimized geometry, middle section, first test case.
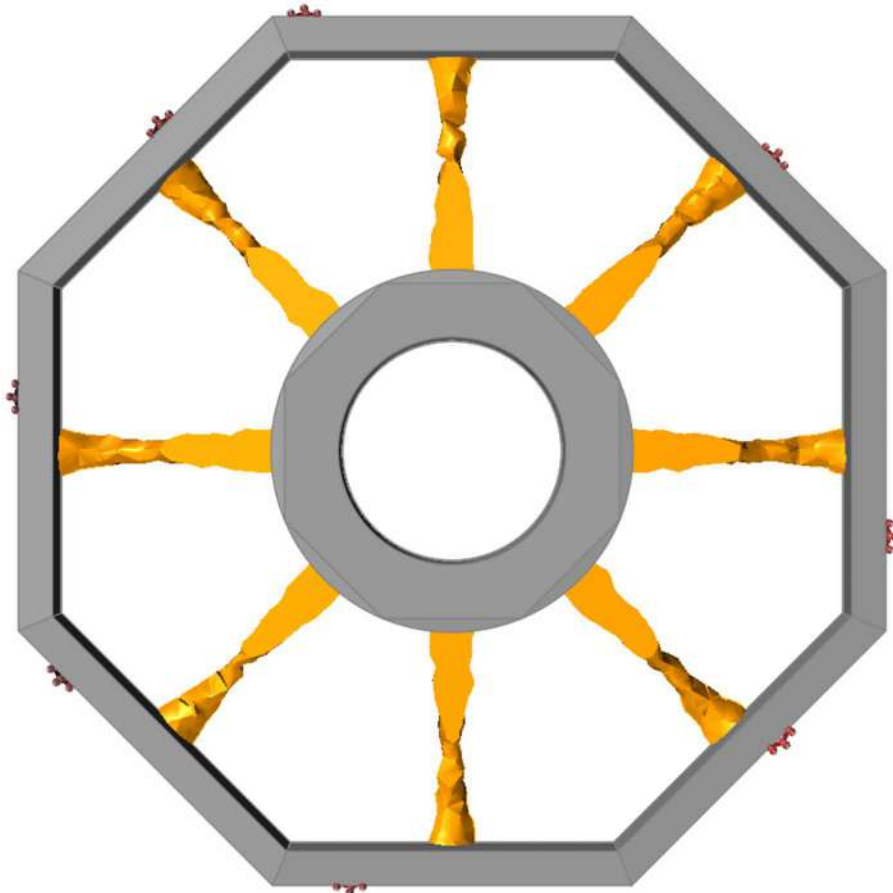
Figure 4.27: Optimized geometry, top view, first test case.

To complete the study, in Figure 4.28 and Figure 4.29 other two views of the complete load configuration are depicted.

Figure 4.28: Optimized geometry, middle section, second test case.
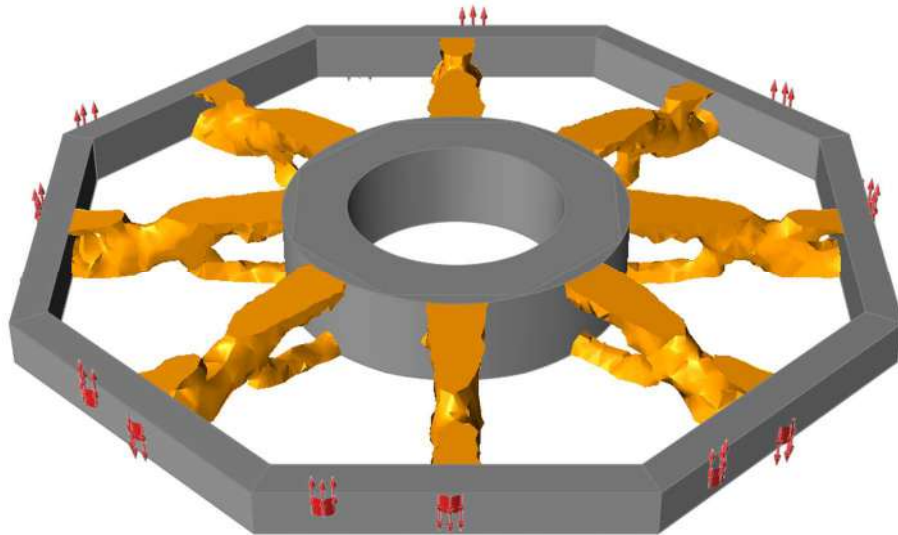
Figure 4.29: Optimized geometry, perspective view, second test case.

Starting from the topological optimization results the octagonal external tube has been linked to the lower flange through double waved spokes (Figure 4.30) and custom plates (the latter shape has been dictated by the mounting of wet connectors.
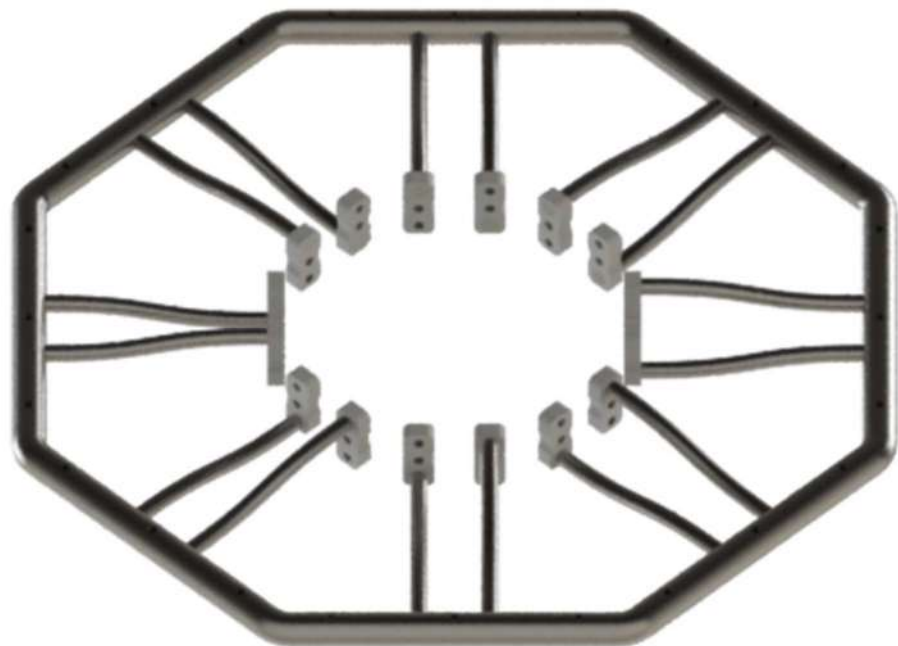
Figure 4.30: Handle rendering.

To simulate the handle system, a fixed constraint has been imposed between the little plates and the lower flange; the applied force is a 1000 N axial force, locally applied at the external part, equivalent to the case in which the buoy is lifted at about 3g.

In Figure 4.31 the maximum stress is of 250 MPa, close to the flange, while the maximum displacement, on the external geometry, is less than 0.7 mm.
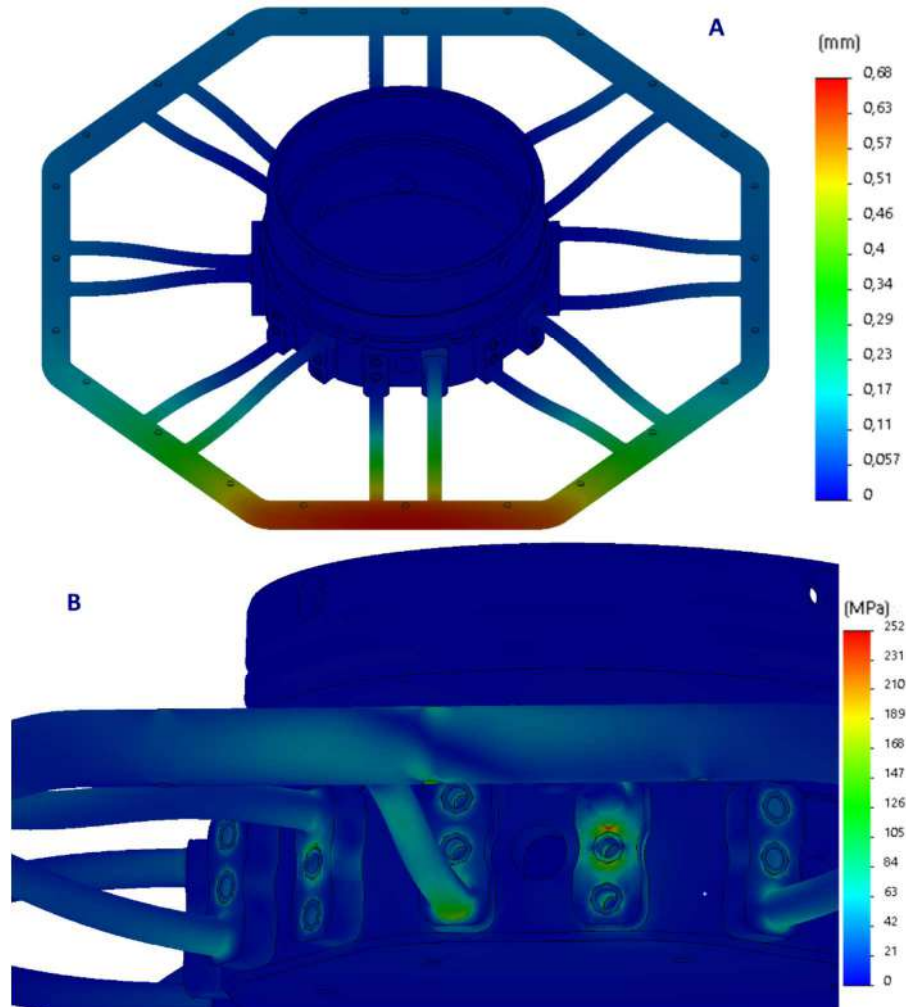
Figure 4.31: Big handle FEM results, displacements (A) and stresses (B).

The central tubes have a thickness of 10 mm, while the external tube is of 20 mm, 3 mm thick. The whole handle system has been designed to be TIG (Tungsten Inert Gas) welded. All the parts, as USBL support, are in stainless steel AISI 316, with a yield strength of 285 MPa, common material for underwater uses and here chosen for its strength as well as its ballast function.

4.5. First testing of the buoy

To conclude, some images of the buoy collected during the first tests are depicted.

First of all the real electronics is shown in Figure 4.32.

Regarding the main PC, the heat sink has been redesigned to fit in the available empty space. To check the goodness of the heat exchange, the main PC has been tested forcing the use of all the four cores at 100% (Figure 4.33):

- 3 hours of work at 23°C room temperature, still air: CPU (Central Processing Unit) maximum reached temperature of 74 °C;
- 1 hour of work at 42°C housing temperature, still air: CPU maximum reached temperature of 85 °C.
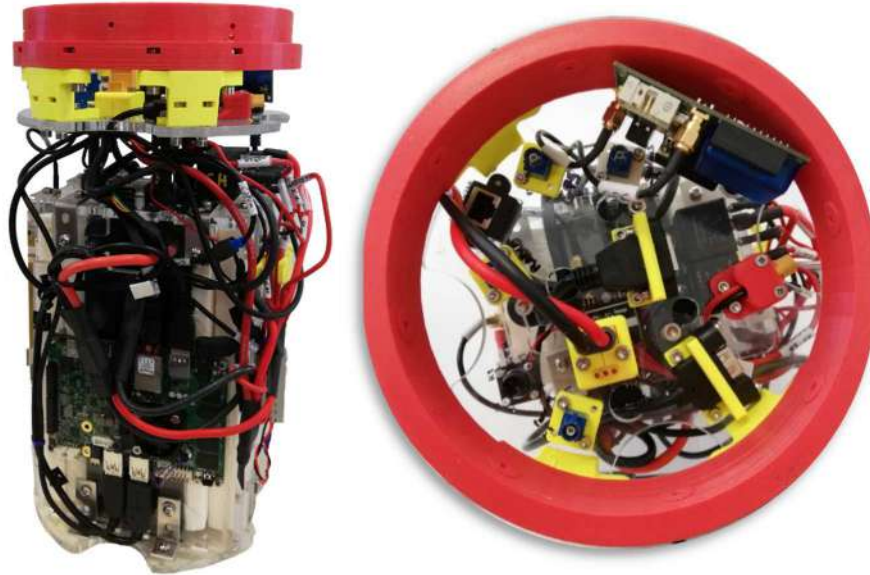
Figure 4.32: Main electronics (perspective and top view).

Figure 4.33: Test for the heat exchange.

Both results are acceptable, since the limit nominal temperature is 90 °C. The electronics, considering only the main PC, the Ethernet switch, the Wi-Fi and the radio modem, requires an energy consumption of 0.5÷0.6 A at 22.3 V.

The buoy watertightness has been also tested; the main housing has been depressurized to 0.5 bar by means of a vacuum pump. The vacuum, in the usual operation, allows the check of the correct assembly by the absence of leakage (Figure 4.34).

Figure 4.34: Vacuum test.

An overall view of the buoy is finally given in Figure 4.35, during a buoyancy test in the swimming pool of the UniFI DIEF MDM Lab.

Figure 4.35: Buoyancy test.

Actually, in the antenna assembly three antennas, instead of two, are visible; this is because there was the opportunity to equip the buoy with a differential GPS. Lastly the buoy has been involved during the test campaigns carried out in La Spezia, thanks to the logistic support of the Naval Experimentation and Support Center (Centro di Supporto e Sperimentazione Navale (CSSN)) of the Italian Navy; the performed tests allowed to assess the performance of the communication between the buoy and FeelHippo AUV, both visible in Figure 4.36, and its proper localization.

Figure 4.36: Communication and localization test.

In the appendix some drafting are gathered.

Conclusions

This work collects the results of the research activity on underwater robotics carried out at the Mechatronics and Dynamic Modelling Laboratory (MDM Lab) of the Department of Industrial Engineering (DIEF) of the University of Florence (UniFI) during the PhD period, years 2016-2019. The activity focused on the study of hull ways of failure, using the test case of FeelHippo AUV, starting from the analysis of state-of-the-art and aiming to the development of new design procedures for thermoformed plastic flanged domes; for this geometry, this study builds on the literature and represents a step forward in collapse prediction theories. Both the cylinder and domes investigated in this study are made of PolyMethyl Methacrylate (PMMA), so the objective of this work is also to adapt the classical methods to a different material and, above all, the production method. Another result of this research activity is the development, realization and preliminary testing of an autonomous self-moving gateway buoy for the localization and communication of underwater targets.

Theoretical and experimental investigations to produce a consistent relationship between both the classic naval design and innovative methods have been presented in this thesis, together with a good correspondence between the experimental evidence and the optimized simulations. Breakage of the hull results in destructive phenomena, namely, yielding and buckling.

Regarding the design of the cylindrical tube, the geometry has been widely studied, and the related theory has been largely used; therefore, it is possible to effectively design this component, even without using FEM analysis in the initial project step. On the other hand, for the dome geometry, the standard theoretical approach is too generic, and the specific results are influenced by boundary conditions, such as geometry and the linking constraints. Therefore, the predictive capacity of the known current algorithms was improved by using the available data in the literature to propose and introduce some correction coefficients. By means of the application of these coefficients, the obtained results are very satisfactory. Furthermore, because of the buckling instability phenomenon, the formula for sizing the dome was combined with the aspect ratio factor. This was implemented because the high region of the dome is affected by this kind of break, and the breaking mode largely depends on the geometry. The other formula predicts the compression break, which occurs in the area of the dome closest to the constraints. Given the strong dependence on the type of constraint and the production methodology of the dome, which even determines the radii of curvature at the base, an overall coefficient was identified for the specific case of a thermoformed plastic flanged dome fixed to the rest of the vehicle by screws. As a result of the adopted changes, the structural resistance to buckling and compression seems to be provided in an effective and correct manner for the specific case under study. A dedicated experimental campaign using a pressure chamber, in which the collapse of available domes was tested, facilitated the creation of a small dataset to extend and validate the proposed theoretical equations.

The main contribution of this research is mainly the proposed design method to identify the mechanical resistance of the domes. For the sake of clarity, the classical theoretical theories and thus the FEM were based on the assumption of a perfect sphere, with only the stiffness of the material taken into account. In this work, the thickness variation and the flange constraints were introduced to consider the real shape of the dome and extrapolate suitable corrective coefficients. The proposed approach starts from the geometrical data and enables the identification of the failure mode and the reachable operational water depth. In conclusion, the proposed innovative method is a lean and effective technique for designing underwater thermoformed plastic hull domes and predicting their collapse pressures.

The second aim of the presented PhD work has been the design of a self-moving autonomous buoy, starting from the analysis of the electronic components, connections among devices and its propulsion system, keeping on with the design of the main mechanical components, thanks to topology optimization too, to end with some preliminary experimental tests. The main field of application of the buoy is the underwater localization but it could also be used, for instance, to collect images of the seabed or to acquire data from the underwater environment, geo-localizing the targets of interest. The buoy has been already involved in some experimental marine tests in collaboration with FeelHippo AUV.

The satisfying results obtained highlight the goodness of the derived solutions. Nonetheless, there is still room for improvements: for instance possible future developments are related to the evaluation of specific coefficients for each application, individual variation in the thickness, the constraint, the manufacturing process, and thereby the material. This requires a much broader experimental campaign that allows each of the, several, coefficients to be studied separately. Because of the costs of shell buckling experiments, the effects of the large number of variables to be considered could be analysed first by a combination of experimental and numerical approaches. Finally, the ultimate goal could be to develop a general method and extend it to different applications. These issues, whose resolution constitutes a natural continuation of the research activity carried out so far, should be subjected to further investigations.

Appendix A

The most significant drawings used for the realization of the buoy are shown below and in the following. Starting from some pieces of the antenna assembly, the floater, the main housing with propulsion and USBL support to the handle.

ROUGHNESS	TOLERANCES	CHAMFERS	MATERIAL AND FINISHES
3,2	UNI EN 22768 f-H	0,5X45°	POM Delrin White

PROJECT NAME: Boa			DATE: 2019/06/03
PRODUCT NAME: Buoy_Antenna_Wifi-RadarSupportClamp			DRAWING: D10.1
COMPANY: Università degli Studi di Firenze			QUANTITY: 3 PCS
SCALE: 1:1	PAPER: 1 of 1	SHEET FORMAT A4	
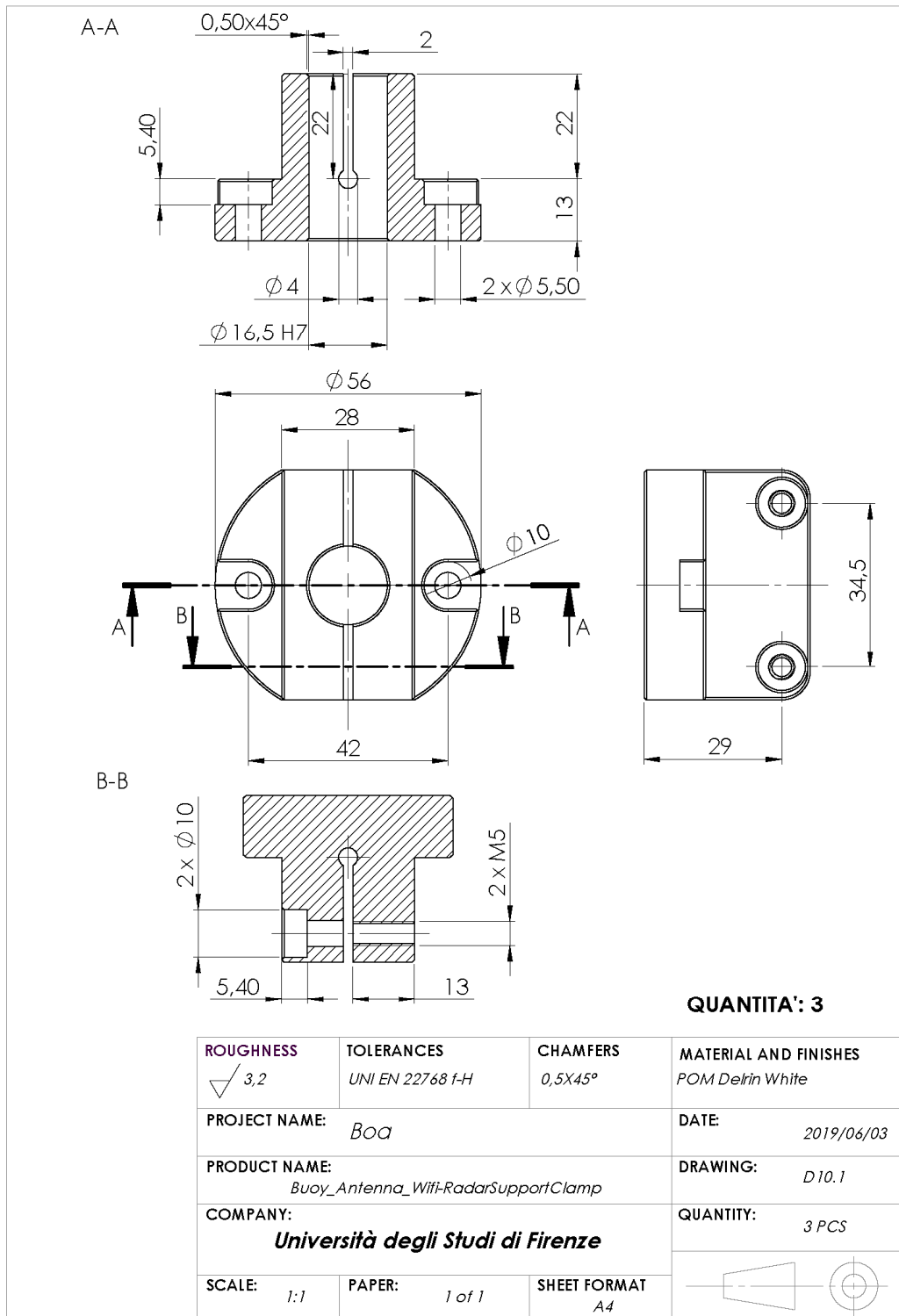
QUANTITA': 3

Drafting A1. 1: Antenna supports.
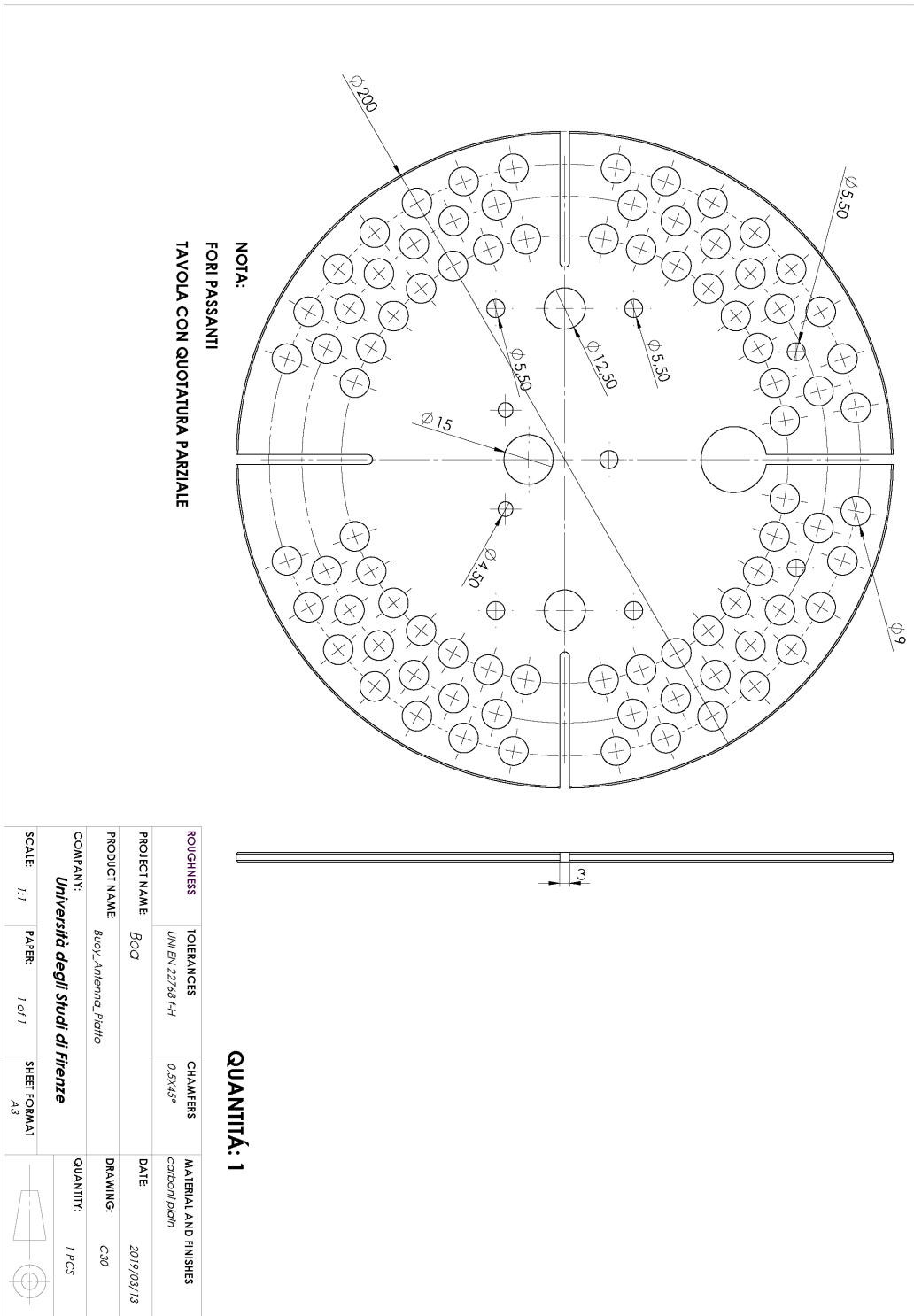
Drafting A1. 2: Main radarable antenna assembly plate.
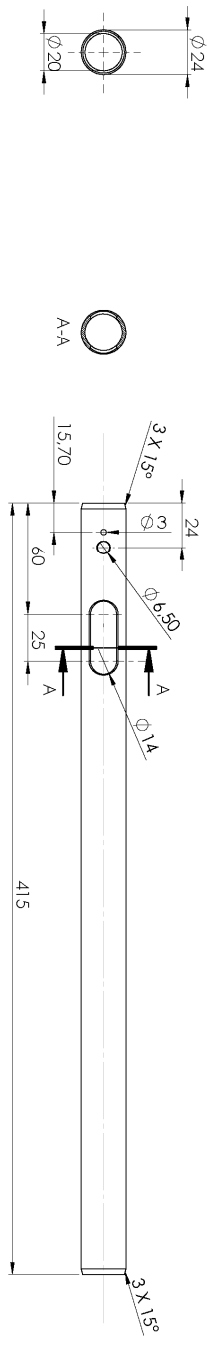
Drafting A1. 3: Antenna rod.
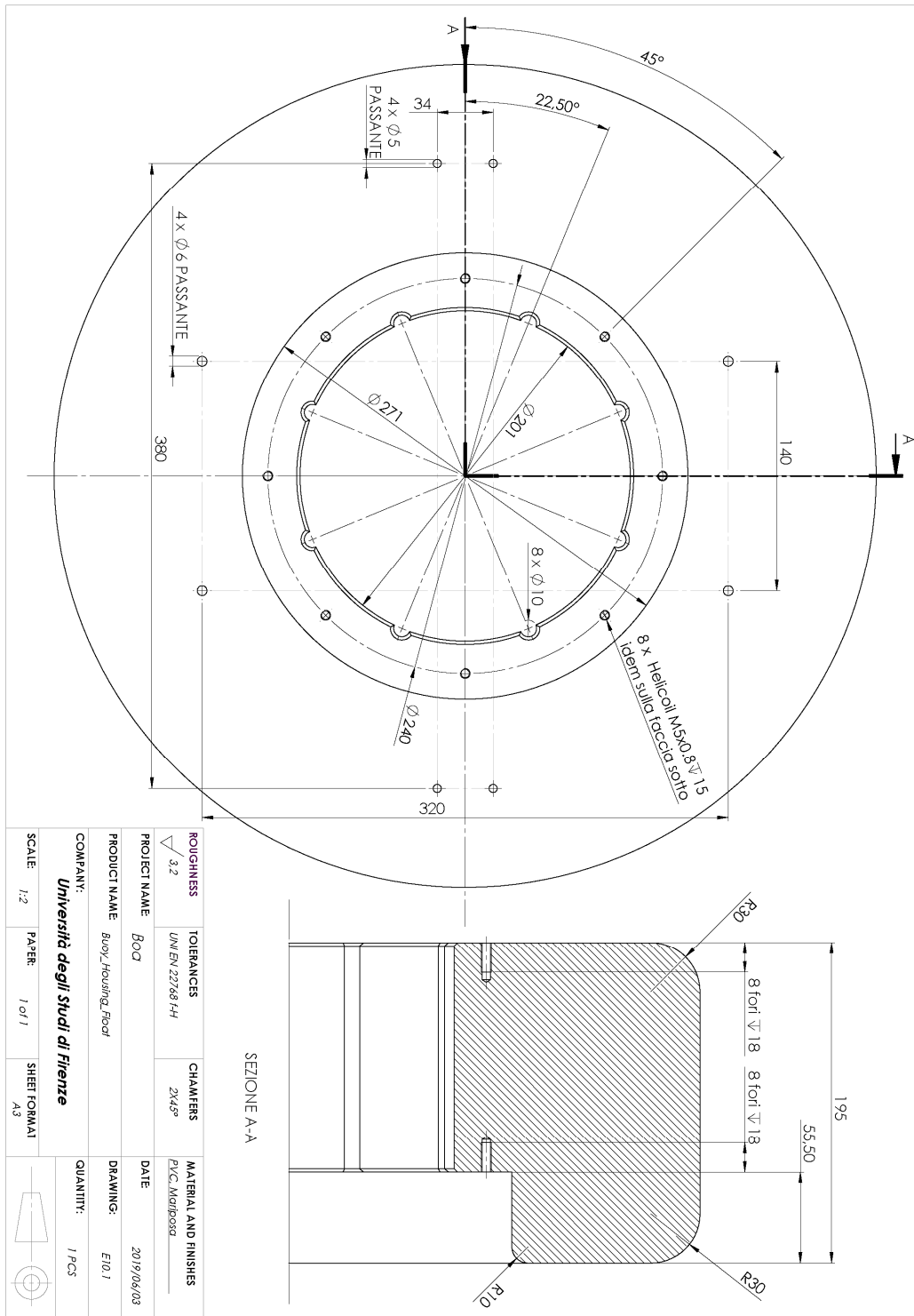
Drafting A1. 4: Floater.
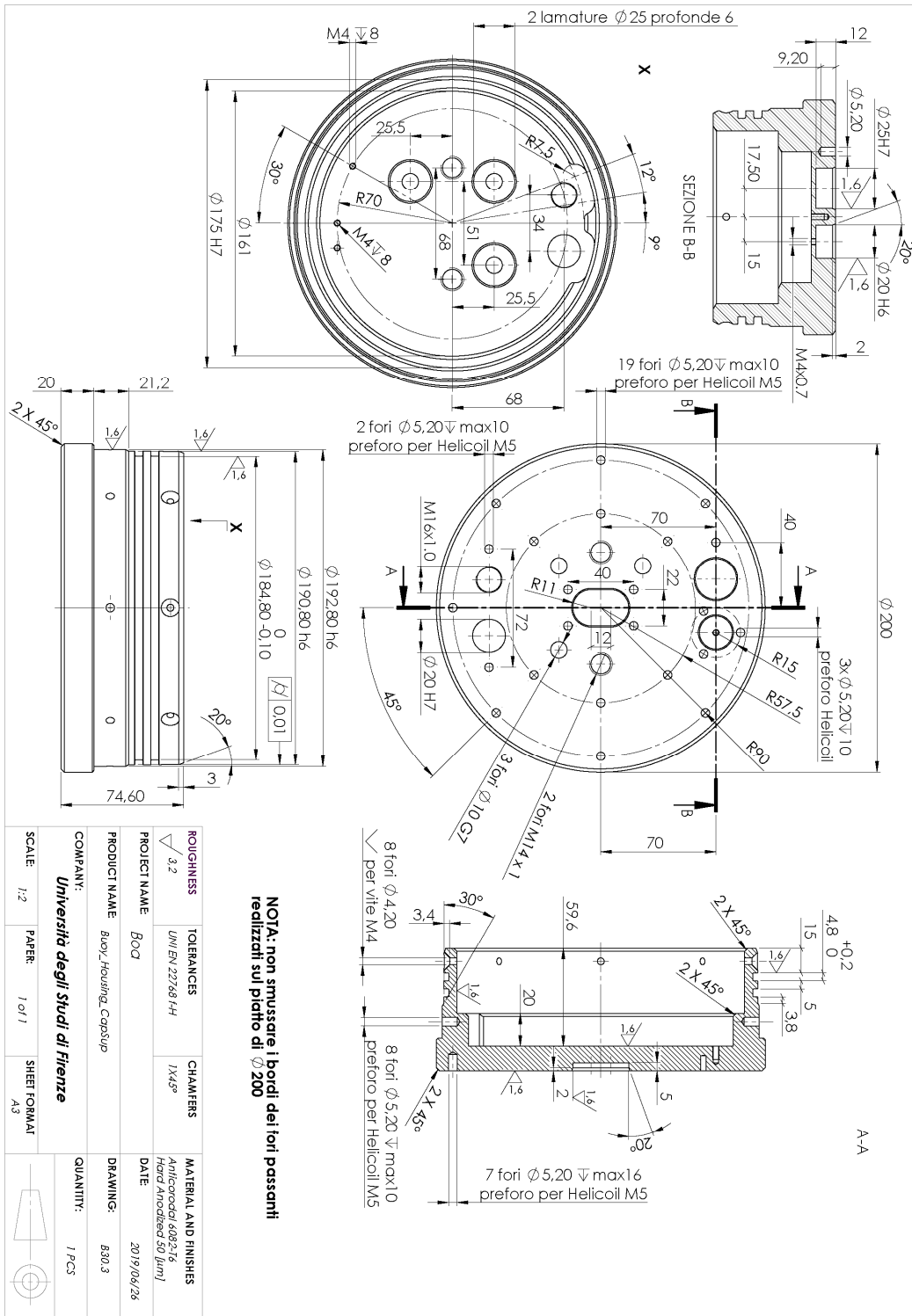
Drafting A1. 5: Upper flange.

Drafting A1. 6: Lower flange.
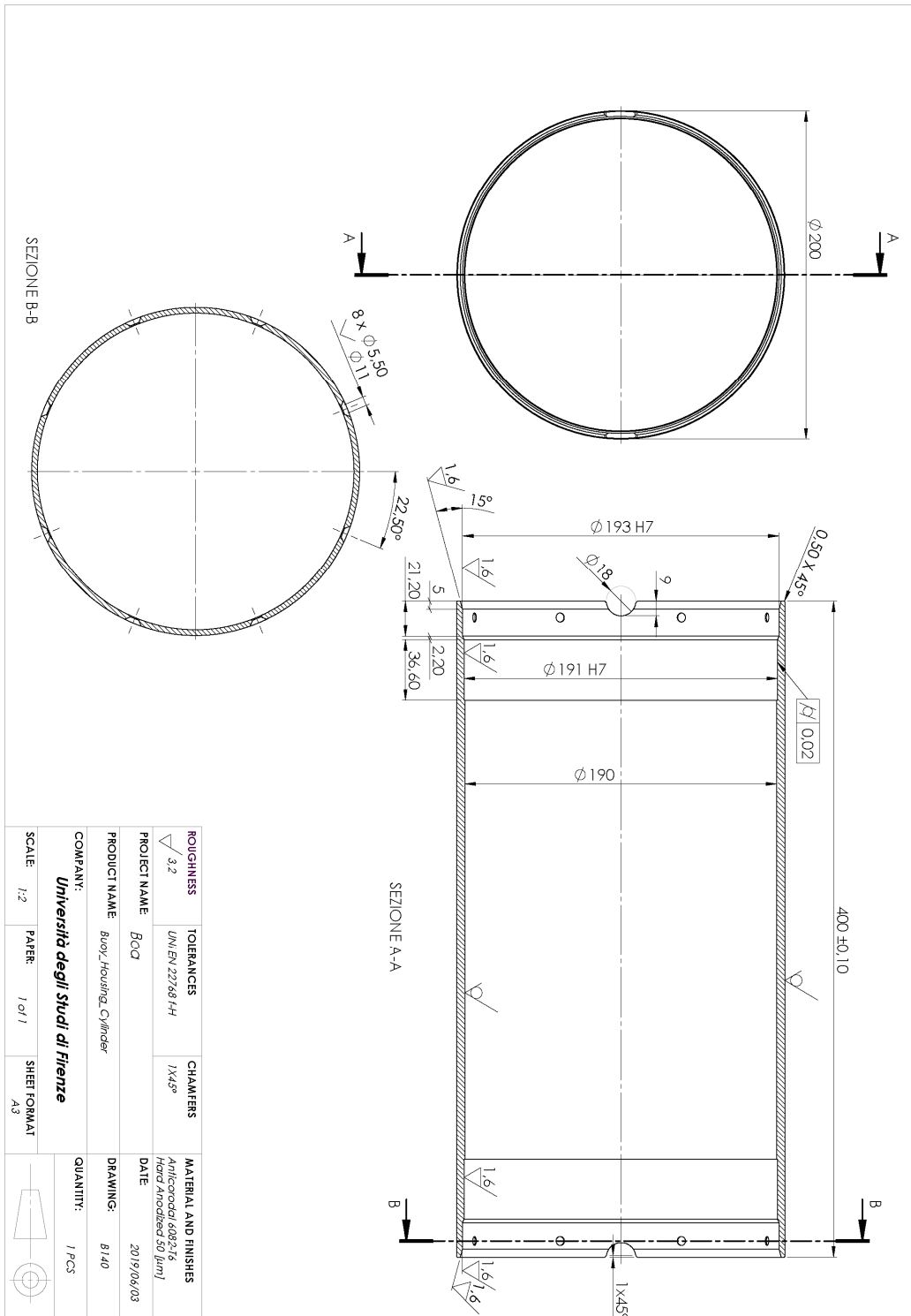
Drafting A1. 7: Main cylinder.
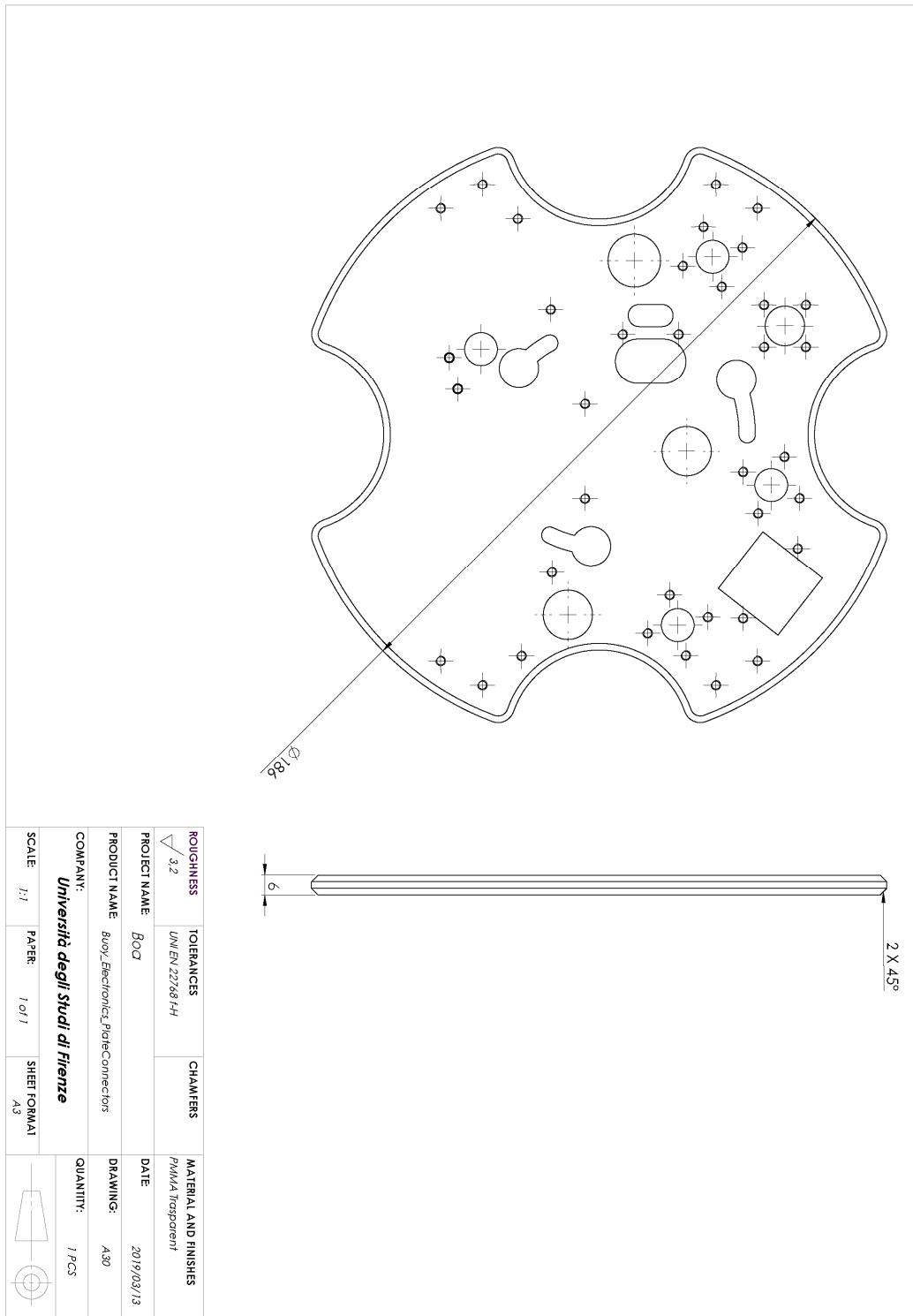
Drafting A1. 8: Example of electronics support plate.

ROUGHNESS
3.2

TOLERANCES	CHAMFERS	MATERIAL AND FINISHES
UNI EN 22768 f-H		PMMA Trasparent

PROJECT NAME: | | DATE: |
BOa | | 2019/03/13 |

PRODUCT NAME: | | DRAWING: |
Buoy_Electronics_PlateConnectors | | A30 |

COMPANY: | | QUANTITY: |
Università degli Studi di Firenze | | 1 PCS |

SCALE:	PAPER:	SHEET FORMAT
1:1	1 of 1	A3

Ø186

6

2 X 45°

NOTA:
SALDATURA TIG TRA 4 E 2
CIANFRINARE SE NECESSARIO IL BORDO DEL COMPONENTE 2 (TAVOLA B70)

SCHEMA MONTAGGIO
2: tavola B70
3: tavola B50
4: tavola B60

c3 45 141

141 c3 45

ROUGHNESS	TOLERANCES	CHAMFERS	MATERIAL AND FINISHES
3.2	UNI EN 22768 f-H		Anticorodal 6082-T6 Hard Anodized 50 [μm]
PROJECT NAME:			DATE:
			2019/03/13
PRODUCT NAME: *Boa*			DRAWING:
Buoy_Motor			M10
COMPANY: *Università degli Studi di Firenze*			QUANTITY:
SCALE: 1:1	PAPER: 1 of 1	SHEET FORMAT A3	

Drafting A1. 9: Propulsion system support.

94
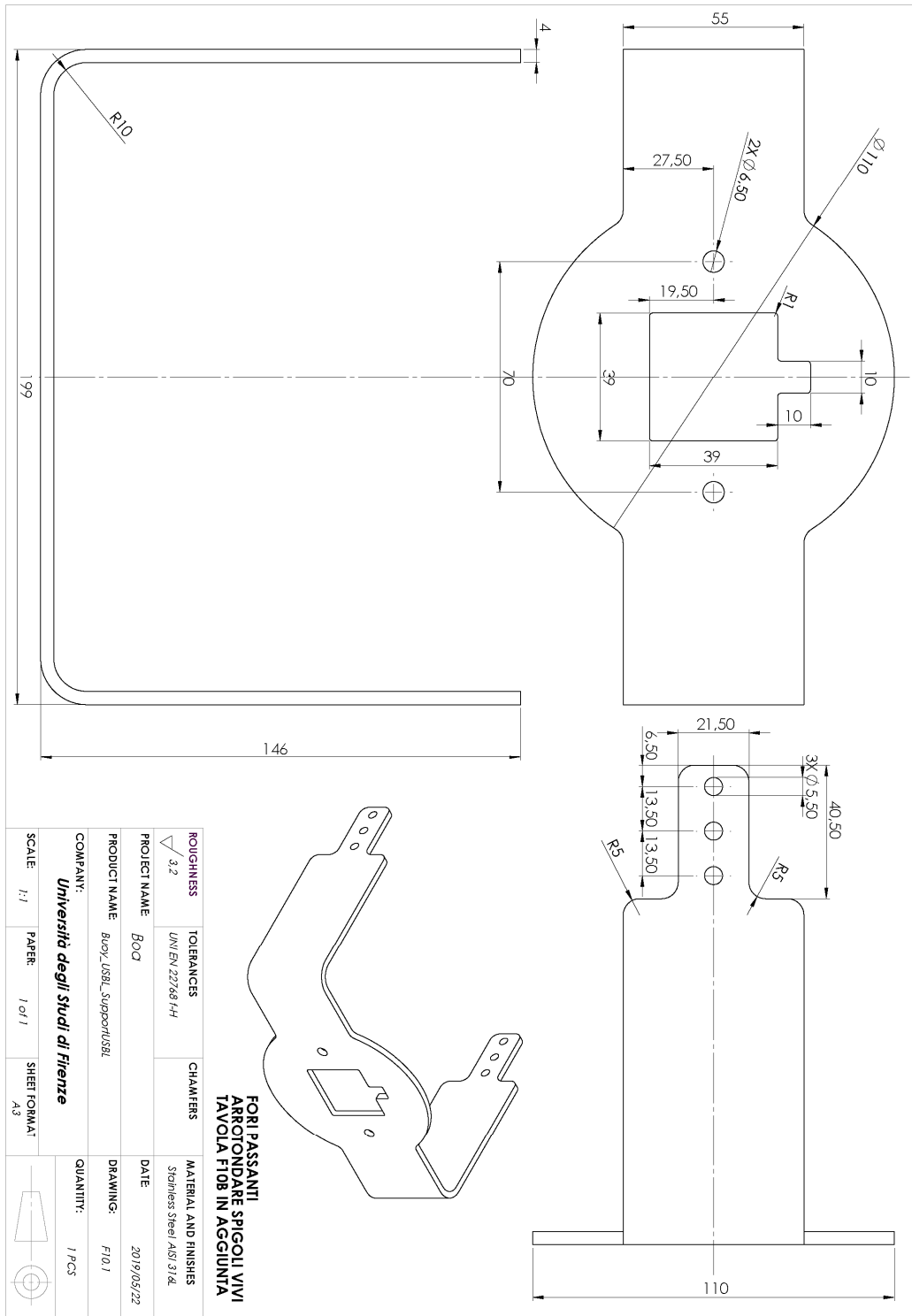
Drafting A1. 10: USBL support.

NOTA:
-RAGGI Ø10 PIENI E PIEGATI:
-TUBOLARE Ø 20 (SPESSORE 3mm) PIEGATO A OTTAGONO
-PIASTRINE FRESATE E FORATE
-SALDATURE SU DIMA
-SALDATURE CONTINUE E COMPLETE
-"RETRO" PIASTRINA LEVIGATO

SEZIONE B-B

40

Ø5.50 Ø10 Ø5.50 18

Ø5PASSANTE

500

3

Ø20

Ø10

Ø191

DETTAGLIO A
SCALA 1 : 2

ROUGHNESS	TOLERANCES	CHAMFERS	MATERIAL AND FINISHES
3.2	UNI EN 22768 f-H		Stainless Steel AISI 316L

PROJECT NAME:		DATE:	MATERIAL AND FINISHES
Boa		2019/03/13	

PRODUCT NAME:
Buoy_Housing_SoftcassieneProtectionRing

		DRAWING:	
		M20	

COMPANY:
Università degli Studi di Firenze

		QUANTITY:	
		1 PCS	

SCALE:	PAPER:	SHEET FORMAT
1:5	1 of 1	A3

Drafting A1. 11: Handle system.
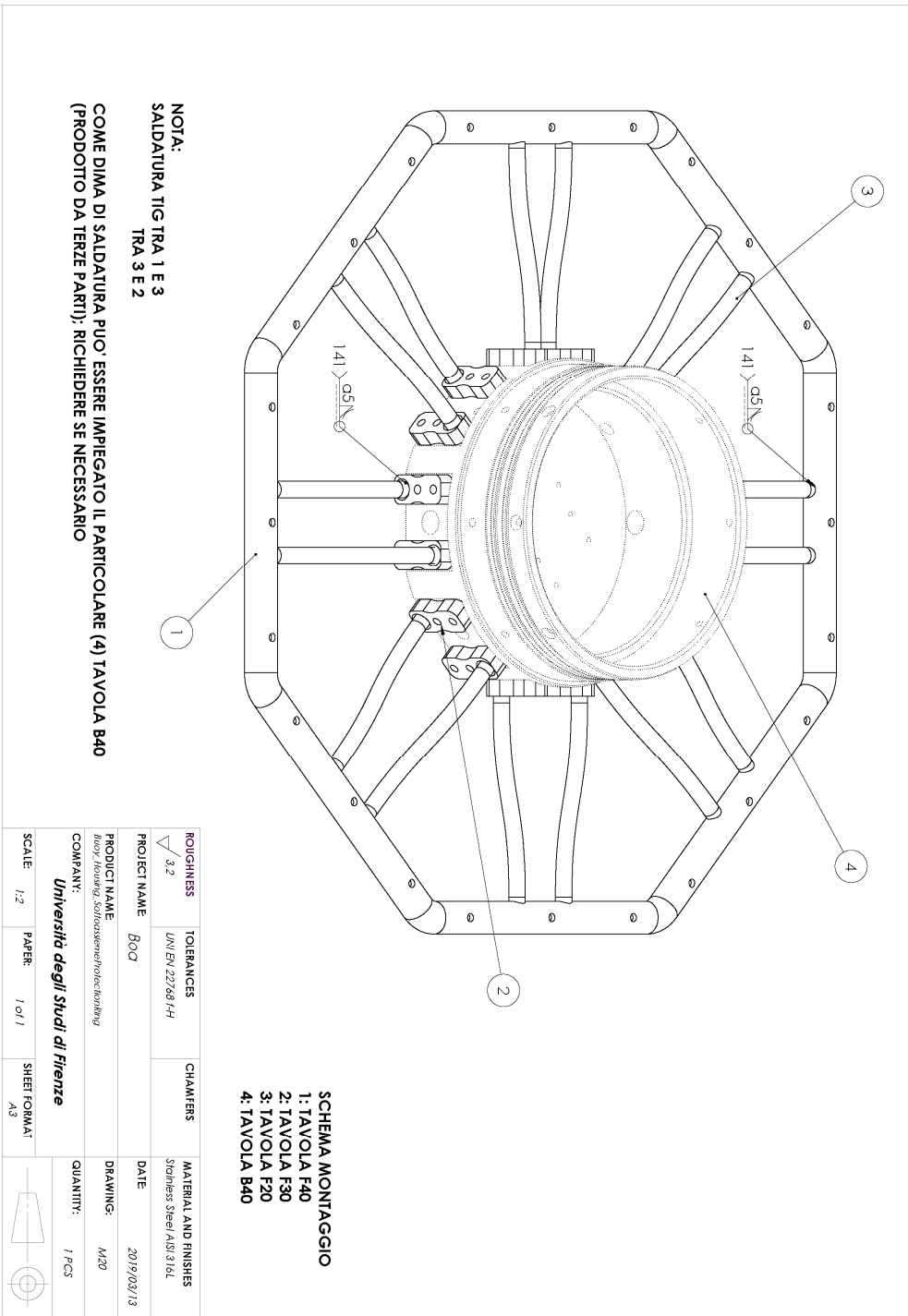
Drafting A1. 12: Handle assembly.

References

[1] R. B. Wynn, V. A. I. Huvenne, T. P. Le Bas, B. J. Murton, D. P. Connelly, B. J. Bett, H. A. Ruhl, K. J. Morris, J. Peakall, D. R. Parsons, E. J. Sumner, S. E. Darby, R. M. Dorrell and J. E. Hunt, "Autonomous Underwater Vehicles (AUVs): Their past, present and future contributions to the advancement of marine geoscience," *Marine Geology,* vol. 352, pp. 451-468, 2014.

[2] L. J. Van Uffelen, E. H. Roth, B. M. Howe, E. M. Oleson and Y. Barkley, "A Seaglider-Integrated digital monitor for bioacoustic sensing," *IEEE Journal of Oceanic Engineering,* vol. 42, no. 4, pp. 800-807, 2017.

[3] S. M. Smith, S. E. Dunn, T. L. Hopkins, K. Heeb and T. Pantelakis, "The application of a modular auv to coastal oceanography: case study on the ocean explorer," in *'Challenges of Our Changing Global Environment'. Conference Proceedings. OCEANS'95 MTS/IEEE*, San Diego, California,USA, 9-12 October 1995.

[4] A. Underwood and C. Murphy, "Design of a micro-AUV for autonomy development and multi-vehicle systems," in *IEEE OCEANS 17*, Aberdeen, Scotland, June 2017.

[5] T. Asai, J. Kojima, K. Asakawa and T. Iso, "Inspection of submarine cable of over 400 km by AUV," in *IEEE International Symposium on UT 00*, Tokio, Japan, May 2000.

[6] M. Jacobi, "Autonomous inspection of underwater structures," *Robotics and Autonomous Systems,* vol. 67, pp. 80-86, 2015.

[7] J. Jamieson, D. Hopkins, M. Arrendondo, J. Evans, K. Hamilton and C. Sotzing, "The potential benefits autonomous underwater vehicles bring to subsea inspection in Arctic regions," *OTC Arctic Technology Conference; Offshore Technology Conference,* 23-25 March 2015.

[8] B. Anderson and J. Crowell, "Workhorse AUV-a cost-sensible new autonomous underwater vehicle for surveys/soundings, search & rescue, and research," in *Proceedings of OCEANS 2005 MTS/IEEE*, Washington, DC, USA, 17-23 September 2005.

[9] S. Venkatesan, "AUV for Search & Rescue at sea-an innovative approach," in *2016 IEEE/OES Autonomous Underwater Vehicles (AUV)*, Tokyo, Japan, 6-9 November 2016.

[10] B. C. R. Allotta, A. Ridolfi, O. Salvetti, M. Reggiannini, M. Kruusmaa, T. Salumae, D. Lane, G. Frost, N. Tsiogkas, M. Cocco, L. Gualdesi, G. Lacava, D. Roig, H. Gundogdu, M. Dede, S. Baines, S. Tusa, P. Latti and D. Scaradozzi, "The ARROWS

Project: robotic technologies for underwater archaeology," in *IOP Conference Series: Materials Science and Engineering (Vol. 364, No. 1, p. 012088). IOP Publishing.*, Florence, Italy, May 2018.

[11] "Official website of the THESAURUS project," 2012. [Online]. Available: http://thesaurus.isti.cnr.it/.

[12] B. Allotta, L. Pugi, F. Bartolini, R. Costanzi, A. Ridolfi, N. Monni, J. Gelli, G. Vettori, L. Gualdesi and M. Natalini, "The THESAURUS project, a long range AUV for extended exploration, surveilance and monitoring of archeological sites," in *V International Conference on Computational Methods in Marine Engineering ECCOMAS MARINE*, Hamburg, Germany, 2013.

[13] B. Allotta, F. Bartolini, A. Caiti, R. Costanzi, F. D. Corato, D. Fenucci, J. GellI, P. Guerrini, N. Monni, A. Munafò, M. Natalini, L. Pugi, A. Ridolfi and J. R. Potter, "Typhoon at CommsNet 2013: experimental experience on AUV navigation and localization," in *19th IFAC World Congress*, August 24-29, 2014.

[14] B. Allotta, L. Pugi, F. Bartolini and A. Ridolfi, "Preliminary design and fast prototyping of an Autonomous Underwater Vehicle propulsion system," *Proceedings of the Institution of Mechanical Engineers, Part M: Journal of Engineering for the Maritime Environment,* vol. 2293, no. 3, p. 248–272, 2015.

[15] B. Allotta, R. Costanzi, L. Pugi and A. Ridolfi, "Identification of the main hydrodynamic parameters of Typhoon AUV from a reduced experimental dataset," *Ocean Engineering,* vol. 147, pp. 77-88, 2018.

[16] "Official website of the ARROWS project," 2015. [Online]. Available: http://www.arrowsproject.eu/.

[17] B. Allotta, R. Costanzi, A. Ridolfi, C. Colombo, F. Bellavia, M. Fanfani, F. Pazzaglia, O. Salvetti, D. Moroni, M. Pascali, M. Reggiannini, M. Kruusmaa, T. Salumae, G. Frost and N. Tsiogkas, "The ARROWS project: adapting and developing robotics technologies for underwater archaeology," *IFAC-PapersOnLine,* vol. 48, no. 2, pp. 194-199, 2015.

[18] B. Allotta, S. Baines, F. Bartolini, F. Bellavia, C. Colombo, R. Conti, R. Costanzi, C. Dede, M. Fanfani, J. Gelli, H. T. Gndogdu, N. Monni, D. Moroni, M. Natalini, M. A. Pascali, F. Pazzaglia, L. Pugi, A. Ridolfi, M. Reggiannini, D. Roig, O. Salvetti and E. Tekdemir, "Design of a modular Autonomous Underwater Vehicle for archaeological investigations," in *IEEE OCEANS 2015,*, Genova, Italy, 18-21 May 2015.

[19] "Official Integrated Systems for the Marine Environment (ISME) website," [Online]. Available: www.isme.unige.it..

[20] "Official website of the ARCHEOSUb project," 2016. [Online]. Available: http://www.archeosub.eu/.

[21] J. Gelli, A. Meschini, N. Monni, M. Pagliai, A. Ridolfi, L. Marini and B. Allotta, "Design and testing of a compact autonomous underwater vehicle for archaeological surveying and monitoring," in *2018 IEEE/OES Autonomous Underwater Vehicle Workshop (AUV)*, Porto, Portugal, 6-9 November 2018.

[22] J. Gelli, A. Meschini, N. Monni, M. Pagliai, A. Ridolfi, L. Marini and B. Allotta, "Development and design of a compact Autonomous Underwater Vehicle: Zeno AUV," in *IFAC-PapersOnLine 51(29), pp. 20-25 11th IFAC Conference on Control Applications in Marine Systems, Robotics, and Vehicles*, Opatija, Croazia, 10-12 September 2018.

[23] "EUMR Project 2018," [Online]. Available: https://www.eumarinerobots.eu/.

[24] R. Limosani, A. Manzi, A. Faggiani, M. Bianchi, M. Pagliai, A. Ridolfi, B. Allotta, P. Dario and F. Cavallo, "Low-cost solution in international robotic challenge: Lessons learned by Tuscany Robotics Team at ERL Emergency Robots 2017," *Journal of Field Robotics,* vol. 36, no. 3, pp. 587-601, 2019.

[25] Centre for Maritime Research and Experimentation, "Official website of the Student Autonomous Underwater Challenge - Europe (SAUC-E) competition," [Online]. Available: http://sauc-europe.org/.

[26] "Official website of the euRathlon competition," [Online]. Available: https://www.eurathlon.eu/.

[27] G. Ferri, F. Ferreira and V. Djapic, "Boosting the talent of new generations of marine engineers through robotics competitions in realistic environments: The SAUC-E and euRathlon experience.," in *IEEE OCEANS 2015*, Genova, Italy, May 2015.

[28] "Official website of the Emergency Robots European Robotics League (ERL)," [Online]. Available: https://eu-robotics.net/robotics_league/.

[29] G. Ferri, F. Ferreira and V. Djapic, "Multi-domain robotics competitions: The CMRE experience from SAUC-E to the European Robotics League Emergency Robots," in *IEEE OCEANS 2017*, Aberdeen, Scotland, 2017, 19-22 June.

[30] G. Ferri, F. Ferreira, V. Djapic, Y. Petillot, M. P. Franco and A. Winfield, "The euRathlon 2015 grand challenge: The first outdoor multi-domain search and rescue robotics competition—A marine perspective.," *Marine Technology Society Journal,* vol. 50, no. 4, pp. 81-97, 2016.

[31] G. Ferri, F. Ferreira and V. Djapic, "Fostering marine robotics through competitions: from SAUC-E to ERL Emergency 2018.," in *OCEANS 2018 MTS/IEEE*, Charleston, 22-25 October 2018.

[32] L. Freitag, M. Grund, C. von Alt, R. Stokey and T. Austin, "A shallow water acoustic network for mine countermeasures operations with autonomous underwater vehicles," Underwater Defense Technology (UDT), 2005.

[33] M. Carreras, C. Candela, D. Ribas, N. Palomeras, L. Magiì, A. Mallios, E. Vidal, E. Pairet and P. Ridao, "Testing SPARUS II AUV, an open platform for industrial, scientific and academic applications," in *Sixth International Workshop On Marine Technology, MARTECH 2015*, Cartagena, Spain, 15-17 September 2015.

[34] R. Costanzi, D. Fenucci, V. Manzari, M. Micheli, L. Morlando, D. Natale, M. Stifani, A. Tesei and A. Caiti, "At-sea NATO operational experimentation with interoperable underwater assets using different robotic middlewares," in *Technology and Science for the Ships of the Future: Proceedings of NAV 2018: 19th International Conference on Ship & Maritime Research*, June 2018.

[35] M. Carreras, J. D. Hern´andez, E. Vidal, N. Palomeras, D. Ribas and P. Ridao, "Sparus II AUV—a hovering vehicle for seabed inspection," *IEEE Journal of Oceanic Engineering,* vol. 43, no. 2, pp. 344-355, 2018.

[36] V. Mittal, S. Dhakad, K. Tyagi, J. Prakash, A. Kumar, Y. Bhagat, A. Singh, S. Bakshi, A. Verma, D. Sharma, L. Mujumdar, A. Arun, M. Pandey, V. H. Prasad, A. Sudhakar, V. Nadkarni, N. Kale, A. Biniwale, A. Taraniya, A. Garg, V. Ramtekar, R. Sudarsanan and P. Rao, "Research and development of Matsya 5.0, autonomous underwater vehicle," 2017. [Online]. Available: http://www.robonation.org/sites/default/files/RS17_IITB_Paper.pdf.

[37] P. H. Milne, Underwater acoustic positioning systems, Houston, TX: Gulf Publishing Co., 1983.

[38] F. Mandić, N. Mišković, N. Palomeras, M. Carreras and G. Vallicrosa, "Mobile beacon control algorithm that ensures observability in single range navigation," *IFAC-PapersOnLine,* vol. 49, no. 23, pp. 48-53, 2016.

[39] D. R. Yoerger, M. Jakuba, A. M. Bradley and B. Bingham, "Techniques for Deep Sea Near Bottom Survey Using an Autonomous Underwater Vehicle," *The International Journal of Robotics Research,* 1 January 2007.

[40] D. Moroni, G. Pieri, O. Salvetti, M. Tampucci, C. Domenici and A. Tonacci, "Sensorized buoy for oil spill early detection," *Methods in Oceanography,* vol. 17, pp. 221-231, 2016.

[41] R. D. Chris and R. L. Wernli, The ROV Manual. A User Guide for Observation Class Remotely Operated Vehicles, Elsevier, 2011.

[42] G. Icolari, Remotely Operated Vehicle: Hand Book for ROV Pilot Technician, Atlantis Deep Sea Ltd, 2018.

[43] O. A. N. Eidsvik, B. O. Arnesen and I. Schjolberg, "SeaArm-A Subsea Multi-Degree of Freedom Manipulator for Small Observation Class Remotely Operated Vehicles," in *2018 European Control Conference (ECC)*, Limassol, Cyprus, 12-15 June 2018.

[44] H. R. Widditsch, SPURV - The First Decade, October 1973.

[45] A. Alvarez, A. Caffaz, A. Caiti, G. Casalino, L. Gualdesi, A. Turetta and R. Viviani, "Fòlaga: a low-cost autonomous underwater vehicle combining glider and AUV capabilities," *Ocean Engineering,* vol. 36, no. 1, pp. 24-38, 2009.

[46] B. Fletcher, S. Martin, G. Flores, A. Jones, A. Nguyen, M. H. Brown and D. L. Moore, "From the lab to the ocean: characterizing the critical docking parameters for a free floating dock with a REMUS 600," in *IEEE OCEANS 17*, Anchorage, Alaska, September 2017.

[47] C. von Alt, B. Allen, T. Austin and R. Stokey, "Remote environmental measuring units," in *Proceedings of IEEE Symposium on Autonomous Underwater Vehicle Technology (AUV'94)*, Cambridge, MA, USA, 19-20 July 1995.

[48] A. Kukulya, A. Plueddemann, T. Austin, R. Stokey, M. Purcell, B. Allen, R. Littlefield, L. Freitag, P. Koski, E. Gallimore, J. Hemp, K. Newhall and J. Pietro, "Under-ice operations with a REMUS-100 AUV in the Arctic," in *2010 IEEE/OES Autonomous Underwater Vehicles*, Monterey, CA, USA, 1-3 September 2010.

[49] M. Johnson-Roberson, M. Bryson, A. Friedman, O. Pizarro, G. Troni, P. Ozog and J. C. Henderson, "High-resolution underwater robotic vision-based mapping and three-dimensional reconstruction for archaeology," *Journal of Field Robotics,* vol. 34, no. 4, pp. 625-643, 2017.

[50] B. Bingham, B. Foley, H. Singh, R. Camilli, K. Delaporta, R. Eustice, A. Mallios, D. Mindell, C. Roman and D. Sakellariou, "Robotic tools for deep water archaeology: Surveying an ancient shipwreck with an autonomous underwater vehicle," *Journal of Field Robotics,* vol. 27, no. 6, pp. 702-717, 2010.

[51] R. Yeo, "Surveying the underside of an Arctic ice ridge using a man-portable GAVIA AUV deployed through the ice," in *IEEE OCEANS 2007*, Vancouver, BC, Canada, 29 September-4 Ocober 2007.

[52] J. C. Kinsey, D. R. Yoerger, M. V. Jakuba, R. Camilli, C. R. Fisher and C. R. German, "Assessing the Deepwater Horizon Oil Spill with the Sentry Autonomous Underwater Vehicle," in *2011 IEEE/RSJ International Conference on Intelligent Robots and Systems*, San Francisco, CA, USA, September 25-30, 2011.

[53] J. A. Curcio, P. A. McGillivary, K. Fall, A. Maffei, K. Schwehr, B. Twiggs, C. Kitts and P. Ballou, "Self-positioning smart buoys, the" un-buoy" solution: Logistic considerations using autonomous surface craft technology and improved communications infrastructure," in *IEEE OCEANS 2006*, September 2006.

[54] B. Anderson and A. Kleiner, "Autonomous Surface Vehicles for Arctic Data Collection.," in *OTC Arctic Technology Conference. Offshore Technology Conference*, Houston, Texas, USA, February 2014.

[55] T. S. Husøy, F. R. Knudsen, B. Gjelstad and A. Furdal, "Product development at kongsberg maritime related to underwater sensor networks," in *Proceedings*

of the Seventh ACM International Conference on Underwater Networks and Systems, Toronto, Canada, November 2012.

[56] H. Ferreira, C. M. A. Almeida, J. Almeida, N. Dias, A. Dias and E. Silva, "Autonomous Bathymetry for Risk Assessment with ROAZ Robotic Surface Vehicle," in *IEEE Oceans 2009-Europe*, Bremen, Germany, 11-14 May 2009.

[57] R. Heitsenrether, L. Fiorentino, W. Hensley, E. Breuer and W. Krug, "NOAA's recent development of a real-time ocean observing system to support safe navigation along US Arctic Coasts," in *OCEANS 2017-IEEE*, Anchorage, Alaska, September 2017.

[58] H. Senga, N. Kato, H. Suzuki, T. Akamatsu, L. Yu, M. Yoshie and T. Tanaka, "Field experiments and new design of a spilled oil tracking autonomous buoy," *Journal of Marine Science and Technology,* vol. 19, no. 1, pp. 90-102, 2014.

[59] G. Hitz, F. Pomerleau, M.-E. Garneau, C. Pradalier, T. Posch, J. Pernthaler and R. Y. Siegwart, "Autonomous inland water monitoring: Design and application of a surface vessel," *IEEE Robotics & Automation Magazine,* vol. 19, no. 1, pp. 62-72, 2012.

[60] R. Onken, H. V. Fiekas, L. Beguery, I. Borrione, A. Funk, M. Hemming, J. Hernandez-Lasheras, K. J. Heywood, J. Kaiser, M. Knoll, B. Mourre, P. Oddo, P. M. Poulain, B. Y. Queste, A. Russo, K. Shitashima, M. Siderius and E. T. Küsel, "High-resolution observations in the western Mediterranean Sea: the REP14-MED experiment.," *Ocean Science,* vol. 14, no. 2, pp. 321-335, 2018.

[61] Datawell BV, Laboratory for instrumentation, "Datawell Waverider reference manual," www.datawell.nl, Haarlem, The Netherlands, 2006.

[62] Datawell, "Waverider Gps-based Buoy," [Online]. Available: http://www.datawell.nl/products/buoys.aspx.

[63] AUVAC, "AUV Gateway Buoy," [Online]. Available: https://auvac.org/navigations/view/42.

[64] OSIL, "Mooring-free Buoy," [Online]. Available: https://osil.com/wp-content/uploads/2018/12/Mooring-Free-Buoy.pdf.

[65] L3ASV, "C-Stat 2 Station Keeping Buoy," [Online]. Available: https://www.asvglobal.com/wp-content/uploads/2019/04/C-Stat2_2019.pdf.

[66] D. Wettergreen, C. Gaskett and A. Zelinsky, "Development of a visually-guided Autonomous Underwater Vehicle," *IEEE Oceanic Engineering Society. OCEANS'98. Conference Proceedings (Cat. No. 98CH36259),* vol. 2, pp. 1200-1204, 1998.

[67] E. Marchand, F. Chaumette, F. Spindler, M. Perrier and I. Toulon, "Controlling the manipulator of an underwater ROV using a coarse calibrated pan/tilt

camera," in *Proceedings 2001 ICRA. IEEE International Conference on Robotics and Automation (Cat. No. 01CH37164)*, Seoul, South Korea, South Korea, 21-26 May 2001.

[68] C. T. Ross, A. P. Little, G. X. Brown and A. Spahiu, "Buckling of near-perfect thick-walled circular cylinders under-external Hydrostatic pressure," *Journal of Ocean Technology,* vol. 4, no. 2, pp. 84-103, 2009.

[69] C. Ross, A. Little, D. Short and G. Brown, "Inelastic buckling of geometrically imperfect tubes under external hydrostatic pressure," *Journal of Ocean Technology,* vol. 3, no. 1, pp. 75-90, 2008.

[70] W. Wunderlich and U. Albertin, "Buckling behaviour of imperfect spherical shells," *International Journal of Non-linear mechanics,* vol. 37, no. 4-5, pp. 589-604, 2002.

[71] M. Lai and D. Holt, "Thickness variation in the thermoforming of poly (methyl methacrylate) and high-impact polystyrene sheets," *Journal of Applied Polymer Science,* vol. 19, no. 7, pp. 1805-1814, 1975.

[72] V. Carvelli, N. Panzeri and C. Poggi, "Buckling strength of GFRP under-water vehicles," *Composites Part B: Engineering,* vol. 32, no. 2, pp. 89-101, 2001.

[73] J. Singer, J. Arbocz and T. Weller, Buckling experiments: experimental methods in buckling of thin-walled structures. Shells, built-up structures, composites and additional topics, New York: John Wiley \& Sons., 2002.

[74] J. W. Hutchinson, "Buckling of spherical shells revisited," *Proceedings of the Royal Society A: Mathematical, Physical and Engineering Sciences,* vol. 472, no. 2195, p. 20160577, 2016.

[75] C. Ross, Pressure Vessels - External pressure technology, Cambridge: Elsevier, Woodhead Publishing, 2011.

[76] K. Breddermann, P. Drescher, C. Polzin, H. Seitz and M. Paschen, "Printed pressure housings for underwater applications," *Ocean Engineering,* vol. 113, pp. 57-63, 2016.

[77] J. Zhang, M. Zhang, W. Tang, W. Wang and M. Wang, "Buckling of spherical shells subjected to external pressure: a comparison of experimental and theoretical data," *Thin-Walled Structures,* vol. 111, pp. 58-64, 2017.

[78] K. Vickery, "Acoustic positioning systems. A practical overview of current systems," in *Proceedings of the 1998 Workshop on Autonomous Underwater Vehicles (Cat. No. 98CH36290)*, Cambridge, 13-14 October 1998.

[79] F. Fanelli, N. Monni, N. Palma and A. Ridolfi, "Development of an ultra short baseline–aided buoy for underwater targets localization," *Proceedings of the*

Institution of Mechanical Engineers, Part M: Journal of Engineering for the Maritime Environment, 2019.

[80]   A. Vasilijević, D. and Nad and N. Mišković, "Autonomous Surface Vehicles as Positioning and Communications Satellites for the Marine Operational Environment—Step toward Internet of Underwater Things," in *2018 IEEE 8th International Conference on Underwater System Technology: Theory and Applications (USYS)*, Wuhan, (China), 1-3 December 2018.

[81]   A. Munafò and G. Ferri, "An acoustic network navigation system," *Journal of Field Robotics ,* vol. 34, no. 7, pp. 1332-1351, 2017.

[82]   W. Yan, W. Chen, R. Cui and H. Li, "Optimal distance between mobile buoy and target for moving long baseline positioning system," *The Journal of Navigation,* vol. 68, no. 4, pp. 809-826, 2015.

[83]   K. Alam, T. Ray and S. G. Anavatti, "A new robust design optimization approach for unmanned underwater vehicle design," *Proceedings of the Institution of Mechanical Engineers, Part M: Journal of Engineering for the Maritime Environment,* vol. 226, no. 3, pp. 235-249, 2012.

[84]   T. Reynolds, O. Lomacky and M. Krenzke, "Design and analysis of small submersible pressure hulls," *Computers and Structures,* vol. 3, no. 5, pp. 1125-1143, 1973.

[85]   X. D. Fan, *Design and analysis of carrier for ocean-exploration AUV,* vol. 2008, Harbin Engineering University: PhD thesis, 2008.

[86]   C. T. Ross, "A conceptual design of an underwater vehicle," *Ocean Engineering,* vol. 33, no. 16, pp. 2087-2104, 2006.

[87]   Z. Xinlong, W. Weibo, T. Wenxian and W. Tang, "Overviews of investigation on submersible pressure hulls," *Advances in Natural Science,* vol. 7, no. 4, pp. 54-61, 2014.

[88]   K. R. Deepika and N. J. Kumar, "Design optimisation of a pressure hull for dynamic loading," *International Journal of Engineering Science and Innovative Technology ,* vol. 2, no. 6, pp. 562-586, 2013.

[89]   A. Jebelli, C. Yagoub and S. Dhillon, "Design and Implementation of an Autonomous Underwater Vehicle (AUV) with PTFE," *Advances in Robotics & Automation,* vol. 7, no. 1, 2018.

[90]   C.-J. Moon, I.-H. Kim, B.-H. Choi, J.-H. Kweon and J.-H. Choi, "Buckling of filament-wound composite cylinders subjected to hydrostatic pressure for underwater vehicle applications," *Composite Structures,* vol. 92, no. 9, pp. 2241--2251, 2010.

[91] A. Marinò, "Mezzi sottomarini - appunti del corso di navi militari e sommergibili, 4," University of Trieste, 2012.

[92] R. Zoely, *Über ein Knickproblem an der; (About a kink problem at the spherical shell).,* Zurich, 1915.

[93] S. Krishnamachari and L. J. Broutman, "A design procedure for large spherical domes under external pressure," *Journal of reinforced plastics and composites,* vol. 16, no. 14, pp. 1342-1349, 1997.

[94] S. N. Amiri and H. A. Rasheed, "Nondestructive method to predict the buckling load in elastic spherical shells," *Engineering Structures,* vol. 150, pp. 300-317, 2017.

[95] C. Ross, A. McLennan and A. Little, "Nonlinear vibration of a hemispherical dome under external water pressure," *Journal of Physics: Conference Series,* vol. 305, no. 1, 2011.

[96] Altair, "Hyperworks 13.0 Desktop User Guide," 2017.

[97] S. Peng-Li, "Buckling analysis of nonlinear structures using Lanczos method," *Computers and Structures,* vol. 36, no. 6, pp. 1111-1120, 1990.

[98] B. Moradi and I. Parsons, "A comparison of techniques for computing the buckling loads of stiffened shells," *Computersand structures,* vol. 46, no. 3, pp. 505-514, 1993.

[99] O. C. Zienkiewicz, R. L. Taylor, P. Nithiarasu and J. Zhu, "The finite element method," London, McGraw-hill, 1977.

[100] E. Ramm and H. Stegmüller, "The displacement finite element method in nonlinear buckling analysis of shells," *Buckling of shells,* pp. 201-235, 1982.

[101] L. Wullschleger and H. Meyer-Piening, "Buckling of geometrically imperfect cylindrical shells—definition of a buckling load," *International Journal of Non-Linear Mechanics,* vol. 37, no. 4-5, pp. 645-657, 2002.

[102] M. P. Bendsoe and O. Sigmund, Topology optimization: theory, methods, and applications, Springer Science & Business Media, 2013.

[103] N. Olhoff, "On optimum design of structures and materials," *Meccanica,* vol. 31, no. 2, pp. 143-161, 1996.

[104] S. O. Degertekin, "Improved harmony search algorithms for sizing optimization of truss structures," *Computers and structures,* vol. 92, pp. 229-241, 2012.

[105] R. Drazumeric and F. Kosel, "Shape optimization of beam due to lateral buckling problem," *International Journal of Non-Linear Mechanics,* vol. 47, no. 3, pp. 65-74, 2012.

[106] P. Hajela and E. Lee, "Genetic algorithms in truss topological optimization," *International journal of solids and structures,* vol. 32, no. 22, pp. 3341-3357, 1995.

[107] W. Prager, "A note on discretized Michell structures," *Computer Methods in Applied Mechanics and Engineering,* vol. 3, no. 3, pp. 349-355, 1974.

[108] M. N. Sudin, M. M. Tahir, F. R. Ramli and S. A. Shamsuddin, "Topology optimization in automotive brake pedal redesign," *International Journal of Engineering and Technology (IJET),* vol. 6, no. 1, pp. 398-402, 2014.

[109] M. Bianchi, F. Buonamici, R. Furferi and N. Vanni, "Design and," in *ASME 2016 International Design Engineering Technical Conferences and Computers and Information in Engineering Conference*, Charlotte, North Carolina, USA, 21-24 August 2016.

[110] N. Secciani, M. Bianchi, A. Meschini, A. Ridolfi, Y. Volpe, L. Governi and B. Allotta, "Assistive hand exoskeletons: the prototypes evolution at the University of Florence," in *The International Conference of IFToMM*, Cassino, Italy, 29-30 November 2018.

[111] B.-C. Chen and N. Kikuchi, "Topology optimization with design-dependent loads," *Finite Elements in Analysis and Design,* vol. 37, no. 1, pp. 57-70, 2001.

[112] B. Pan and W. Cui, "Structural optimization for a spherical pressure hull of a deep manned submersible based on an appropriate design standard," *IEEE Journal of Oceanic Engineering,* vol. 37, no. 3, pp. 564-571, 2012.

[113] M. Pagliai, A. Ridolfi, J. Gelli, A. Meschini and B. Allotta, "Design of a Reconfigurable Autonomous Underwater Vehicle for Offshore Platform Surveying and Monitoring," in *2018 IEEE/OES Autonomous Underwater Vehicle Workshop (AUV)*, Porto, Portugal , 6-9 November 2018.

[114] M. Bendsoe and O. Sigmund, Topology optimization: theory, methods and applications, Springer, 2003.

[115] M. Y. Wang, X. Wang and D. Guo, "A level set method for structural topology optimization," *Computer methods in applied mechanics and engineering,* vol. 192, no. 1 - 2, pp. 227-246, 2003.

[116] L. Shu, M. Y. Wang, Z. Fang, Z. Ma and P. Wei, "Level set based structural topology optimization for minimizing frequency response," *Journal of Sound and Vibration,* vol. 220, no. 24, pp. 5820-5834, 2011.

[117] G. I. Rozvany, "Aims, scope, methods, history and unified terminology of computer-aided topology optimization in structural mechanics," *Structural and Multidisciplinary optimization,* vol. 21, no. 2, pp. 90-108, 2001.

[118] S. Osher and R. P. Fedkiw, "Level set methods: an overview and some recent results," *Journal of Computational physics,* vol. 169, no. 2, pp. 462-502, 2001.

[119] B. Allotta, R. Conti, R. Costanzi, F. Fanelli, J. Gelli, E. Meli, N. Monni, A. Ridolfi and A. Rindi, "A low cost autonomous underwater vehicle for patrolling and monitoring," *Proceedings of the Institution of Mechanical Engineers, Part M: Journal of Engineering for the Maritime Environment,* vol. 231, no. 3, pp. 740-749, 2017.

[120] A. Meschini, A. Ridolfi, J. Gelli, M. Pagliai and A. Rindi, "Pressure hull design methods for Unmanned Underwater Vehicles," *Journal of Marine Science and Engineering, Ocean Engineering,* vol. 7, no. 11, p. 382, 28 October 2019.

[121] J. Carlton, Marine propeller and propulsion, Amsterdam, Holland: Butterworth - Heinemann, 2007.

[122] T. I. Fossen, Guidance and control of ocean vehicles, Chichester UK: John Wiley & Sons, 1994.

[123] Det Norske Veritas, *DNVGL-CG-0128 Class Guideline Buckling,* Høvik, Norway, 2015.

[124] R. Von Mises and D. Windenburg, "The critical external pressure of cylindrical tubes under uniform radial and axial load," DAVID TAYLOR MODEL BASIN WASHINGTON DC, 1933.

[125] R. G. Sturm, "A study of the collapsing pressure of thin-walled cylinders," University of Illinois, Urbana Champaign, College of Engineering, 1941.

[126] T. E. Reynolds, "Inelastic lobar buckling of cylindrical shells under external,Report No.1392," DAVID TAYLOR MODEL BASIN WASHINGTON DC, Cameron Station Alexandria,Virginia, August 1960.

[127] S. S. Seleim and J. Roorda, "Buckling behaviour of ring-stiffened cylinders, experimental," *Thin-walled structures,* vol. 4, no. 3, pp. 203-222, 1986.

[128] K. Hom and W. P. Couch, "Hydrostatic tests of inelastic and elastic stability of ring-stiffened cylindrical shells machined from strain-hardening steel Report No.1501," Navy Department, David Taylor Model Basin, 1961.

[129] C. T. Ross, P. Haynes, A. Seers and T. Johns, "Inelastic buckling of ring-stiffened circular cylinders under uniform external pressure," *Proceedings International Conference of Structural Dynamics and Vibration, ASME,* vol. 70, pp. 207-215, 1995.

[130] C. T. Ross and T. Johns, "The effect of stiffener size on interframe shell instability of ring-reinforced circular cylinders," *Journal of Ship Research,* vol. 15, pp. 141-143, 1971.

[131] C. Ross and J. Kimber, "Plastic axisymmetric buckling of thin-walled circular cylinders under uniform external pressure," American Society of Mechanical Engineers, New York, United States, 1996.

[132] C. T. F. Ross, Interviewee, *Collapse of ring-reinforced cylinders under uniform external pressure.* [Interview]. 1963.

[133] C. T. Ross, K. O. Okoto and A. P. Little, "Buckling by general instability of cylindrical components of deep sea submersibles," *Applied Mechanics and Materials,* vol. 12, pp. 289-296, 2008.

[134] "BlueRobotics tests," [Online]. Available: https://bluerobotics.com/new-products-aluminum-tubes/. [Accessed 2018 March 23].

[135] A. Lee, L. J. Francisco, J. Marthelot, J. W. Hutchinson and P. M. Reis, "The geometric role of precisely engineered imperfections on the critical buckling load of spherical elastic shells," *Journal of Applied Mechanics,* vol. 83, no. 11, 2016.

[136] T. Kàrmàn and H. Tsien, "The buckling of spherical shells by external pressure," *Journal of the Aeronautical Sciences,* vol. 7, no. 2, pp. 43-50, 1939.

[137] W. Young and R. Budynas, Roark's formulas for stress and strain, New York: McGraw-Hill, 2002.

[138] J. Rotter, G. Mackenzie and M. Lee, "Spherical dome buckling with edge ring support," *Structures,* vol. 8, pp. 264-274, 2016.

[139] Det Norske Veritas, *DNV CN30.1 Buckling strength analysis of bars and frames, and spherical shells,* Høvik, Norway, 2004.

[140] P. Ewing and J. Williams, "The fracture of spherical shells under pressure and circular tubes," *International Journal of Fracture,* vol. 10, no. 4, pp. 537-544, 1974.

[141] "Formatura di PLEXIGLAS - Direttive per la lavorazione (Evonik Industries)," 2008. [Online]. Available: https://www.plexiglas-shop.com/pdfs/it/311-2%20Formatura%20di%20PLEXIGLAS%C2%AE_it.pdf. [Accessed 2018 April 18].

[142] P. Smith and J. Blachut, "Buckling of externally pressurized prolate ellipsoidal domes," *Journal of Pressure Vessel Technology,* vol. 130, no. 1, p. 011210, 2008.

[143] G. Galletly, B. J. and J. Kruzelecki, "Plastic buckling of imperfect hemispherical shells subjected to external pressure," *Proceedings of the Institution of Mechanical Engineers, Part C: Journal of Mechanical Engineering Science,* vol. 201, no. 3, pp. 153-170, 1987.

[144] A. Lee, P. T. Brun, J. Marthelot, G. Balestra, F. Gallaire and P. M. Reis, "Fabrication of slender elastic shells by the coating of curved surfaces," *Nature communications,* vol. 7, 2016.

[145] N. H. Kussat, C. D. Chadwell and R. Zimmerman, "Absolute positioning of an autonomous underwater vehicle using GPS and acoustic measurements," *IEEE Journal of Oceanic Engineering,* vol. 30, no. 1, pp. 153-164, 2005.

[146] L. Freitag, M. Johnson, M. Grund, S. Singh and J. Preisig, "Integrated acoustic communication and navigation for multiple UUVs," in *MTS/IEEE Oceans 2001. An Ocean Odyssey. Conference Proceedings (IEEE Cat. No. 01CH37295)*, 2001.

[147] A. Alcocer, P. Oliveira and A. Pascoal, "Underwater acoustic positioning systems based on buoys with GPS," in *Proceedings of the Eighth European Conference on Underwater Acoustics*, Carvoerio, Portugal, 2006.

[148] A. Meschini, J. Gelli, M. Pagliai, A. della Valle, M. Franchi, M. Bianchi, A. Ridolfi and B. Allotta, "Design of a Self-moving Autonomous Buoy for the Localization of Underwater Targets," in *IEEE OCEANS2019*, Marseilles, France, 17-20 June 2019.

[149] B. Allotta, M. Bianchi, F. Fanelli, J. Gelli, N. Monni, M. Pagliai, N. Palma and A. Ridolfi, "An IMU and USBL-aided buoy for underwater localization," in *Proceedings of VII International Conference on Computational Methods in Marine Engineering (MARINE 2017)*, Nantes, France, 15-17 May 2017.

[150] R. Costanzi, N. Monni, A. Ridolfi, B. Allotta and A. Caiti, "On field experience on underwater acoustic localization through USBL modems," in *Proceedings of MTS/IEEE OCEANS2017* , Aberdeen, Scotland, 2017.

[151] H. O. Berteaux, Buoy engineering, New York: Wiley, 1976.

[152] Det Norske Veritas, *Buckling Strength of Shells. Recommended Practice DNV-RP-C202,* Høvik, Norway, 2013.

[153] "ROS: Robot Operating System," [Online]. Available: http://www.ros.org/.